Competing Orders in Honeycomb Hubbard Models with Nonlocal Coulomb Interactions

A Functional Renormalization Group Approach

Von der Fakultät für Mathematik, Informatik und Naturwissenschaften der RWTH Aachen University zur Erlangung des akademischen Grades eines Doktors der Naturwissenschaften genehmigte Dissertation

vorgelegt von

M.Sc. David Sánchez de la Peña

aus

Madrid

Berichter: Prof. Dr. Carsten Honerkamp
Priv.-Doz. Dr. Michael Scherer

Tag der mündlichen Prüfung: 31.08.2018

To my parents

Abstract

This dissertation focuses on the application of fermionic functional Renormalization Group (fRG) techniques to the study of competing electronic instabilities arising in two dimensional honeycomb lattice systems at low temperatures.

We start by developing a new computational scheme within the fRG, named Truncated Unity fRG (TUfRG), which allows to overcome some of the computational limitations of previous schemes like the Exchange Parametrization fRG, specifically in terms of parallel scalability. Making an efficient use of modern multi-core CPU clusters, the TUfRG scheme opens up the possibility for highly resolved calculations of wavevector dependences in the low-energy effective interactions, which are crucial for the correct description of undoped Honeycomb Hubbard models with extended Coulomb interactions.

We continue by applying the TUfRG to the undoped Honeycomb Hubbard model with extended Coulomb interactions up to the second nearest neighbor. As expected, the anti-ferromagnetic spin density wave instability appears for a dominant on-site repulsion between electrons, and charge density waves of different modulations for dominant pure n-th nearest neighbor repulsive interactions. New instabilities towards incommensurate charge density waves take place when non-local density interactions among several bond distances are simultaneously included. The possibility of a topological Mott insulator being the favored tendency for dominating second nearest neighbor interactions is not realized in our results with high momentum resolution. We also include the effect of a second-nearest neighbor hopping in the dispersion relation, and study its impact on the critical scales and critical coupling strength for antiferromagnetic ordering.

We finish by considering long-ranged Coulomb interactions on the Honeycomb Hubbard model. We find that the mutual competition among ordering tendencies triggered by extended interactions acting at different distances is essential for the stability of the semimetallic state. We then submit the system to biaxial strain, and analyze the critical amount of strain necessary to induce a quantum phase transition towards an ordered ground state. We investigate a range of parameters relevant to the realistic graphene material which are not accessible by numerically exact methods. Although a plethora of charge density waves arises under medium-range interactions, we find the antiferromagnetic spin-density wave to be the prevailing instability for long-ranged interactions. The critical strain needed to induce the antiferromagnetic transition turns out to depend mainly on the spatial decay of the bare interactions. We again explore the impact of including a second-nearest neighbor hopping term.

Zusammenfassung

Diese Dissertation befasst sich mit der Anwendung von Methoden der fermionischen funktionalen Renormierungsgruppen (fRG) auf konkurrierende elektronische Instabilitäten in zweidimensionalen Honigwabengittersystemen bei tiefen Temperaturen.

Wir beginnen mit der Entwicklung eines neuen Berechnungsschemas innerhalb der fRG, Truncated Unity fRG (TUfRG) genannt, dass uns erlaubt, rechnerische Einschränkungen von vorherigen Methoden wie der Austauschparametrisierungs fRG zu überwinden. Insbesondere handelt es sich dabei um Einschränkungen bezüglich der parallelen Skalierbarkeit. Durch eine effiziente Verwendung von modernen Mehrkernprozessoren, eröffnet das TUfRG Schema Möglichkeiten für hochauflösende Berechnungen von Wellenvektorabhängigkeiten der niedrigenergetischen effektiven Wechselwirkungen. Diese sind kritisch für eine richtige Beschreibung von undotierten Hubbardmodellen auf dem Honigwabegitter inklusive langreichweitiger Coulomb Wechselwirkungen.

Nachfolgend wenden wir die TUfRG auf das undotierte Hubbardmodell auf dem Honigwabegitter an. Dabei berücksichtigen wir langreichweitige Coulomb Wechselwirkungen bis zum zweit-nächsten Nachbarn. Wie erwartet, ergibt sich für dominierendes lokales Abstoßen zwischen Elektronen eine Instabilität hin zu antiferromagnetischen Spindichtewellen. Für dominierende repulsive reine n-te Nachbar Welchselwirungen finden wir Instabilitäten hin zu Ladungsdichtewellen unterschiedlicher Modulierungen. Wenn dagegen nicht-lokale Dichte-Dichte-Wechselwirkungen zwischen mehreren unterschiedlichen Gitterabständen berücksichtigt werden, treten neue Instabilitäten hin zu inkommensurabelen Ladungsdichtewellen auf. Laut unseren hochaufgelösten Ergebnissen für dominierende zweitenächste Nachbar Wechselwirkungen liegen keine Instabilitäten hin zu Topologischen Mott-Isolatoren vor. Desweiteren fügen wir einen zweiten Nachbar Hüpfenterm in die Dispersionsrelation ein und analysieren deren Einfluss auf kritische Skalen und kritische Kopplungsstärken für antiferromagnetische Ordnung.

Abschließend betrachten wir langreichweitige Columb Wechselwirkungen im Hubbardmodell auf dem Honigwabengitter. Wir argumentieren, dass die Konkurrenz zwischen verschiedenen Ordnungstendenzen, die vom nicht-lokalen Wechselwirkungen unterschiedlicher Abstände erzeugt werden, essenziell für die Stabilität des Semimetalls ist. Danach wenden wir auf das System biaxiale Dehnung an und analysieren bei welchen kritischen Spannungswerten ein Quantenphasenübergang hin zu einem geordneten Grundzustand auftritt. Wir untersuchen einen Parameterbereich, der für realistische Graphenmaterialien relevant ist und der für andere numerische Methoden nicht zugänglich ist. Auch wenn bei Wechselwirkungen, die von mittlerer Reichweite sind, eine Vielzahl an Landungsdichtewellen auftritt, ergeben unsere Analysen, dass die antiferromagnetische Spindichtewelle die vorherrschende Instabilität für langreichweitige Wechselwirkungen ist. Es zeigt sich, dass die kritische Dehnung, die zum Induzieren des antiferromagnetischen Übergangs nötig ist, hauptsächlich vom räumlichen Abfallverhalten der unrenormierten Wechselwirkung abhängt. Auch hier erforschen wir die Auswirkungen des Hüpfterms zwischen zweit-nächsten Nachbarn.

Contents

1. Introduction

Ever since the advent of quantum mechanics and atomic theory, culminating in the Standard Model of elementary particle physics, the reductionist philosophy of viewing systems as a mere sum of their parts has been very successful in revealing the fundamental principles that underlie the existence of matter and its properties. However, as famously conveyed by Anderson in his essay "More is different" [3], qualitative changes may follow from quantitative ones, in the sense that even if the individual agents in a system follow simple rules, large collections of such agents often display complex behavior which is not fully reducible to that of its constituents. Emergence, as opposed to reductionism, is one of the central aspects in the study of complexity theory, where systems are more than the sum of their parts. Emergent phenomena are ubiquitous across scientific disciplines, which may themselves be seen as a hierarchical structure where each discipline emerges from a more fundamental one as the degree of complexity in their respective field of study increases.

Emergence is particularly prevalent in the low-energy physics of quantum many-body systems. Although the behavior of isolated atoms and electrons is relatively well understood, the study of their aggregates in the form of liquids and solids is still a very active front of research. More specifically, interactions among electrons in a solid are paramount for a rich diversity of strongly correlated phases of matter [28,30] at low temperatures, including conventional and unconventional superconductivity [4,59], various forms of magnetism [11,83,92], charge ordering, and matter with exotic topological properties [19, 111]. This is especially true of two-dimensional crystalline systems, on which a lot of effort has been devoted in recent years.

Understanding strongly correlated electron systems from a fundamental perspective is an arduous task. Due to the inherently emergent nature of the spontaneous onset of order in a system which has undergone a symmetry breaking phase transition, it is necessary to reformulate the description of the system in terms of the emergent collective degrees of freedom instead of the fundamental ones. Guided by experience and intuition, one may resort to building effective models a posteriori, which directly involve the corresponding collective degrees of freedom of relevance. The values for parameters involved in model Hamiltonians must then be obtained via *ab initio* methods like Density Functional Theory (DFT). Another approach consists on making educated guesses about the types of order that a system may adopt, and then studying them via Mean-Field Theory (MFT) to discern which one is the most stable. Nevertheless, one would still want to comprehend the underlying mechanisms responsible for the existence of the various ordered phases. In some simple cases, identifying the kind of microscopic interactions required to trigger a particular macroscopically ordered state is not especially difficult. However, in most realistic scenarios there are several different interactions at play or different ordering tendencies being driven by a given interaction, and taking the competition and interplay among these tendencies into account is crucial for a correct understanding of their outcome. A prominent example is the manifestation of unconventional superconductivity in the square Hubbard model [45, 162], where a microscopic repulsive interaction between electrons due to their electric charge induces an effective interaction in the spin sector, and spin fluctuations subsequently mediate a d-wave pairing instability. Various many-body

methods have been devised which allow to study the low-energy physics of a strongly correlated system starting from knowledge about its properties at high-energy. They still rely on building model Hamiltonians for the microscopic physics, which require the input from *ab initio* methods, but provide the missing connection between the complex orderings arising in the symmetry broken states and the original features of the symmetric phase. The conceptual framework provided by the functional Renormalization Group (fRG) [97] has become a very valuable tool in the exploration of correlated electron systems at low energies, being specifically suited to bridge the simplicity of the microphysics with the complexity of the macrophysics in a many-body system. The core idea of the RG is to integrate out modes which have a high-energy relative to a variable energy scale of reference, and redefine the coupling parameters of the theory to absorb the effect of having decimated some degrees of freedom. The coupling parameters then become scale dependent quantities to reflect the successive averaging over high-energy modes. This leads to an RG flow equation for the couplings respect to the auxiliary scale, which allows to interpolate between the well understood microscopic behavior at high energy scales and the complex emergent phenomena at low energies. So far, the majority of fermionic fRG analyses employed to study correlated electron systems start by considering itinerant and weakly coupled electrons, and face technical challenges when attempting to directly describe transitions to insulating strongly correlated phases. Methodological improvements are still necessary in order to unlock the full potential of the fRG in this regard. However, it still provides a very flexible approach to do instability analyses, identifying ordering tendencies in an unbiased and transparent way. Quantitative predictions about ordered states, like gap sizes for example, are still difficult to obtain within fRG methods, but nevertheless, their qualitative predictive power has brought important insights for a broad variety of physical systems. For the explicit description of strongly correlated phases, other methods like Quantum Monte-Carlo (QMC), Exact Diagonalization (ED), or Dynamical Mean-Field Theory (DMFT) [96, 148], still provide better alternatives. They are not devoid of limitations either, with QMC being only applicable to sign-problem-free models, ED being only feasible for small sized systems, and DMFT being inaccurate in low dimensions. In general, no definite answer can be obtained by a single method, and the fRG complements the results of the aforementioned methods by allowing to go beyond their range of applicability. In comparison with simpler approaches like MFT or perturbative single-channel resummations, the fRG requires no ansatz of the kind of order that should prevail at low energy, and it treats all correlations on equal footing. Instead of singling out a candidate to be the dominating low-energy scattering process, the fRG includes all possible combinations of the relevant diagrams to infinite order. This is essential for the description of realistic situations where, as already mentioned, the interplay among several ordering tendencies plays a crucial role.

The interplay of competing ordering tendencies is of particular relevance for Dirac electron systems, which have caught the attention of the condensed matter community in the last decades. Ever since the experimental realization of graphene [15, 34, 103], a growing number of exotic materials have been studied whose low energy excitations behave like massless Dirac fermions. The linear dispersion relation of low-energy quasiparticles in such materials is of great academic interest, providing a condensed matter analogue of quantum electrodynamics in the ultrarelativistic limit, with the advantage that some effects which are difficult to observe in elementary particles become more accessible experimentally. It is also very relevant for technological applications, since it leads to an extremely high charge mobility in materials like monolayer graphene. Even more promising technological perspectives depend on the possibility of inducing phase transitions of the Dirac semimetal into gapped ordered states, which still poses an experimental challenge.

The Hubbard model on the Honeycomb lattice at charge neutrality is a standard prototype for Dirac electron systems, since its band structure features Dirac-cone structures at the corners of the Brillouin Zone. There are several important implications arising from the fact that the Fermi level lays at the linear band crossing and that subsequently there is a vanishing density of states. One of these implications is that electron interactions do not play a qualitatively relevant role [81] unless exceeding a critical interaction strength, the semimetallic state staying otherwise unperturbed. Moreover, the nature of effective interactions at low-energies is not fully dictated by the scattering of quasi-particles at the Fermi level, as it would be if there were a finite density of states. Another implication is that the Coulomb interaction between electrons is not efficiently screened and stays long ranged. Thus, on the one hand, it is required to consider correlations between energy modes across the whole band structure, and on the other hand, these are coupled by a myriad of interaction terms acting at different distances and competing with each other.

In a numerical fRG treatment of the emerging ordering tendencies at low temperature, such peculiarities of Dirac semi-metals require a fine discretization of momentum dependences in the effective interactions [123, 124, 129], posing a challenge for its successful application to the undoped Hubbard model on the Honeycomb lattice. Other approaches like Quantum Monte-Carlo (QMC) allow for a correct description of the semimetallic state and its transition to an antiferromagnetically ordered phase for both short- and long-ranged interactions [136, 144]. Unfortunately, these studies are limited in the choice of band model parameters and interaction profiles due to sign problems. Exact Diagonalization approaches have also provided important insights [14, 20], but are limited to small system sizes and generally neglect spin degrees of freedom for computational feasibility. Predictions of *ab inito* interaction parameters for graphene have found that electron interactions lie close to the critical values necessary to induce a phase transition to a gapped ordered state [156]. However, these critical values for given interaction terms only apply when such interactions are considered individually, in the absence of competition effects among the different terms. Experimental observations have consistently found a robust semimetallic state for pristine graphene, where interactions do not seem to play a role even at very low temperatures. Therefore the question arises, wether interactions may actually be weaker than often predicted, or are the overlooked competition effects responsible for the semimetallic stability.

In this thesis, we devise a new fRG implementation scheme which allows to perform efficient numerical computations with the required momentum resolution to accurately describe long-ranged interactions and correlations among modes of any wavevector in the Brillouin zone. Despite it not being an exact method, the flexibility of the fRG makes possible to go beyond the regimes explored by other methods in the search for possible deviations of the expected trends. We will analyze the impact of the different competing ordering tendencies on the semimetal in an unbiased way, and explore the possibility of achieving a realistic transition to an ordered state in graphene. For that matter, the application of biaxial strain provides an experimentally feasible way to enhance interaction effects in graphene, a possibility which has already been studied with Quantum Monte-Carlo [138]. We will contrast and complement the study by considering a range of parameters which were inaccessible in QMC. See the coming outline for a more detailed account of the contents of this thesis.

Outline of the thesis

This thesis is structured as follows.

After this introductory chapter, we dedicate Chapter 2 to briefly reviewing the functional Renormalization Group on its one-particle-irreducible formulation applied to fermionic systems. In particular, we sketch the derivation leading to the flow equations for U(1)- and SU(2)-invariant two-particle interactions in multiorbital systems, and explain their use to perform instability analyses in two-dimensional systems.

Chapter 3 focuses on the numerical implementation scheme for the flow equations. Starting from two recent approaches which allow for an efficient parametrization of two-particle interactions, namely, the exchange boson parametrization and the Singular Mode fRG, we relate the two in a new implementation scheme called the Truncated Unity fRG (TUfRG). The two previous approaches are first explained, and their respective advantages and drawbacks discussed. This will provide the motivational background to pursue their combination into a more advantageous scheme in the form of the TUfRG. Next, some useful symmetry relations are presented, and the different considerations for the initialization procedure of the TUfRG flow in multiband systems are enunciated.

The TUfRG is put to use on Chapter 4, where an instability analysis is done for the extended Hubbard model in the honeycomb lattice at half-filling. Considering up to the second-nearest neighbor in the bare interactions, a phase diagram from results with high momentum resolution is obtained. These new results allow us to update the fRG's predictions on the controversial possibility of a topological Mott insulating phase being realized in the honeycomb lattice for dominating second-nearest neighbor repulsive interactions. Novel instabilities arising due to competition in the charge sector are presented as well. We also include a second-nearest neighbor hopping term in the free dispersion and study its impact on antiferromagnetic ordering tendencies.

Chapter 5 continues the analysis done in the fourth chapter by extending the range of interactions up to several thousand neighbors. The intermediate regime is studied first, including the additional terms one by one up to the twentieth neighbor and exposing the semimetallic state as a consequence of a complex balance among competing ordering tendencies. Next, the stability of the semimetal is perturbed by the application of isotropic strain. Two sets of *ab initio* interaction parameters are used, together with their extrapolation to a long-ranged interaction and their respective modification under strain. Critical strain values for ordering are computed using different interaction profiles of various ranges, making a qualitative comparison to results from QMC. Finally, we analyze the impact of a second-nearest neighbor hopping on the strained and long-range interacting system.

Conclusions are drawn in Chapter 6, together with a brief outlook on future studies.

2. Method: Fermionic functional Renormalization Group

This chapter is meant to briefly introduce the exact functional RG-flow equation on which this thesis is based. See Refs. [80, 97] for a general review.

Contents

The theoretical framework provided by the Renormalization Group is one of the greatest conceptual achievements of twentieth century physics. At its root lie the ideas of scale transformations and scale invariance, which trace back to classical antiquity. The notion of renormalization first arose from the necessity to cancel out infinities which appear in perturbative quantum field theoretic calculations of fundamental interactions. By redefining the parameters of the fundamental theory as scale dependent quantities, finite predictions could be obtained at all perturbative orders. The first formulation of what is now known as the Renormalization Group came from the study of continuous phase transitions in statistical physics by Wilson [159,160], building on an idea of decimating degrees of freedom by Kadanoff [67]. By means of an iterative averaging over microscopic degrees of freedom and a subsequent redefinition of the system parameters, this Wilsonian renormalization technique was able to shed light on the puzzling universal behavior exhibited by seemingly unrelated systems when approaching a critical point. The key aspect was the identification of many microscopic properties of these systems as irrelevant for the macroscopic behavior.

Nowadays, the RG has become the standard theoretical tool to reconcile the different phenomena acting at distant energy and length scales in a physical system. In particular, it has allowed to understand how the dynamics of a many-body system at a fundamental microscopic scale may lead to the emergence of complex collective behavior at macroscopic scales. It is an invaluable tool in the study of condensed matter systems, which usually support a rich variety of strongly correlated phases in low dimensions and at low energies. The traditional Wilsonian approach, which ignores irrelevant degrees of freedom, provides a quantitatively accurate description of physical systems at criticality, with their scale invariance being identified from fixed points of the RG procedure. However, for more general cases away from criticality, the method

is only qualitatively correct. Many of the correlated low energy electronic states of interest to the condensed matter community are generally non-critical, and their existence depends on non-universal properties like the lattice structure, gap openings around Fermi-surfaces, and phenomena involved at intermediate energy scales. For the correct description of these phases of matter, an exact Renormalization Group technique is required which accounts for all the microscopic features of the system, including irrelevant ones.

The exact RG approach employed in this thesis has its roots in the work of Wegner [155], who introduced the use of exact flow equations for generating functionals in statistical field theory. Further developments by Polchinski [109] and Wetterich [158] have culminated in a unifying perspective of the diverse RG approaches devised across many different fields of physics, in what is now known as the functional Renormalization Group. Its applications range from high energy physics and cosmology to the physics of ultracold atoms and Bose-Einstein condensates [22]. It is also a widespread method in the many active research fronts of condensed matter theory, including unconventional superconductivity [45, 53, 78, 79, 86, 107, 114, 118, 139, 150, 152, 153, 162], topological states of matter [112, 129], quantum transport in low-dimensional systems [2, 94], systems out of equilibrium [64], and spin systems [115, 116].

2.1. Exact functional flow equations

In a functional integral formalism of quantum field theory [101], we consider an interacting many-fermion system described by the action

$$\mathcal{S}\left[\psi,\overline{\psi}\right] = -\left(\overline{\psi}, Q_0\psi\right) + V\left[\psi,\overline{\psi}\right] \tag{2.1}$$

with Grassmann fields $\psi, \overline{\psi}$, the inverse free propagator $Q_0 = G_0^{-1}$, and a generic many-body interaction $V\left[\psi,\overline{\psi}\right]$. The round brackets denote a scalar product between Grassmann fields

$$\left(\overline{\phi},\psi\right) \coloneqq \sum\!\!\!\!\!\!\int_{\xi} \overline{\phi}(\xi)\psi(\xi),$$

where the field index ξ collects all the quantum numbers in the basis set, and $\sum\!\!\!\!\!\!\int_{\xi}$ contains all the corresponding sums and integrals, together with normalization constants.

Thermodynamic quantities like the grand-canonical partition function can be written as functional integrals over the Grassmann fields

$$Z = \int \mathcal{D}\left(\overline{\psi},\psi\right) e^{-\mathcal{S}\left(\overline{\psi},\psi\right)},$$

where the functional integral measure reads

$$\mathcal{D}\left(\overline{\psi},\psi\right) \coloneqq \prod_{\xi} d\overline{\psi}(\xi) d\psi(\xi),$$

and normalization is again implicit. One can define the generating functional

$$\mathcal{G}\left[\eta,\overline{\eta}\right] = -\ln \int \mathcal{D}\left(\overline{\psi},\psi\right) e^{-\mathcal{S}\left(\overline{\psi},\psi\right)+\left(\overline{\eta},\psi\right)+\left(\overline{\psi},\eta\right)} \tag{2.2}$$

which provides the connected m-particle Green's functions by functional differentia-

tion respect to the source fields

$$G^{c(2m)}\left(\xi_1,\ldots,\xi_m;\xi'_1,\ldots,\xi'_m\right) = -\left\langle\psi(\xi_1)\ldots\psi(\xi_m)\overline{\psi}(\xi'_1)\ldots\overline{\psi}(\xi'_m)\right\rangle_c$$
$$= (-1)^m \frac{\delta^{2m}\mathcal{G}\left[\eta,\overline{\eta}\right]}{\delta\overline{\eta}(\xi_1)\ldots\delta\overline{\eta}(\xi_m)\delta\eta(\xi'_m)\ldots\delta\eta(\xi'_1)}\bigg|_{\eta=\overline{\eta}=0},$$

where $\langle\ldots\rangle_c$ denotes the connected expectation value. Due to the presence of interaction terms inside the action in Eq. 2.1, there is no general analytic solution for the functional integral in Eq. 2.2. If the physical system under consideration has an ordered ground state, conventional perturbative treatments of Eq. 2.2 fail. The obstacle lies in the appearance of infrared singularities among perturbative corrections, as a consequence of spontaneous symmetry breaking and the emergence of collective degrees of freedom.

A more convenient strategy is to construct a one-parameter family of generating functionals $\mathcal{G}^\Lambda$ that allows to interpolate between some solvable generating functional and the one of interest by varying the auxiliary parameter Λ. For that matter, the free propagator can be modified by the inclusion of a Λ-dependent regulator C^Λ,$G_0 \to G_0^\Lambda = C^\Lambda G_0$, which monotonically satisfies

$$C^\Lambda = \begin{cases} 0 & \text{for } \Lambda \to \infty \\ 1 & \text{for } \Lambda \to 0 \end{cases}, \tag{2.3}$$

so that

$$G_0^\Lambda = \begin{cases} 0 & \text{for } \Lambda \to \infty \\ G_0 & \text{for } \Lambda \to 0 \end{cases}, \quad \mathcal{G}^\Lambda = \begin{cases} 0 & \text{for } \Lambda \to \infty \\ \mathcal{G} & \text{for } \Lambda \to 0 \end{cases}.$$

Differentiating respect to Λ while keeping the fields constant, one obtains an exact functional flow equation

$$\partial_\Lambda \mathcal{G}^\Lambda\left[\eta,\overline{\eta}\right] = \left(\delta_\eta \mathcal{G}^\Lambda\left[\eta,\overline{\eta}\right], \dot{Q}_0^\Lambda\, \delta_{\overline{\eta}}\mathcal{G}\left[\eta,\overline{\eta}\right]\right) + \mathrm{tr}\left\{\dot{Q}_0^\Lambda\, \delta_{\overline{\eta}}\delta_\eta \mathcal{G}\left[\eta,\overline{\eta}\right]\right\} \tag{2.4}$$

with dot notation for Λ-derivatives, and with the trace above being defined as

$$\mathrm{tr}\left\{AB\right\} \coloneqq \sum\!\!\!\!\!\!\int_{\xi,\xi'} A(\xi,\xi')B(\xi',\xi). \tag{2.5}$$

Doing a Taylor expansion in both sides of Eq. 2.4 in powers of the source fields and comparing same order coefficients leads to an infinite hierarchy of coupled differential equations for the connected Green's functions. In practice, the trivial boundary condition $\mathcal{G}^{\Lambda\to\infty} = 0$ is not convenient since it does not contain any information about the system. It is more desirable to have a starting point which already contains some system specific information.

A better alternative is to use the generating functional for the one-particle irreducible (1PI) vertices Γ, which is the Legendre transform of $\mathcal{G}$

$$\Gamma\left[\psi,\overline{\psi}\right] = \mathcal{G}\left[\eta,\overline{\eta}\right] + \left(\overline{\eta},\psi\right) + \left(\overline{\psi},\eta\right) \tag{2.6}$$

with

$$\psi = -\frac{\delta\mathcal{G}}{\delta\overline{\eta}}, \quad \overline{\psi} = \frac{\delta\mathcal{G}}{\delta\eta}.$$

As implied, the 1PI vertex functions follow by functional differentiation

$$\Gamma^{(2m)}\left(\xi_1,\ldots,\xi_m;\xi_1',\ldots,\xi_m'\right)=\left.\frac{\delta^{2m}\Gamma\left[\psi,\overline{\psi}\right]}{\delta\overline{\psi}(\xi_1)\ldots\delta\overline{\psi}(\xi_m)\delta\psi(\xi_m')\ldots\delta\psi(\xi_1')}\right|_{\psi=\overline{\psi}=0}.$$

Due to the Legendre correspondence between $\mathcal{G}$ and Γ, their second functional derivatives respect to source fields are reciprocal

$$\boldsymbol{\delta}^2\Gamma\left[\psi,\overline{\psi}\right]=\left(\boldsymbol{\delta}^2\mathcal{G}\left[\eta,\overline{\eta}\right]\right)^{-1} \tag{2.7}$$

where

$$\boldsymbol{\delta}^2\Gamma^{\Lambda}\left[\psi,\overline{\psi}\right]=\begin{pmatrix}\frac{\delta^2\Gamma^{\Lambda}}{\delta\overline{\psi}(\xi)\delta\psi(\xi')} & \frac{\delta^2\Gamma^{\Lambda}}{\delta\overline{\psi}(\xi)\delta\overline{\psi}(\xi')}\\ \frac{\delta^2\Gamma^{\Lambda}}{\delta\psi(\xi)\delta\psi(\xi')} & \frac{\delta^2\Gamma^{\Lambda}}{\delta\psi(\xi)\delta\overline{\psi}(\xi')}\end{pmatrix}$$

$$\boldsymbol{\delta}^2\mathcal{G}^{\Lambda}\left[\eta,\overline{\eta}\right]=\begin{pmatrix}-\frac{\delta^2\mathcal{G}^{\Lambda}}{\delta\overline{\eta}(\xi')\delta\eta(\xi)} & \frac{\delta^2\mathcal{G}^{\Lambda}}{\delta\overline{\eta}(\xi')\delta\overline{\eta}(\xi)}\\ \frac{\delta^2\mathcal{G}^{\Lambda}}{\delta\eta(\xi')\delta\eta(\xi)} & -\frac{\delta^2\mathcal{G}^{\Lambda}}{\delta\eta(\xi')\delta\overline{\eta}(\xi)}\end{pmatrix}.$$

The inclusion of a regulator in the free propagator brings Eq. 2.6 to

$$\Gamma^{\Lambda}\left[\psi,\overline{\psi}\right]=\mathcal{G}^{\Lambda}\left[\eta,\overline{\eta}\right]+\left(\overline{\eta}^{\Lambda},\psi\right)+\left(\overline{\psi},\eta^{\Lambda}\right)$$

and by differentiating respect to Λ while keeping the fields constant we obtain the flow equation [98, 158]

$$\partial_{\Lambda}\Gamma^{\Lambda}\left[\psi,\overline{\psi}\right]=-\left(\overline{\psi},\dot{Q}_0^{\Lambda}\,\psi\right)-\frac{1}{2}\mathrm{Tr}\left\{\dot{\mathbf{Q}}_0^{\Lambda}\left(\boldsymbol{\delta}^2\Gamma^{\Lambda}\left[\psi,\overline{\psi}\right]\right)^{-1}\right\}, \tag{2.8}$$

where the capital trace now includes a summation over the matrix entries together with Eq. 2.5, and $\dot{\mathbf{Q}}_0^{\Lambda}$ is defined as

$$\dot{\mathbf{Q}}_0^{\Lambda}=\begin{pmatrix}\dot{Q}_0^{\Lambda} & 0\\ 0 & -\left(\dot{Q}_0^{\Lambda}\right)^T\end{pmatrix}.$$

The functional flow equation Eq. 2.8 satisfies the initial condition $\Gamma^{\Lambda\to\infty}=\mathcal{S}$, with the bare action $\mathcal{S}$ from Eq. 2.1, and the full effective action would be obtained by flowing down to $\Lambda=0$. Expanding Γ^{Λ} in a power series of the fields

$$\Gamma^{\Lambda}\left[\psi,\overline{\psi}\right]=\sum_{m=0}^{\infty}\mathcal{A}^{(2m)\Lambda}\left[\psi,\overline{\psi}\right]$$

with

$$\mathcal{A}^{(2m)\Lambda}\left[\psi,\overline{\psi}\right]=\frac{(-1)^m}{(m!)^2}\sum\!\!\!\!\!\!\int_{\substack{\xi_1\ldots\xi_m\\ \xi_1'\ldots\xi_m'}}\Gamma^{(2m)\Lambda}\left(\xi_1,\ldots,\xi_m;\xi_1',\ldots,\xi_m'\right)\times\overline{\psi}(\xi_1')\ldots\overline{\psi}(\xi_m')\psi(\xi_m)\ldots\psi(\xi_1), \tag{2.9}$$

and comparing same order terms, reveals the following infinite hierarchy of coupled

differential equations

$$\begin{aligned}
\frac{d}{d\Lambda}\mathcal{A}^{(0)\Lambda} &= -\operatorname{tr}\left\{\dot{Q}_0^\Lambda G^\Lambda\right\} \\
\frac{d}{d\Lambda}\mathcal{A}^{(2)\Lambda} &= -\frac{1}{2}\mathrm{Tr}\left\{\mathbf{S}^\Lambda \boldsymbol{\delta}^2\mathcal{A}^{(4)\Lambda}\right\} - \left(\overline{\psi}, \dot{Q}_0^\Lambda \psi\right) \\
\frac{d}{d\Lambda}\mathcal{A}^{(4)\Lambda} &= -\frac{1}{2}\mathrm{Tr}\left\{\mathbf{S}^\Lambda \boldsymbol{\delta}^2\mathcal{A}^{(6)\Lambda}\right\} + \frac{1}{2}\mathrm{Tr}\left\{\mathbf{S}^\Lambda \boldsymbol{\delta}^2\mathcal{A}^{(4)\Lambda}\mathbf{G}^\Lambda\boldsymbol{\delta}^2\mathcal{A}^{(4)\Lambda}\right\} \\
\frac{d}{d\Lambda}\mathcal{A}^{(6)\Lambda} &= -\frac{1}{2}\mathrm{Tr}\left\{\mathbf{S}^\Lambda \boldsymbol{\delta}^2\mathcal{A}^{(8)\Lambda}\right\} + \frac{1}{2}\mathrm{Tr}\left\{\mathbf{S}^\Lambda \boldsymbol{\delta}^2\mathcal{A}^{(4)\Lambda}\mathbf{G}^\Lambda\boldsymbol{\delta}^2\mathcal{A}^{(6)\Lambda}\right\} \\
&\quad + \frac{1}{2}\mathrm{Tr}\left\{\mathbf{S}^\Lambda \boldsymbol{\delta}^2\mathcal{A}^{(4)\Lambda}\mathbf{G}^\Lambda\boldsymbol{\delta}^2\mathcal{A}^{(4)\Lambda}\mathbf{G}^\Lambda\boldsymbol{\delta}^2\mathcal{A}^{(4)\Lambda}\right\} \\
&\quad \vdots
\end{aligned} \tag{2.10}$$

where

$$\mathbf{S}^\Lambda = \begin{pmatrix} S^\Lambda & 0 \\ 0 & -\left(S^\Lambda\right)^T \end{pmatrix} = -\mathbf{G}^\Lambda \dot{\mathbf{Q}}_0^\Lambda \mathbf{G}^\Lambda$$

is the so-called single-scale propagator, and $\mathbf{G}^\Lambda = \operatorname{diag}\left(G^\Lambda, -\left(G^\Lambda\right)^T\right)$. The zeroth order equation in Eqs. 2.10 amounts to the flow of the grand-canonical potential, and rewriting the rest in terms of the field-independent coefficients leads to an infinite hierarchy of flow equations for the 1PI vertices. The first three equations are depicted diagrammatically in Fig. 2.1, and the explicit form of the first two reads

$$\frac{d}{d\Lambda}\Sigma^\Lambda(\xi_1', \xi_1) = \sum\!\!\!\!\!\!\int_{\rho,\rho'} S^\Lambda(\rho,\rho')\Gamma^{(4)\Lambda}(\xi_1', \rho'; \xi_1, \rho) \tag{2.11}$$

$$\begin{aligned}
\frac{d}{d\Lambda}\Gamma^{(4)\Lambda}(\xi_1', \xi_2'; \xi_1, \xi_2) &= -\sum\!\!\!\!\!\!\int_{\rho,\rho'} S^\Lambda(\rho,\rho')\Gamma^{(6)\Lambda}(\xi_1', \xi_2', \rho'; \xi_1, \xi_2, \rho) \\
&\quad + \sum\!\!\!\!\!\!\int_{\substack{\xi,\xi' \\ \rho,\rho'}} G^\Lambda(\xi,\xi')S^\Lambda(\rho,\rho') \times \Big(\Gamma^{(4)\Lambda}(\xi_1', \xi_2'; \xi, \rho)\Gamma^{(4)\Lambda}(\xi', \rho'; \xi_1, \xi_2) \\
&\quad - \Big[\Gamma^{(4)\Lambda}(\xi_1', \rho'; \xi_1, \xi)\Gamma^{(4)\Lambda}(\xi', \xi_2'; \rho, \xi_2) + (\xi \leftrightarrow \rho, \xi' \leftrightarrow \rho')\Big] \\
&\quad + \Big[\Gamma^{(4)\Lambda}(\xi_2', \rho'; \xi_1, \xi)\Gamma^{(4)\Lambda}(\xi', \xi_1'; \rho, \xi_2) + (\xi \leftrightarrow \rho, \xi' \leftrightarrow \rho')\Big]\Big),
\end{aligned} \tag{2.12}$$

where in Eq. 2.11 we made use of $\Gamma^{(2)\Lambda} = \left(G^\Lambda\right)^{-1} = Q_0^\Lambda - \Sigma^\Lambda$, following from the reciprocity relation (2.7) for the first order Taylor coefficients, together with the Dyson equation.

2.2. Truncation

The flow equation of every vertex in Eqs. 2.10 contains a self-contraction of a vertex of next order, and therefore the coupled hierarchy never closes. Thus, it is generally not possible to solve the exact functional flow equation, since it amounts to solving an infinite set of coupled differential equations. In order to make calculations feasible, the hierarchy has to be truncated. For the physical problems of interest in the coming chapters, the most common and adequate truncation consists on neglecting all vertices $\Gamma^{(2m)}$ of order $m > 2$, the so-called level-2 truncation. Dropping the six-point vertex $\Gamma^{(6)}$ can be justified in light of the argumentation found in Ref. [121]. For physical systems involving two-particle bare interactions only, and these not being strong, $\Gamma^{(6)}$ is zero at the start of the flow and it remains small at high energy scales.

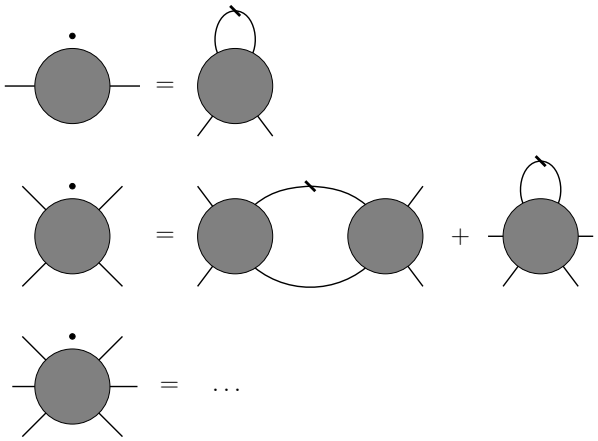

Figure 2.1.: Diagrammatic representation of the first two flow equations in the hierarchy of Eqs. 2.10, where dotted vertices on the left-hand-side represent scale differentials. The diagrammatic structure at each order is obtained from a self-contraction of a vertex of next order, plus all possible one-loop terms obtainable with vertices of the given order and below. One of the internal lines in every loop is a single-scale propagator, denoted in the figure by a barred line.

Even though $\Gamma^{(4)}$ may start to take large values at intermediate or low scales, it can be shown through phase-space constraints that $\Gamma^{(6)}$ still stays comparatively small. Nevertheless, although higher order vertices are not expected to have a qualitative influence on the flow, their quantitative impact may still be relevant. Two-loop [26, 74] and multiloop [82] approaches have been devised, allowing to go beyond the level-2 truncation.

Together with the level-2 truncation, a common further simplification is to neglect the flow of self-energies. This is done due to technical difficulties and computational limitations, some of which are summarized in chapter 12 of Ref. [6]. The hierarchy of flow equations is thus reduced to a single equation involving the two-particle vertex only. In two-dimensional systems at zero temperature (which will be the focus of this study), as long as the density of states at the Fermi level is non-zero, the flow equation contains singular diagrams. In the absence of self-energy corrections, which would regularize such singularities by altering the single-particle energy spectrum (e.g. via a gap opening), one typically encounters *flows to strong coupling* where some components of $\Gamma^{(4)}$ diverge. The RG flow has to be stopped when coupling strengths exceed the order of magnitude of the single-particle bandwidth, since the aforementioned approximations break down below that scale. Not only would self-energy effects become important, but with a divergent two-particle vertex the neglect of higher order vertices is no longer justified.

2.3. SU(2) symmetric flow equations

So far we have implicitly restricted ourselves to U(1)-invariant theories for charge conservation, manifest in the fact that only even orders of the m-point functions are non-zero. In addition, our focus will lie on SU(2)-invariant systems where interactions respect spin-rotational symmetry. Writing dependences on quantum numbers more explicitly than in previous sections, the antisymmetric two-particle vertex $\Gamma^{(4)}$ for

Matsubara frequencies and momenta $k_i = (\omega_i, \mathbf{k}_i)$, and spins s_i, can be expressed in terms of a spin independent coupling function V [121] via

$$\Gamma^{(4)\Lambda}_{s_1,s_2,s_3,s_4}(k_1,k_2,k_3,k_4) = V^\Lambda(k_1,k_2,k_3,k_4)\delta_{s_1,s_3}\delta_{s_2,s_4} - V^\Lambda(k_2,k_1,k_3,k_4)\delta_{s_1,s_4}\delta_{s_2,s_3}\,, \tag{2.13}$$

with incoming particles 1 and 2, and outgoing particles 3 and 4. Furthermore, since the lattice systems studied in this work satisfy discrete translational symmetries, interactions respect frequency-wavevector conservation (modulo reciprocal lattice vectors). This allows to reduce the description to a coupling function with three dependences, $V^\Lambda(k_1,k_2,k_3)$, and a self-energy with a single dependence. Dependences on other quantum numbers which do not follow conservation laws, like band indices, must all be kept explicitly. For notational clarity, we will ignore band indices for now.

The flow equations in the level-2 truncation under these additional symmetries read

$$\frac{d}{d\Lambda}\Sigma^\Lambda(k) = \int dp \left[2V^\Lambda(k,p,k) - V(k,p,p)\right] S^\Lambda(p) \tag{2.14}$$

$$\frac{d}{d\Lambda}V^\Lambda(k_1,k_2,k_3) = \mathcal{T}^\Lambda_{\mathrm{pp}}(k_1,k_2,k_3) + \mathcal{T}^\Lambda_{\mathrm{ph,cr}}(k_1,k_2,k_3) + \mathcal{T}^\Lambda_{\mathrm{ph,d}}(k_1,k_2,k_3) \tag{2.15}$$

with contributions from the particle-particle channel $\mathcal{T}_{\mathrm{pp}}$, crossed particle-hole channel $\mathcal{T}_{\mathrm{ph,cr}}$ and direct particle-hole channel $\mathcal{T}_{\mathrm{ph,d}}$

$$\begin{aligned}
\mathcal{T}^\Lambda_{\mathrm{pp}}(k_1,k_2,k_3) &= -\int dp\, V^\Lambda(k_1,k_2,p)\, V^\Lambda(p,k_1+k_2-p,k_3) L^\Lambda(p,k_1+k_2-p)\,,\\
\mathcal{T}^\Lambda_{\mathrm{ph,cr}}(k_1,k_2,k_3) &= -\int dp\, V^\Lambda(k_1,p+k_2-k_3,p)\, V^\Lambda(p,k_2,k_3) L^\Lambda(p,p+k_2-k_3)\,,
\end{aligned} \tag{2.16}$$

$$\begin{aligned}
\mathcal{T}^\Lambda_{\mathrm{ph,d}}(k_1,k_2,k_3) = -\int dp\ \big[&-2V^\Lambda(k_1,p+k_3-k_1,k_3)\, V^\Lambda(p,k_2,p+k_3-k_1)\\
&+ V^\Lambda(k_1,p+k_3-k_1,p)\, V^\Lambda(p,k_2,p+k_3-k_1)\\
&+V^\Lambda(k_1,p+k_3-k_1,k_3)\ V^\Lambda(k_2,p,p+k_3-k_1)\big] L^\Lambda(p,p+k_3-k_1)\,.
\end{aligned}$$

where $L^\Lambda(k,k') = S^\Lambda(k)G^\Lambda(k') + G^\Lambda(k)S^\Lambda(k')$ and $\int dp$ is shorthand notation for $\int \frac{d\mathbf{p}}{A_{BZ}} \frac{1}{\beta}\sum_\omega$ with Brillouin zone area A_{BZ} and inverse temperature β. The diagrammatic representation of the three contributions in Eq. (2.16) is presented in Fig. 2.2.

In the flows without self-energy corrections, since

$$S^\Lambda = -G^\Lambda \dot{Q}^\Lambda_0 G^\Lambda = \frac{d}{d\Lambda}\, G^\Lambda\big|_{\Sigma^\Lambda \text{fixed}} \tag{2.17}$$

one has a more compact expression for the loops, namely $L^\Lambda(k,k') = \frac{d}{d\Lambda}G^\Lambda(k)G^\Lambda(k')$. In the general case including self-energies, the latter replacement [72] in L brings additional contributions of third order in the interaction to the flow of the two-particle vertex, which would otherwise contribute via the self-contraction of the neglected three-particle vertex.

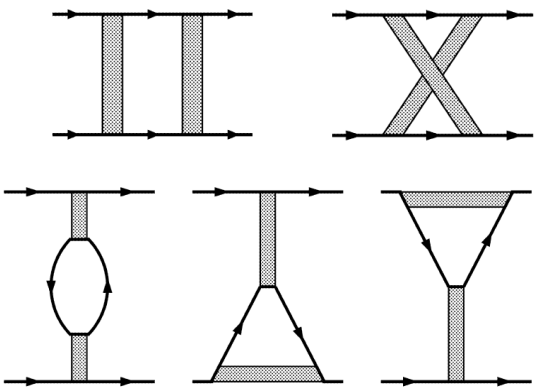

Figure 2.2.: Diagrammatic representation of the three channels in Eq. (2.16), with particle-particle (top left), crossed particle-hole (top right) and direct particle-hole (bottom) diagrams. One of the internal lines in the loops is a single scale propagator.

2.4. Flow parameters and regulator choices

Some of the versatility and broad applicability of functional RG methods lies in its flexibility respect to the choice of regulator, which may describe any possible path in the coupling parameter space as long as it satisfies Eq. 2.3. Since in practice the exact flow equation is generally not exactly solvable, the use of different regulators can also provide a means of error estimation. As mentioned in Sec. 2.2, for the physical systems considered in this work and neglecting self-energies, singularities will lure in the infrared. In general these are logarithmic singularities for $T \to 0$ of the form $g \log (W/T)$ after Matsubara summation for a frequency independent interaction, with coupling constant g and bandwidth W. The most widespread choice of regulator is a low energy cutoff, normally taken in momentum space relative to the free dispersion $\epsilon (\mathbf{k})$ and in the form of a step function $\Theta (|\epsilon (\mathbf{k})| - \Lambda)$. It is from this momentum-shell cutoff scheme that the single-scale propagator gets its name, since it only gets support at energy Λ. In numerical implementations, it is generally convenient to choose the regulator to be a smooth step function of finite width. After the inclusion of this regulator, the singularity can be approached in a controlled and transparent way by reducing the RG scale Λ. Unfortunately, it has an important drawback, since particle-hole processes with $\omega = 0$ and $\mathbf{q} \to 0$ can only start to contribute when Λ drops to the scale of the temperature, which means that they are excluded in studies at zero temperature. Other alternatives which avoid this problem are to directly use the temperature as flow parameter in the so-called temperature-flow, or to start from the non-interacting case and increase the coupling constant g in the so-called interaction-flow.

Yet another option which also avoids the aforementioned problem is to use a smooth regulator in frequency space. A convenient form for such a regulator was introduced by Husemann and Salmhofer [61] in their so-called Ω-scheme, reading

$$C^{\Omega}(\omega) = \frac{\omega^2}{\omega^2 + \Omega^2} \tag{2.18}$$

where Ω here takes the role previously held by Λ. Its convenience lies in the fact that it still allows the Matsubara sums in the loops to be performed analytically for frequency independent interactions if the self-energy is neglected. Apart from

avoiding the artificial suppression of some particle-hole processes, the Ω-regulator also allows to include the real part of self-energies in the flow in a more reliable way than cutoffs that discriminate energy modes respect to the free dispersion, like the usual momentum shell cutoff. The Ω-regulator will be employed throughout the work done in this thesis. The resulting expressions for the one-loop integrals can be found in App. B.

2.5. Multiband models

The SU(2)-symmetric flow equations 2.16 for the coupling function written in Sec. 2.3 can be generalized to the description of multiorbital systems, for a review see Ref. [108]. Although the physical intepretation of single particle states in a basis of localized Wannier functions is normally the most natural, it is generally more economical to work on a band basis where free Green's functions are diagonal. The momentum dependent part of the coupling function in band basis is then obtained by

$$V^{b_1b_2b_3b_4}(\mathbf{k}_1,\mathbf{k}_2,\mathbf{k}_3) = \sum_{\substack{o_1o_2\\o_3o_4}} V^{o_1o_2o_3o_4}(\mathbf{k}_1,\mathbf{k}_2,\mathbf{k}_3)\, \hat{T}^{b_1,o_1}_{\mathbf{k}_1}\, \hat{T}^{b_2,o_2}_{\mathbf{k}_2} \left(\hat{T}^{b_3,o_3}_{\mathbf{k}_3}\right)^* \left(\hat{T}^{b_4,o_4}_{\mathbf{k}_4}\right)^* \tag{2.19}$$

where the explicit scale dependence was omitted for notational clarity, and $\hat{T}^{b_i,o_i}_{\mathbf{k}_i}$ are the unitary transformation elements between orbital and band degrees of freedom. This transformation is not unique, and in practice the specific choice may have relevant implications [90], as it will be the case in our studies on the honeycomb lattice system. Note that for lattices with a multiatomic basis, like the bipartite honeycomb lattice, we will also refer to sublattice dependences as orbital dependences. The additional momentum structure of the coupling function in band picture due to the transformation (2.19) is often referred to as *orbital makeup* [141, 142].

The flow equations in 2.16 generalize in the multiband case to

$$\begin{aligned}
\mathcal{T}^{b_1\ldots b_4}_{\mathrm{pp}}(k_1,k_2,k_3) &= -\int dp\, V^{b_1b_2bb'}(k_1,k_2,p)\, V^{bb'b_3b_4}(p,k_1+k_2-p,k_3) L^{bb'}(p,k_1+k_2-p)\,,\\
\mathcal{T}^{b_1\ldots b_4}_{\mathrm{ph,cr}}(k_1,k_2,k_3) &= -\int dp\, V^{b_1b'bb_4}(k_1,p+k_2-k_3,p)\, V^{bb_2b_3b'}(p,k_2,k_3) L^{bb'}(p,p+k_2-k_3)\,,
\end{aligned} \tag{2.20}$$

$$\begin{aligned}
\mathcal{T}^{b_1\ldots b_4}_{\mathrm{ph,d}}(k_1,k_2,k_3) = -\int dp\ \Big[&-2V^{b_1b'b_3b}(k_1,p+k_3-k_1,k_3)\, V^{bb_2b'b_4}(p,k_2,p+k_3-k_1)\\
&+ V^{b_1b'bb_3}(k_1,p+k_3-k_1,p)\, V^{bb_2b'b_4}(p,k_2,p+k_3-k_1)\\
&+V^{b_1b'b_3b}(k_1,p+k_3-k_1,k_3)\ V^{b_2bb'b_4}(k_2,p,p+k_3-k_1)\Big] L^{bb'}(p,p+k_3-k_1)\,.
\end{aligned}$$

where now $\int dp = \int \frac{d\mathbf{p}}{A_{BZ}} \frac{1}{\beta} \sum_\omega \sum_{bb'}$ and $L^{bb'}(k,k') = \frac{d}{d\Lambda} G^\Lambda(k,b) G^\Lambda(k',b')$.

2.6. Instability analyses

The application of the fRG method presented so far sets the stage for the instability analyses performed in the following chapters. Due to the simplifications done when reducing the exact flow equation to a level-2 truncation without self-energies, one is

not allowed to flow through phase transitions into symmetry broken phases. However, in our studies of interacting electrons on two-dimensional lattices, if the system has ordered low-energy phases, these become manifest as flows to strong coupling where the two-particle vertex diverges. These divergences reflect the fact that important modifications to the single-particle spectrum would have taken place if the self-energy had been included, and the need for additional order parameter fields describing the collective excitations associated with the symmetry breaking phase transition. Although he phase transition cannot be studied directly, the buildup of long-range order and possible interplay or competition between different tendencies can be reproduced in an unbiased way. The fRG treats all correlations on the same footing, without singling out any specific interaction channel as in ladder resummations. Instead of having to rely on an ansatz or educated guess about the predominant order in low-energy regimes, as is done in mean field studies, the instability towards an ordered phase emerges spontaneously in the flow. This unbiasedness is one of the main strengths of the fRG method, together with its wide applicability, since it is not restricted to particular band structures or interaction types.

In the usual instability analyses, when encountering a divergence in the coupling function, the flow is normally stopped when it exceeds the order of magnitude of the single-particle bandwidth, although the precise choice of a stopping point has no relevant effect on the stopping scale since the couplings diverge strongly as the instability is approached. That stopping scale provides an upper estimate for critical scales. Furthermore, the divergences arise forming sharp structures in frequency and momentum space, indicating the onset of long-range order, and the type of ordering instability can be read from such structures. For example, in the SU(2) invariant case, the possible sharp dependences which the coupling function may develop appear for specific combinations of external frequencies and momenta which correspond to the transfer l involved in the loops $L^{bb'}(k, \pm(l-k))$, which as of Eq. (2.16), can take the values $l = k_1 + k_2$, $l = k_3 - k_2$ or $l = k_1 - k_3$. Divergences in either of these frequency and momentum combinations respectively indicate a superconducting, magnetic, or charge ordering instability. Focusing on the momentum part, the precise value of $\mathbf{l}$ for which the diverge occurs provides the real space modulation of the ordered phase. The weaker dependences on the remaining momenta normally take the form of low level harmonic functions, and reflect the symmetry character of the order parameter to be induced at the phase transition. Further details about the system's information encoded in the behavior of the two-particle coupling function will be discussed in the next chapter.

3. Implementation: The Truncated Unity fRG scheme

In this chapter we derive a novel computational scheme for functional Renormalization Group calculations for interacting fermions on 2D lattices. We start by introducing its predecessors, namely, the exchange parametrization scheme and the Singular Mode fRG. Our scheme is obtained from the exchange parametrization by inserting truncated partitions of unity in the loop integrals. These insertions decouple the fermionic propagators from the exchange propagators and lead to a separation of the underlying equations. We show that this separation is numerically advantageous and may pave the way for refined, large-scale computational investigations even in the case of complex multiband systems, with the extended Hubbard model on the honeycomb lattice as a prototype. This chapter sets up the numerical implementation of the fRG which will be employed for the studies of graphene in the following chapters.

Parts of this chapter have already been published in Refs. [87, 123, 124]

Contents

Ever since its inception, the fermionic functional RG introduced in the previous chapter has gone through important developments in its application to 2-dimensional lattice systems at low temperature. Despite the simplifications undergone by the exact functional flow equation to arrive at an ordinary integro-differential equation for the two-particle interaction, the latter can only be solved numerically in the vast majority of cases. The refinement of numerical schemes, together with the progress and greater availability of computing power, is allowing for the investigation of an ever wider range of material classes and exotic phenomena using fRG methods.

The main focus of the scheme presented in this chapter, and employed throughout this thesis, is the accurate description of the functional dependence of two-particle

interactions on wavevectors in the Brillouin zone (BZ). So far, the most common procedure has been to discretize momentum dependences only along the Fermi surface, in the so-called *N-patch scheme* or *Fermi surface patching* [53, 71, 162]. This scheme constituted a significant improvement on previous g-ology models, which simplified low-energy interactions to a handful of couplings g_i representing the scattering among hot-spots in the Fermi surface. The applicability of g-ology models on 2-dimensional systems is therefore limited to situations where the low-energy activity is restricted to a few locations in the Fermi surface. By tracking the tangential momentum dependence along the whole Fermi surface, the N-patch scheme significantly broadened the application scope of the fRG method.

However, although patching schemes have been successful in providing sound insights for a variety of physical systems, other systems remain where the wavevector dependences away from the Fermi surface play a relevant role. The example of interest is that of Dirac electron systems, which have pointlike Fermi surfaces with a vanishing density of states. Although in principle a zero dimensional Fermi surface provides the ideal scenario for the applicability of g-ology models, one should include interactions between energy modes across the whole band structure and not just from the vicinity of the Fermi level, especially since at the latter the density of states vanishes. Another reason for the necessity of a finer Brillouin zone discretization is the inclusion of extended interactions, which have to be properly resolved in momentum space. In the same example of Dirac electrons, due to the vanishing density of states at the Fermi level, interactions are not efficiently screened and stay long-ranged. Finally, in a general case, more elaborate numerical schemes are needed for quantitatively precise predictions, since typically the obtainable fRG results are only qualitatively correct.

The most straightforward attempts to extend the N-patch scheme to these situations lead to the *multi-patch scheme*, consisting on also patching perpendicularly to the Fermi surface. However, discretizing a function which depends on three two-dimensional arguments is numerically expensive and does not scale well, and thus the total number of patches has to be kept relatively small for computational feasibility. A more convenient parametrization of the two-particle vertex function is necessary in order to overcome these limitations. The Truncated Unity functional Renormalization Group (TUfRG) scheme [87] presented in this chapter constitutes a further step to already existing improved parametrizations of the two-particle vertex flow equation [24–26, 37, 61, 62, 91, 151, 152, 161], based on channel decomposed flows. One of the central considerations in the development of the TUfRG is the fact that modern numerical implementations rely heavily on parallel and high performance computing. Together with the physical considerations, computing efficiency and scalability must also be taken into account, and it is in this regard that the TUfRG delivers some of its main advantages.

As already mentioned, the main focus here will be on momentum dependences of the two-particle interaction. Except for some minor comments, frequency dependences and self-energies will be ignored. The Fermi surface patching scheme has already been used to explore the inclusion of self-energy effects and frequency dependence [54, 73, 117, 143], but channel decomposed flows provide a more promising alternative [24,25,37,61,62,70], although so far only simplified decompositions of frequency dependences have been taken into account. The development of cutoff schemes like the Ω-regulator have allowed to include the real part of self-energies in the flow in a more reliable way than cutoffs that discriminate energy modes respect to the free dispersion, like the usual momentum shell cutoff. The Fermi surface patching scheme has also been implemented to describe models without spin-rotational invariance [91, 128, 131] due to the presence of spin-orbit coupling terms. A great effort has been made in the continuation of flows into symmetry broken phases [25, 27, 35, 36, 91, 137]. Higher

loop approaches [26,74,82] have also made possible to go beyond the standard level-2 truncation of the functional hierarchy. The Fermi surface patching scheme has often been applied to multiband systems [108] at the expense of momentum resolution or the possibility to include frequency dependences. In the presence of high-energy bands away from the Fermi level, it is unclear how to correctly patch them. So far, the majority of the more refined channel decomposed schemes including frequencies and self-energies have been focused on single-band systems or multiband models with important simplifications. Although the TUfRG scheme has not yet been applied to computations including self-energy effects and frequency dependence, its applicability to multiband models is shown in this thesis for the honeycomb lattice as a prototype. In its current state, the band dependences of the two-particle coupling are fully kept. For its extension to systems featuring a high number of bands, a more efficient reparametrization of band dependences would be additionally required. Recently, the TUfRG has also been extended to the study of multiband models without SU(2) invariance [132].

3.1. Boson exchange parametrization

An important breakthrough towards a more efficient scheme took place with the so-called *exchange parametrization* of Husemann and Salmhofer [61]. Its main insight builds upon the fact that the singular momentum dependences which a regular vertex function can develop in the RG-flow are dictated by the singular contributions produced by the one-loop bubbles. These singular contributions take place for particular values of the transfer momenta involved in the one-loop diagrams of the flow equation. For instance, in the SU(2) invariant flow equation there are three kinds of contributions, written in Eq. (2.16) as particle-particle, crossed particle-hole and direct particle-hole, each having a momentum transfer of $\mathbf{k_1}+\mathbf{k_2}$, $\mathbf{k_3}-\mathbf{k_2}$ and $\mathbf{k_1}-\mathbf{k_3}$, respectively. When encountering a flow to strong coupling, the coupling function develops a strong dependence on one of these wavevector combinations, from which the physical nature of the instability can be read, as explained in Sec. 2.6. This allows for a reparametrization of the coupling function in terms of different channels, each picking up a direct dependence on one of the transfer momenta, which read

$$\begin{aligned} V^{b_1\ldots b_4}(\mathbf{k}_1,\mathbf{k}_2,\mathbf{k}_3) = & V^{\Omega_0,\,b_1\ldots b_4}_{\mathbf{k}_1,\mathbf{k}_2,\mathbf{k}_3} - \Phi^{\mathrm{SC},\,b_1\ldots b_4}_{\mathbf{k}_1+\mathbf{k}_2,\frac{\mathbf{k}_1-\mathbf{k}_2}{2},\frac{\mathbf{k}_3-\mathbf{k}_4}{2}} + \Phi^{\mathrm{M},\,b_1\ldots b_4}_{\mathbf{k}_3-\mathbf{k}_2,\frac{\mathbf{k}_1+\mathbf{k}_4}{2},\frac{\mathbf{k}_2+\mathbf{k}_3}{2}} \\ & - \frac{1}{2}\Phi^{\mathrm{K},b_1\ldots b_4}_{\mathbf{k}_1-\mathbf{k}_3,\frac{\mathbf{k}_1+\mathbf{k}_3}{2},\frac{\mathbf{k}_2+\mathbf{k}_4}{2}} + \frac{1}{2}\Phi^{\mathrm{M},b_1\ldots b_4}_{\mathbf{k}_1-\mathbf{k}_3,\frac{\mathbf{k}_1+\mathbf{k}_3}{2},\frac{\mathbf{k}_2+\mathbf{k}_4}{2}} , \end{aligned} \tag{3.1}$$

where V^{Ω_0} is the initial bare interaction which stays constant, and the so called *single-channel coupling functions* Φ are generated during the flow according to

$$\begin{aligned} \partial_\Omega \Phi^{\mathrm{SC},\,b_1\ldots b_4}_{\mathbf{k}_1+\mathbf{k}_2,\frac{\mathbf{k}_1-\mathbf{k}_2}{2},\frac{\mathbf{k}_3-\mathbf{k}_4}{2}} &= -\mathcal{T}^{b_1\ldots b_4}_{\mathrm{pp}}(\mathbf{k}_1,\mathbf{k}_2,\mathbf{k}_3) , \\ \partial_\Omega \Phi^{\mathrm{M},\,b_1\ldots b_4}_{\mathbf{k}_3-\mathbf{k}_2,\frac{\mathbf{k}_1+\mathbf{k}_4}{2},\frac{\mathbf{k}_2+\mathbf{k}_3}{2}} &= \mathcal{T}^{\mathrm{cr},\,b_1\ldots b_4}_{\mathrm{ph}}(\mathbf{k}_1,\mathbf{k}_2,\mathbf{k}_3) , \\ \partial_\Omega \Phi^{\mathrm{K},\,b_1\ldots b_4}_{\mathbf{k}_1-\mathbf{k}_3,\frac{\mathbf{k}_1+\mathbf{k}_3}{2},\frac{\mathbf{k}_2+\mathbf{k}_4}{2}} &= -2\mathcal{T}^{\mathrm{d},\,b_1\ldots b_4}_{\mathrm{ph}}(\mathbf{k}_1,\mathbf{k}_2,\mathbf{k}_3) + \mathcal{T}^{\mathrm{cr},\,b_1\ldots b_4}_{\mathrm{ph}}(\mathbf{k}_1,\mathbf{k}_2,\mathbf{k}_1+\mathbf{k}_2-\mathbf{k}_3) . \end{aligned} \tag{3.2}$$

The dependence of V and Φ functions on the regularization scale Ω is assumed. The first momentum argument in the single-channel coupling functions denotes the transfer momenta, and the second and third arguments capture the remaining weak momentum dependences. This channel decomposition is not unique, its original formulation here being cast in terms of the three possible rearrangements of a general

U(1) and SU(2) two-particle interaction in the form of fermion bilinears. This way, after the assignments in Eq. (3.2) the SC, M and K channels can be physically interpreted as pairing, magnetic and charge scattering corrections to the bare interaction, respectively. The single-channel coupling functions stand subsequently as coefficients or coupling functions for interactions among Cooper pairs, spin operators and density operators. The convention used here for the weak momentum dependences is motivated by symmetry arguments and differs from the original one in Ref. [61]. As explicitly shown in App. A, the weak momentum dependences are the Fourier duals of the real space distances between the two operators within each bilinear, and the transfer momenta are conjugate to the relative distance between midpoints of the corresponding bilinears.

For the sake of generality and unbiasedness, the initial bare interaction V^{Ω_0} is kept as a separate scale independent term in the channel decomposition. This avoids possible ambiguities when having to assign a given interaction to either of the three channels, the simplest example being the case of a momentum independent coupling, which can be equivalently formulated in all channels. The initial condition for the single-channel coupling functions at the start of the flow is therefore zero valued. However, as discussed in Sec. 3.3.4, in some practical cases it is more convenient to assign the bare interaction as initial condition in the single-channel functions.

A different decomposition is used in the Singular Mode fRG scheme (SMfRG) of Ref. [151], directly following the diagrammatic structure of particle-hole channels. It reads

$$\begin{aligned} V^{b_1\ldots b_4}(\mathbf{k}_1,\mathbf{k}_2,\mathbf{k}_3) =& V^{\Omega_0,\,b_1\ldots b_4}_{\mathbf{k}_1,\mathbf{k}_2,\mathbf{k}_3} - \Phi^{\mathrm{P},\,b_1\ldots b_4}_{\mathbf{k}_1+\mathbf{k}_2,\frac{\mathbf{k}_1-\mathbf{k}_2}{2},\frac{\mathbf{k}_3-\mathbf{k}_4}{2}} + \Phi^{\mathrm{C},\,b_1\ldots b_4}_{\mathbf{k}_3-\mathbf{k}_2,\frac{\mathbf{k}_1+\mathbf{k}_4}{2},\frac{\mathbf{k}_2+\mathbf{k}_3}{2}} \\ &+ \Phi^{\mathrm{D},b_1\ldots b_4}_{\mathbf{k}_1-\mathbf{k}_3,\frac{\mathbf{k}_1+\mathbf{k}_3}{2},\frac{\mathbf{k}_2+\mathbf{k}_4}{2}} , \end{aligned} \tag{3.3}$$

with

$$\begin{aligned} \partial_\Omega \Phi^{\mathrm{P},\,b_1\ldots b_4}_{\mathbf{k}_1+\mathbf{k}_2,\frac{\mathbf{k}_1-\mathbf{k}_2}{2},\frac{\mathbf{k}_3-\mathbf{k}_4}{2}} &= -\mathcal{T}^{b_1\ldots b_4}_{\mathrm{pp}}(\mathbf{k}_1,\mathbf{k}_2,\mathbf{k}_3) , \\ \partial_\Omega \Phi^{\mathrm{C},\,b_1\ldots b_4}_{\mathbf{k}_3-\mathbf{k}_2,\frac{\mathbf{k}_1+\mathbf{k}_4}{2},\frac{\mathbf{k}_2+\mathbf{k}_3}{2}} &= \mathcal{T}^{\mathrm{cr},\,b_1\ldots b_4}_{\mathrm{ph}}(\mathbf{k}_1,\mathbf{k}_2,\mathbf{k}_3) , \\ \partial_\Omega \Phi^{\mathrm{D},\,b_1\ldots b_4}_{\mathbf{k}_1-\mathbf{k}_3,\frac{\mathbf{k}_1+\mathbf{k}_3}{2},\frac{\mathbf{k}_2+\mathbf{k}_4}{2}} &= \mathcal{T}^{\mathrm{d},\,b_1\ldots b_4}_{\mathrm{ph}}(\mathbf{k}_1,\mathbf{k}_2,\mathbf{k}_3) , \end{aligned} \tag{3.4}$$

amounting to a mere relabeling for the pairing and magnetic channels, whereas the charge channel is obtained by

$$\Phi^{\mathrm{K},b_1\ldots b_4}_{\mathbf{k}_1-\mathbf{k}_3,\frac{\mathbf{k}_1+\mathbf{k}_3}{2},\frac{\mathbf{k}_2+\mathbf{k}_4}{2}} = -2\Phi^{\mathrm{D},b_1\ldots b_4}_{\mathbf{k}_1-\mathbf{k}_3,\frac{\mathbf{k}_1+\mathbf{k}_3}{2},\frac{\mathbf{k}_2+\mathbf{k}_4}{2}} + \Phi^{\mathrm{C},b_1\ldots b_4}_{\mathbf{k}_1-\mathbf{k}_3,\frac{\mathbf{k}_1+\mathbf{k}_3}{2},\frac{\mathbf{k}_2+\mathbf{k}_4}{2}} . \tag{3.5}$$

Although the SMfRG does not strictly follow a channel decomposition as in the exchange parametrization, Eq. (3.3) will be the decomposition used in the TUfRG, which can be said to be a combination of the two former approaches. More specific details about the SMfRG will be discussed in the following section.

With the channel decompositions written so far, the possible singular momentum dependences developed in the flow have been separated. The next step undertaken in the exchange parametrization is to expand the weak momentum dependences of the

single-channel coupling functions onto a suitable orthonormal basis of form factors

$$\begin{aligned}
\Phi^{\mathrm{P},\, b_1 \ldots b_4}_{\mathbf{l},\mathbf{k},\mathbf{k}'} &= \sum_{m,n} f_m(\mathbf{k})\, f_n^*(\mathbf{k}')\, P^{b_1 \ldots b_4}_{m,n}(\mathbf{l})\,, \\
\Phi^{\mathrm{C},\, b_1 \ldots b_4}_{\mathbf{l},\mathbf{k},\mathbf{k}'} &= \sum_{m,n} f_m(\mathbf{k})\, f_n^*(\mathbf{k}')\, C^{b_1 \ldots b_4}_{m,n}(\mathbf{l})\,, \\
\Phi^{\mathrm{D},\, b_1 \ldots b_4}_{\mathbf{l},\mathbf{k},\mathbf{k}'} &= \sum_{m,n} f_m(\mathbf{k})\, f_n^*(\mathbf{k}')\, D^{b_1 \ldots b_4}_{m,n}(\mathbf{l})\,.
\end{aligned} \tag{3.6}$$

This way, the interaction between fermion bilinears is in fact rewritten as if mediated by an auxiliary exchange boson carrying the transfer momentum $\mathbf{l}$, and hence the objects P, C, D are consequently named bosonic propagators. Note that the naming is only due to analogy, and that no explicit bosonic fields are being considered. This reparametrization is formally exact so far, but in practice the infinite basis of form factors has to be truncated. A right choice of form factor basis minimizes the truncation error and allows to capture weak momentum dependences with just a handful of terms. The choice of form factor basis will be discussed in Sec. 3.3.1. After this expansion, the coupling function can then be conveniently described by three objects, each having just one momentum dependence. Upon discretization of the strong momentum dependences, the numerical effort should scale linearly respect to the number of sampling points, in contrast with the cubic scaling of Fermi-surface patching schemes. For that matter, one must first rewrite the RG-flow equation (2.16) in terms of the bosonic propagators via

$$\begin{aligned}
\partial_\Omega P^{b_1 \ldots b_4}_{m,n}(\mathbf{l}) &= -\hat{P}\left[\mathcal{T}^{b_1 \ldots b_4}_{\mathrm{pp}}\right]_{m,n}(\mathbf{l}) \\
\partial_\Omega C^{b_1 \ldots b_4}_{m,n}(\mathbf{l}) &= \hat{C}\left[\mathcal{T}^{\mathrm{cr},\, b_1 \ldots b_4}_{\mathrm{ph}}\right]_{m,n}(\mathbf{l}) \\
\partial_\Omega D^{b_1 \ldots b_4}_{m,n}(\mathbf{l}) &= \hat{D}\left[\mathcal{T}^{\mathrm{d},\, b_1 \ldots b_4}_{\mathrm{ph}}\right]_{m,n}(\mathbf{l})
\end{aligned} \tag{3.7}$$

where the projection operators $\hat{P}, \hat{C}, \hat{D}$ act as an inverse to the expansions (3.6) and read

$$\begin{aligned}
\hat{P}\,[F]_{m,n}(\mathbf{l}) &= \int d\mathbf{k}\, d\mathbf{k}'\, f_m^*(\mathbf{k})\, f_n(\mathbf{k}')\, F\left(\frac{\mathbf{l}}{2}+\mathbf{k}, \frac{\mathbf{l}}{2}-\mathbf{k}, \frac{\mathbf{l}}{2}+\mathbf{k}'\right), \\
\hat{C}\,[F]_{m,n}(\mathbf{l}) &= \int d\mathbf{k}\, d\mathbf{k}'\, f_m^*(\mathbf{k})\, f_n(\mathbf{k}')\, F\left(\mathbf{k}+\frac{\mathbf{l}}{2}, \mathbf{k}'-\frac{\mathbf{l}}{2}, \mathbf{k}'+\frac{\mathbf{l}}{2}\right), \\
\hat{D}\,[F]_{m,n}(\mathbf{l}) &= \int d\mathbf{k}\, d\mathbf{k}'\, f_m^*(\mathbf{k})\, f_n(\mathbf{k}')\, F\left(\mathbf{k}+\frac{\mathbf{l}}{2}, \mathbf{k}'-\frac{\mathbf{l}}{2}, \mathbf{k}-\frac{\mathbf{l}}{2}\right).
\end{aligned} \tag{3.8}$$

All momentum integration measures implicitly include a normalization over the Brillouin Zone area. A direct numerical computation of the high-dimensional integrals above would be costly. Moreover, for reasons of memory bounds, if momentum dependences in the bosonic propagators are finely discretized, it might be undesirable having to reconstruct the coupling function V appearing in the right-hand-side of Eq. (3.7) in its full momentum dependences. Instead, one can decompose every instance of the coupling function in the flow equations so that they only explicitly involve the bosonic propagators. However, this generates intricate diagrams which are challenging to compute, namely, mixed boson-fermion loops. There are three types of diagrams involved in the flow equation for a given bosonic propagator $B \in \{P, C, D\}$, as shown in Fig. 3.1. The easiest to compute are those which arise from the B parts themselves in both V's of the right-hand-side, shown in Fig. 3.1a, since the loops stay in the purely fermionic $L(k, k')$ type defined in Sec. 2.3. Diagrams involving a contribution

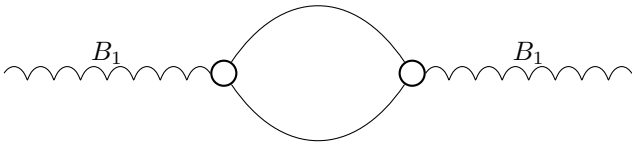

(a) Propagator renormalization diagram

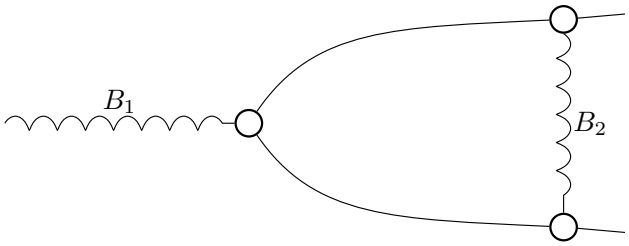

(b) Vertex correction diagram

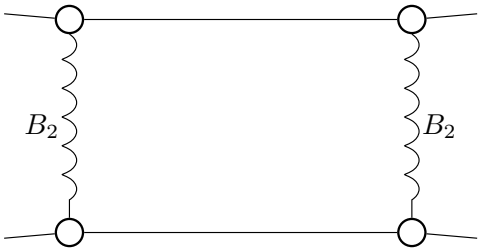

(c) Box diagram

Figure 3.1.: The three different types of loop diagrams arising in the boson exchange parametrization for the flow of a bosonic propagator B_1. A bosonic propagator from any of the other two channels is denoted by B_2. Solid lines represent fermionic propagators.

from channels other than B in either one or both of the V's lead to vertex correction and box diagrams, respectively shown in Figs. 3.1b - 3.1c. The loops in these diagrams contain bosonic propagators together with the fermionic Green's functions. As already mentioned, the fermionic $L(k, k')$ loops drive the singular structure of the flow, and are already challenging to compute on their own. Adding the bosonic propagators, which eventually develop sharp structures during the flow, further increases the difficulty of the loop integrals. Moreover, the presence of the bosonic propagators in the integrands hinders the parallel scalability of a computer code implementation of these integrals due to interprocess communication.

For the neglected frequency dependences, a similar decomposition was already developed by Karrasch in Ref. [70]. In that work, the frequency dependent vertex was split intro functions depending on a single transfer frequency each, i.e. remaining weak dependences on other frequency combinations are discarded altogether instead of being expanded in some form factor basis. Similarly, in the original implementation of Ref. [61] the transfer frequency dependences are also kept in the bosonic propagators, but the form factors are only momentum dependent. The remaining dependences, which are fermionic frequencies in their convention, are projected to be

a half of the bosonic transfer momenta in their version of Eq. (3.8). A proposal for basis functions which could result in a more compact representation than Matsubara frequency harmonics is the Legendre polynomial representation of Ref. [10]. The limitations on the straight separation of frequency dependences done in Refs. [61,70] have been exposed in Ref. [147].

3.2. The Singular Mode fRG scheme

The Singular Mode fRG introduced by Wang [151] takes a different approach to that of the boson exchange parametrization of last section. It is also based on separately keeping track of the singular momentum dependences in the two-particle coupling function, but instead of decomposing in single-channel couplings, the two-particle interaction is itself expanded in three different but complementary approximations, namely

$$\begin{aligned}
V^{b_1\ldots b_4}(\mathbf{k}_1,\mathbf{k}_2,\mathbf{k}_3) &= \sum_{m,n} f_m\left(\frac{\mathbf{k}_1-\mathbf{k}_2}{2}\right) f_n^*\left(\frac{\mathbf{k}_3-\mathbf{k}_4}{2}\right) V_{m,n}^{\mathrm{P},\,b_1\ldots b_4}(\mathbf{k}_1+\mathbf{k}_2)\,,\\
V^{b_1\ldots b_4}(\mathbf{k}_1,\mathbf{k}_2,\mathbf{k}_3) &= \sum_{m,n} f_m\left(\frac{\mathbf{k}_1+\mathbf{k}_4}{2}\right) f_n^*\left(\frac{\mathbf{k}_2+\mathbf{k}_3}{2}\right) V_{m,n}^{\mathrm{C},\,b_1\ldots b_4}(\mathbf{k}_3-\mathbf{k}_2)\,, \qquad (3.9)\\
V^{b_1\ldots b_4}(\mathbf{k}_1,\mathbf{k}_2,\mathbf{k}_3) &= \sum_{m,n} f_m\left(\frac{\mathbf{k}_1+\mathbf{k}_3}{2}\right) f_n^*\left(\frac{\mathbf{k}_2+\mathbf{k}_4}{2}\right) V_{m,n}^{\mathrm{D},\,b_1\ldots b_4}(\mathbf{k}_1-\mathbf{k}_3)\,.
\end{aligned}$$

The choice of momentum combinations for strong and weak dependences matches that of the previous channel decomposition, in order to relate the two approaches more easily. Note that the convention for weak momentum dependences expanded in form factors is different in the original formulation of Ref. [151]. Alternatively, the expressions above can also be cast using the projections defined in Eq. (3.8), yielding

$$\begin{aligned}
V_{m,n}^{\mathrm{P},\,b_1\ldots b_4}(\mathbf{k}_1+\mathbf{k}_2) &= \hat{P}\,[V]_{m,n}^{b_1\ldots b_4}(\mathbf{k}_1+\mathbf{k}_2)\,,\\
V_{m,n}^{\mathrm{C},\,b_1\ldots b_4}(\mathbf{k}_3-\mathbf{k}_2) &= \hat{C}\,[V]_{m,n}^{b_1\ldots b_4}(\mathbf{k}_3-\mathbf{k}_2)\,,\\
V_{m,n}^{\mathrm{D},\,b_1\ldots b_4}(\mathbf{k}_1-\mathbf{k}_3) &= \hat{D}\,[V]_{m,n}^{b_1\ldots b_4}(\mathbf{k}_1-\mathbf{k}_3)\,.
\end{aligned}$$

The flow of these three approximations of the coupling function, which we will denote *projected V*s in the following, reads

$$\begin{aligned}
\partial_\Omega V_{m,n}^{\mathrm{P},\,b_1\ldots b_4}(\mathbf{l}) &= \hat{P}\left[\mathcal{T}_{\mathrm{pp}}+\mathcal{T}_{\mathrm{ph}}^{\mathrm{cr}}+\mathcal{T}_{\mathrm{ph}}^{\mathrm{d}}\right]_{m,n}^{b_1\ldots b_4}(\mathbf{l})\,,\\
\partial_\Omega V_{m,n}^{\mathrm{C},\,b_1\ldots b_4}(\mathbf{l}) &= \hat{C}\left[\mathcal{T}_{\mathrm{pp}}+\mathcal{T}_{\mathrm{ph}}^{\mathrm{cr}}+\mathcal{T}_{\mathrm{ph}}^{\mathrm{d}}\right]_{m,n}^{b_1\ldots b_4}(\mathbf{l})\,,\\
\partial_\Omega V_{m,n}^{\mathrm{D},\,b_1\ldots b_4}(\mathbf{l}) &= \hat{D}\left[\mathcal{T}_{\mathrm{pp}}+\mathcal{T}_{\mathrm{ph}}^{\mathrm{cr}}+\mathcal{T}_{\mathrm{ph}}^{\mathrm{d}}\right]_{m,n}^{b_1\ldots b_4}(\mathbf{l})\,,
\end{aligned}$$

which in terms of the bosonic propagators and single-channel coupling functions of previous section becomes

$$\begin{aligned}
\partial_\Omega \mathbf{V}^{\mathrm{P}}(\mathbf{l}) &= -\partial_\Omega \mathbf{P}(\mathbf{l}) + \hat{P}\left[\partial_\Omega \Phi^{\mathrm{C}}\right](\mathbf{l}) + \hat{P}\left[\partial_\Omega \Phi^{\mathrm{D}}\right](\mathbf{l})\,,\\
\partial_\Omega \mathbf{V}^{\mathrm{C}}(\mathbf{l}) &= -\hat{C}\left[\partial_\Omega \Phi^{\mathrm{P}}\right](\mathbf{l}) + \partial_\Omega \mathbf{C}(\mathbf{l}) + \hat{C}\left[\partial_\Omega \Phi^{\mathrm{D}}\right](\mathbf{l})\,, \qquad (3.10)\\
\partial_\Omega \mathbf{V}^{\mathrm{D}}(\mathbf{l}) &= -\hat{D}\left[\partial_\Omega \Phi^{\mathrm{P}}\right](\mathbf{l}) + \hat{D}\left[\partial_\Omega \Phi^{\mathrm{C}}\right](\mathbf{l}) + \partial_\Omega \mathbf{D}(\mathbf{l})\,,
\end{aligned}$$

where boldface objects are shorthand tensor notation for the various band and form factor index dependences.

In this approach, one does not encounter mixed boson-fermion loop integrals. In the RG-flow of V^{B}, $B \in \{P, C, D\}$, computing the intra-channel contribution $\partial_\Omega B$ involves purely fermionic one-loop integrals. Once these have been determined, they are inserted in form factor expansions of $\partial_\Omega \Phi^{\mathrm{B}}$'s at the inter-channel feedback contributions, which then amount to integrating a scale-differentiated bosonic propagator together with four form factors. The resulting expressions are completely analogous to those used in the TUfRG, and thus we refer the reader to the next section where they will be derived from an exchange parametrization perspective.

Despite the aforementioned advantage of the SMfRG in calculating loop integrals, it entails an important drawback compared to other schemes. An ambiguity is introduced with the definition of different approximations of the coupling function, and the right pick for reconstructing the coupling function becomes a matter of context. It is unclear which of the three projected Vs we should unproject, for example, to be plugged into the self-energy flow equation if we had not neglected it. The result will strongly depend on the ambiguous choice, since the projected coupling functions only contain one of the three important momentum dependences while the other two are smoothened out by the projection process and cannot be fully recovered due to a truncated form factor basis.

3.3. The Truncated Unity fRG scheme

The following scheme was developed in the course of this thesis with the objective of combining the advantageous traits of the two schemes presented so far. It allows to keep bosonic lines out of the loop integrals as in the SMfRG, but without introducing the ambiguities discussed at the end of the previous section. In a sense, the key attempt of the TUfRG is to arrive at flow equations analogous to those of the SMfRG but starting from the formulation of the boson exchange parametrization. We continue where the exchange parametrization was left off in Sec. 3.1, namely at Eq. (3.7), which for the P channel reads

$$\begin{aligned}
\partial_\Omega P^{b_1\dots b_4}_{m,n}(\mathbf{l}) &= -\hat{P}\left[\mathcal{T}^{b_1\dots b_4}_{\mathrm{pp}}\right]_{m,n}(\mathbf{l}) \qquad (3.11)\\
&= -\int d\mathbf{k}\, d\mathbf{k}'\, f^*_m(\mathbf{k})\, f_n(\mathbf{k}')\, \mathcal{T}^{b_1\dots b_4}_{\mathrm{pp}}\left(\frac{\mathbf{l}}{2}+\mathbf{k}, \frac{\mathbf{l}}{2}-\mathbf{k}, \frac{\mathbf{l}}{2}+\mathbf{k}'\right)\\
&= \int d\mathbf{k}\, d\mathbf{k}'\, f^*_m(\mathbf{k})\, f_n(\mathbf{k}') \int dk'' V^{b_1 b_2 b b'}\left(\frac{\mathbf{l}}{2}+\mathbf{k}, \frac{\mathbf{l}}{2}-\mathbf{k}, \mathbf{k}''\right)\\
&\qquad \times L^{bb'}(k'', l-k'')\, V^{bb' b_3 b_4}\left(\mathbf{k}'', \mathbf{l}-\mathbf{k}'', \frac{\mathbf{l}}{2}+\mathbf{k}'\right)
\end{aligned}$$

where again $k'' = (\omega, \mathbf{k}'')$ and $\int dk'' = \int d\mathbf{k}'' \frac{1}{\beta}\sum_\omega \sum_{bb'}$ with momentum integration measures $d\mathbf{k}$ implicitly including a normalization factor over the Brillouin Zone area. The fermionic bubble was defined as $L^{bb'}(k,k') = \frac{d}{d\Omega} G^\Omega(k,b) G^\Omega(k',b')$. Note that together with the neglect of Matsubara frequency dependences in the coupling function, the external frequencies $\omega_1 \dots \omega_4$ are set to zero because we are interested in groundstate properties. Since we will always work at zero temperature, there is no inconsistency in fermionic frequencies taking zero values. It then follows that bosonic transfer frequencies are always zero, i.e. $l = (0, \mathbf{l})$.

To avoid the difficulty of mixed fermion-boson loops arising when decomposing the coupling functions as in the exchange parametrization, one can directly expand them in form factors as done in the SMfRG. Together with a shift of the integration variable $\mathbf{k}'' \to \mathbf{k}'' + \mathbf{l}/2$ for a more symmetric expression, the form factor expansion yields

$$\begin{aligned}\partial_\Omega P^{b_1\dots b_4}_{m,n}(\mathbf{l}) = &\int d\mathbf{k}\, d\mathbf{k}'\, f^*_m(\mathbf{k})\, f_n(\mathbf{k}') \int dk''\, V^{b_1 b_2 b b'}\left(\frac{\mathbf{l}}{2}+\mathbf{k}, \frac{\mathbf{l}}{2}-\mathbf{k}, \frac{\mathbf{l}}{2}+\mathbf{k}''\right) \\ &\times L^{bb'}\left(\frac{l}{2}+k'', \frac{l}{2}-k''\right) V^{bb' b_3 b_4}\left(\frac{\mathbf{l}}{2}+\mathbf{k}'', \frac{\mathbf{l}}{2}-\mathbf{k}'', \frac{\mathbf{l}}{2}+\mathbf{k}'\right) \\ = &\int d\mathbf{k}\, d\mathbf{k}'\, f^*_m(\mathbf{k})\, f_n(\mathbf{k}') \int dk'' \sum_{m'',m'} f_{m''}(\mathbf{k})\, f^*_{m'}(\mathbf{k}'') V^{\mathrm{P},\, b_1 b_2 b b'}_{m'',m'}(\mathbf{l}) \\ &\times L^{bb'}\left(\frac{l}{2}+k'', \frac{l}{2}-k''\right) \sum_{n',n''} f_{n'}(\mathbf{k}'')\, f^*_{n''}(\mathbf{k}') V^{\mathrm{P},\, bb' b_3 b_4}_{n',n''}(\mathbf{l})\,.\end{aligned} \tag{3.12}$$

Since the form factor basis is orthonormal, the above expression can be simplified using $\int d\mathbf{k}\, f^*_m(\mathbf{k}) f_{m''}(\mathbf{k}) = \delta_{m,m''}$ and $\int d\mathbf{k}'\, f^*_{n''}(\mathbf{k}') f_n(\mathbf{k}') = \delta_{n'',n}$ to arrive at

$$\partial_\Omega P^{b_1\dots b_4}_{m,n}(\mathbf{l}) = \sum_{m',n'} V^{\mathrm{P},\, b_1 b_2 b b'}_{m,m'}(\mathbf{l}) V^{\mathrm{P},\, bb' b_3 b_4}_{n',n}(\mathbf{l}) \tag{3.13}$$

$$\times \int dk''\, f^*_{m'}(\mathbf{k}'') L^{bb'}\left(\frac{l}{2}+k'', \frac{l}{2}-k''\right) f_{n'}(\mathbf{k}'')\,. \tag{3.14}$$

After these modifications, the loops stay purely fermionic but now also contain form factors. With the right choice of form factor basis, the appearance of sharp bosonic propagators is replaced by slowly varying functions which make the loop integrals much more manageable. The complete form factor basis actually contains an infinite number of functions, but an appropriate truncation neglects strongly oscillating ones. The price to pay is that we now have several fermionic loops to compute, since the various form factor combinations must be considered. Nevertheless, they can all be calculated independently from each other, which is beneficial for a scalable parallel code implementation. Furthermore, one also needs to calculate the projected Vs via the inter-channel projections detailed in Sec. 3.3.2. The latter can also be computed in parallel in an efficient and scalable way. The result of pulling bosonic propagators out of the loops is illustrated in Fig. 3.2 for the example of a vertex correction diagram.

An equivalent way to arrive at Eq. (3.13) is to directly insert partitions of unity in the form factor basis

$$\mathbb{1} = \int d\mathbf{p}'\, \delta(\mathbf{p}-\mathbf{p}') = \int d\mathbf{p}' \sum_m f^*_m(\mathbf{p}') f_m(\mathbf{p}) \tag{3.15}$$

at both sides of the fermionic bubble L in Eq. (3.11) to isolate the corresponding projection of the coupling function into V^{P}. In practice, such partitions of unity must also be truncated for computational feasibility, hence the name of the scheme.

The procedure for the particle-hole channels follows analogously to the one here illustrated. The obvious difference is that they involve a particle-hole bubble $L^{bb'}(k'', k''-l)$ instead of the particle-particle one of Eq. (3.11). One can then define

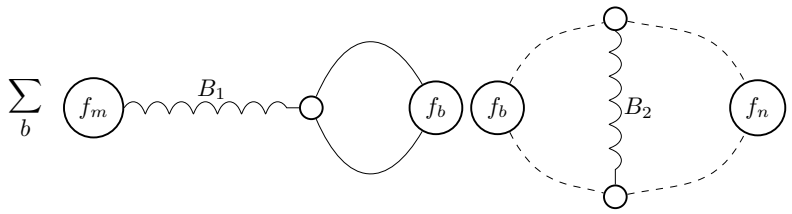

Figure 3.2.: Modification of the vertex correction diagram in Fig. 3.1b after the insertion of a partition of unity between the fermionic propagators (solid lines) and the bosonic one (wiggly line) in the loop. Dashed lines are just contractions including a form factor as in the projection operations, so that the dashed bubble corresponds to $\hat{B}_1\left[\Phi^{\mathrm{B}_2}\right]$.

the form factor projected bubbles

$$\chi^{\mathrm{pp},\,bb'}_{m,n}(l) = \int dp\, G\left(\frac{l}{2}+p,b\right) G\left(\frac{l}{2}-p,b'\right) f^*_m(\mathbf{p})\, f_n(\mathbf{p})\,, \tag{3.16}$$

$$\chi^{\mathrm{ph},\,bb'}_{m,n}(l) = \int dp\, G\left(p+\frac{l}{2},b\right) G\left(p-\frac{l}{2},b'\right) f^*_m(\mathbf{p})\, f_n(\mathbf{p})\,,$$

so that the flow equations can be written in terms of its scale derivatives

$$\partial_\Omega \chi^{\mathrm{pp},\,bb'}_{m,n}(l) = \int dp\, L^{bb'}\left(\frac{l}{2}+p,\frac{l}{2}-p\right) f^*_m(\mathbf{p})\, f_n(\mathbf{p})\,, \tag{3.17}$$

$$\partial_\Omega \chi^{\mathrm{ph},\,bb'}_{m,n}(l) = \int dp\, L^{bb'}\left(p+\frac{l}{2},p-\frac{l}{2}\right) f^*_m(\mathbf{p})\, f_n(\mathbf{p})\,.$$

This finally leads to the TUfRG flow equations

$$\dot{P}^{b_1\ldots b_4}_{m,n}(\mathbf{l}) = \sum_{m',n'}\sum_{b,b'} V^{\mathrm{P},\,b_1b_2bb'}_{m,m'}(\mathbf{l})\, \dot{\chi}^{\mathrm{pp},\,bb'}_{m',n'}(\mathbf{l})\, V^{\mathrm{P},\,bb'b_3b_4}_{n',n}(\mathbf{l})\,,$$

$$\dot{C}^{b_1\ldots b_4}_{m,n}(\mathbf{l}) = \sum_{m',n'}\sum_{b,b'} -V^{\mathrm{C},\,b_1b'bb_4}_{m,m'}(\mathbf{l})\, \dot{\chi}^{\mathrm{ph},\,bb'}_{m',n'}(\mathbf{l})\, V^{\mathrm{C},\,bb_2b_3b'}_{n',n}(\mathbf{l})\,,$$

$$\begin{aligned}\dot{D}^{b_1\ldots b_4}_{m,n}(\mathbf{l}) = \sum_{m',n'}\sum_{b,b'} \Big(&2V^{\mathrm{D},\,b_1b'b_3b}_{m,m'}(\mathbf{l})\, \dot{\chi}^{\mathrm{ph},\,bb'}_{m',n'}(\mathbf{l})\, V^{\mathrm{D},\,bb_2b'b_4}_{n',n}(\mathbf{l}) - \\ &- V^{\mathrm{C},\,b_1b'bb_3}_{m,m'}(\mathbf{l})\, \dot{\chi}^{\mathrm{ph},\,bb'}_{m',n'}(\mathbf{l})\, V^{\mathrm{D},\,bb_2b'b_4}_{n',n}(\mathbf{l}) - V^{\mathrm{D},\,b_1b'b_3b}_{m,m'}(\mathbf{l})\, \dot{\chi}^{\mathrm{ph},\,bb'}_{m',n'}(\mathbf{l})\, V^{\mathrm{C},\,b_2bb'b_4}_{n',n}(\mathbf{l})\Big)\,,\end{aligned} \tag{3.18}$$

with scale derivatives represented in dot notation.

Let us recapitulate before moving on to the calculation of projected Vs. As shown in this section, it is possible to combine the main advantages of the exchange parametrization and the SMfRG, namely, to have an efficient reparametrization of the two-particle coupling function without introducing ambiguities or having to deal with mixed fermion-boson loop integrals. Starting from the exchange parametrization scheme, an insertion of truncated partitions of unity allows to pull bosonic lines out of the loop integrals to arrive at flow equations of the SMfRG form. Thus, the TUfRG is basically the standard exchange parametrization scheme with an additional approximation. The main drawback that comes with it, is the need to additionally compute the projected Vs for inter-channel feedback. On the other front, the SMfRG and TUfRG are mostly equivalent from a formal and computational perspective. The

only difference is that the TUfRG keeps track of the bosonic propagators as core objects in the calculation, whereas in the SMfRG only their scale derivatives are computed as an auxiliary step to renormalize the projected Vs. The TUfRG therefore allows for an unequivocal reconstruction of the full coupling function without entailing any drawbacks respect to the SMfRG scheme.

For a demonstration of the scheme's performance and scalability in a distributed multi-core CPU implementation, and the feasibility of achieving good convergence with a low number of form factors, we refer to Ref. [87] where the TUfRG is applied to the $t - t'$ Hubbard model as test case. For details on our current numerical implementation, and considerations on parallelization and scalability, see App. D.

3.3.1. Form factor basis

An interlude to introduce our choice of form factors will ease discussing the calculation of inter-channel projections. The expansion in form factors will capture the weak momentum dependences, corresponding to the extension of fermionic bilinears in real space. These are dominated by short bond distances within bilinears, hence their weakly oscillating behavior in momentum space. Therefore, a meaningful way to truncate the form factor basis is by establishing a maximum bond distance covered by them. Being defined over a Bravais lattice, their general form in real space is a linear combination of delta functions centered on bond positions $\mathbf{R}_b$

$$f_n(\mathbf{R}) = \sum_b g_{n,b}\, \delta(\mathbf{R} - \mathbf{R}_b)\,, \tag{3.19}$$

with coefficients $g_{n,b}$. These coefficients are constrained by the requirement that the basis be orthonormal

$$\begin{aligned} \sum_n f_n^*(\mathbf{R}')\, f_n(\mathbf{R}) &= \delta(\mathbf{R} - \mathbf{R}')\,, \\ \sum_{\mathbf{R}} f_m^*(\mathbf{R})\, f_n(\mathbf{R}) &= \delta_{n,m}\,, \end{aligned} \tag{3.20}$$

which yields

$$\begin{aligned} \sum_n \left(g_{n,b'}\right)^* g_{n,b} &= \delta(\mathbf{R}_b - \mathbf{R}_{b'})\,, \\ \sum_b \left(g_{m,b}\right)^* g_{n,b} &= \delta_{n,m}\,. \end{aligned} \tag{3.21}$$

Unless otherwise specified, we will always work with a particular choice of $g_{n,b}$ coefficients, namely those given by the character table of the underlying lattice point group. This ensures that they transform according to irreducible representations of the lattice point group, facilitating the exploitation of symmetries, summarized in Sec. 3.3.3. Moreover, the use of lattice harmonics as form factors allows for a direct physical interpretation of the flow of bosonic propagators. When a propagator signals an instability towards emergent order, the form factor components which diverge to strong coupling indicate the symmetry of the induced order parameter. Since the point group operations involve only rotations and reflections, this choice automatically groups bond combinations in shells of a given radius. In addition, with the appropriate normalization, form factors can be chosen to satisfy $f_n^*(\mathbf{R}) = f_n(-\mathbf{R})$ which renders them real valued in momentum space, and either purely real or purely imaginary in

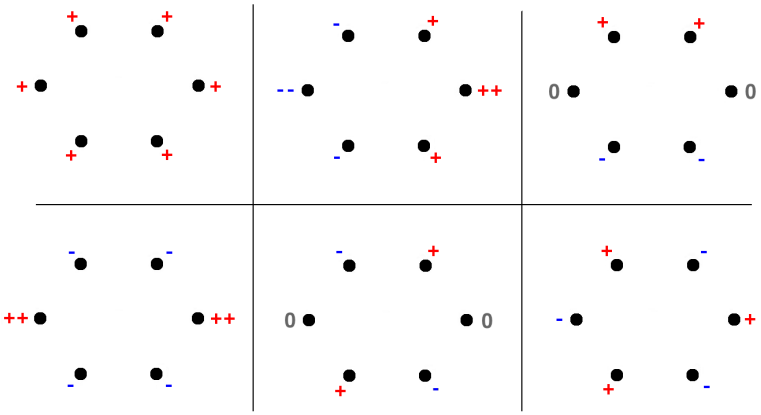

Figure 3.3.: Shell of nearest-neighbor bonds and the corresponding coefficients (prior to normalization) for real space form factors in the basis of irreducible representations for the C_{6v} group. Double plus and minus signs indicate a coefficient of ± 2.

real space. They also have a well defined parity. As a brief example, the zeroth shell of plain s-wave symmetry just consists of an on-site form factor, corresponding to a constant in wavevector space, and the first shell for the C_{6v} group is illustrated in Fig. 3.3, with its sign structure in momentum space depicted in Fig. 3.4. See App. C for a detailed construction of the irreducible form factor basis with C_{6v} symmetry.

Another choice is to set $g_{n,b} = \delta_{n,b}$, which yields a basis in terms of individual bond vectors. In this basis, form factors are real valued in position space. This may be more convenient for real space sums, as done in the coming inter-channel projections, where one would rather have form factors representing a single bond vector rather than combinations of them. Overall, the basis of irreducible representations will be generally preferred to the individual bond basis. Transformations between the two bases take the form

$$B^{(i)}_{m,n}(\mathbf{l}) = \sum_{m',n'} T^{(ib)}_{m,n,m',n'}\, B^{(b)}_{m',n'}(\mathbf{l}) \tag{3.22}$$

where band indices have been omitted, $B \in \{P, D, C\}$, and (i) and (b) indicate irreducible representation and individual bond bases, respectively. The form of the transformation elements $\mathbf{T}^{(ib)}$ can be traced back to

$$\begin{aligned} B^{(i)}_{m,n}(\mathbf{l}) &= \int d\mathbf{k}\, d\mathbf{k}' \left(f^{(i)}_m(\mathbf{k})\right)^* f^{(i)}_n(\mathbf{k}')\, \Phi^{\mathrm{B}}_{\mathbf{l},\mathbf{k},\mathbf{k}'} \\ &= \int d\mathbf{k}\, d\mathbf{k}' \left(f^{(i)}_m(\mathbf{k})\right)^* f^{(i)}_n(\mathbf{k}') \sum_{m',n'} f^{(b)}_{m'}(\mathbf{k}) \left(f^{(b)}_{n'}(\mathbf{k}')\right)^* B^{(b)}_{m',n'}(\mathbf{l})\,, \end{aligned} \tag{3.23}$$

which implies

$$\begin{aligned} T^{(ib)}_{m,n,m',n'} &= \int d\mathbf{k}\, d\mathbf{k}' \left(f^{(i)}_m(\mathbf{k})\right)^* f^{(i)}_n(\mathbf{k}')\, f^{(b)}_{m'}(\mathbf{k}) \left(f^{(b)}_{n'}(\mathbf{k}')\right)^* \\ &= \sum_{\mathbf{R}} \left(f^{(i)}_m(\mathbf{R})\right)^* f^{(b)}_{m'}(\mathbf{R}) \sum_{\mathbf{R}'} f^{(i)}_n(\mathbf{R}') \left(f^{(b)}_{n'}(\mathbf{R}')\right)^* \\ &= \left(f^{(i)}_m(\mathbf{R}_{m'})\right)^* f^{(i)}_n(\mathbf{R}_{n'}) \\ &= \left(g^{(i)}_{m,m'}\right)^* g^{(i)}_{n,n'}\,, \end{aligned} \tag{3.24}$$

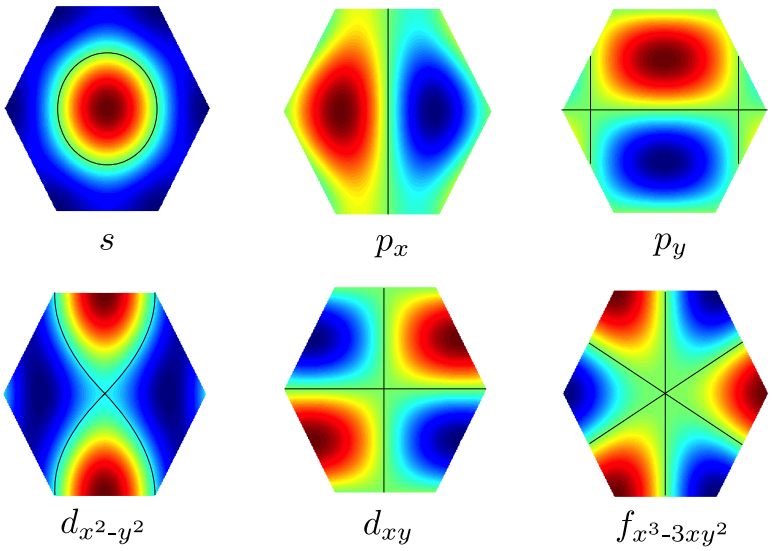

Figure 3.4.: Sign structure of the first shell of form factors in momentum space, with positive maxima in dark red, negative minima in dark blue, and nodal lines in black. The second shell contains the lowest harmonic of the irreducible representation B_1, an f-wave form factor with nodal lines crossing the corners of the Brillouin zone. The first representative of the remaining irreducible representation, A_2, is an i-wave form factor in the fourth shell, with six nodal lines.

where we made use of the fact that there is a one-to-one correspondence between bond and form factor indices in the individual bond basis. For the abuse of notation involved in treating form factor indices as bond indices to make sense, an equal indexation of bonds in both bases is assumed. The inverse transformation elements read

$$T^{(bi)}_{m,n,m',n'} = g^{(i)}_{m',m} \left(g^{(i)}_{n',n} \right)^* . \tag{3.25}$$

A further possibility, whose advantages and drawbacks lie somewhere inbetween the two previous form factor bases, is to define form factors as bond pairs of the form $\delta(\mathbf{R}-\mathbf{R}_b)\pm\delta(\mathbf{R}+\mathbf{R}_b)$. This makes it possible to have them real valued in momentum space, and with a well defined parity, without necessarily including as many bonds per form factor as in the irreducible representation basis.

The truncation does not need to be done at the same maximal bond distance for all three channels. Depending on the situation, contributions from higher harmonics in a given channel may have a much stronger influence than in the other two, where they could be neglected. However, due to the additional approximation done in the TUfRG by inserting a truncated partition of unity in mixed boson-fermion loops, the truncation will directly affect the accuracy of inter-channel feedback, as discussed in the following Sec. 3.3.2. We will thus truncate all channels in the same way, keeping as many possible terms in all channels.

For multiorbital systems, the form factors must also incorporate additional orbital indices that dictate how they are affected by point group operations. For instance, in bipartite lattices like the honeycomb lattice considered in this thesis, some group operations map sublattices onto each other. In contrast, the form factors need no additional indices for descriptions in band picture, since band indices transform trivially

under point group operations. Thus, it will be more economical to do the form factor expansions directly in band picture. There is no defined transformation from band to orbital picture for objects like the bosonic propagators or projected coupling functions, since they do not have the full momentum structure of the original coupling function. The information about the multiatomic nature of the system is encoded in the band index dependences of bosonic propagators and projected Vs. Although we compute the RG flow in band picture, we rely on the orbital picture for the initialization of the bare coupling function, which poses some difficulties in calculating the initial condition for the projected Vs, summarized in Sec. 3.3.4. Also, results at the end of the flow are usually easier to visualize in orbital picture, which requires a reconstruction of the full coupling function. For such interpretation purposes, it generally suffices to do a partial reconstruction of the coupling function in orbital picture where only the momentum transfer dependence of the dominating channel is kept. The two remaining transfer momenta are set to fixed values so that external momenta lie at the Fermi surface.

3.3.2. Inter-channel projections

The three projected Vs appearing in Eq. (3.18) are obtained via

$$\begin{aligned}
\mathbf{V}^{\mathrm{P}}(\mathbf{l}) &= \hat{P}\left[V^{\Omega_0}\right](\mathbf{l}) - \mathbf{P}(\mathbf{l}) + \hat{P}\left[\Phi^{\mathrm{C}}\right](\mathbf{l}) + \hat{P}\left[\Phi^{\mathrm{D}}\right](\mathbf{l}),\\
\mathbf{V}^{\mathrm{C}}(\mathbf{l}) &= \hat{C}\left[V^{\Omega_0}\right](\mathbf{l}) - \hat{C}\left[\Phi^{\mathrm{P}}\right](\mathbf{l}) + \mathbf{C}(\mathbf{l}) + \hat{C}\left[\Phi^{\mathrm{D}}\right](\mathbf{l}),\\
\mathbf{V}^{\mathrm{D}}(\mathbf{l}) &= \hat{D}\left[V^{\Omega_0}\right](\mathbf{l}) - \hat{D}\left[\Phi^{\mathrm{P}}\right](\mathbf{l}) + \hat{D}\left[\Phi^{\mathrm{C}}\right](\mathbf{l}) + \mathbf{D}(\mathbf{l}),
\end{aligned} \tag{3.26}$$

where again boldface objects are shorthand tensor notation for the various band and form factor index dependences. As explained in Sec. 3.2, the single-channel coupling functions are expanded in their weak momentum dependences so that each projection above amounts to integrals of bosonic propagators together with four form factors. Explicitly, they read

$$\begin{aligned}
\hat{P}\left[\Phi^{\mathrm{D}}\right]^{b_1\ldots b_4}_{m,n}(\mathbf{l}) &= \int d\mathbf{k}\, d\mathbf{k}'\, f^*_m(\mathbf{k})\, f_n(\mathbf{k}')\, \Phi^{\mathrm{D},\, b_1\ldots b_4}_{\mathbf{k}-\mathbf{k}',\, \frac{\mathbf{l}+\mathbf{k}+\mathbf{k}'}{2},\, \frac{\mathbf{l}-\mathbf{k}-\mathbf{k}'}{2}}\\
&= \int d\mathbf{k}\, d\mathbf{k}'\, f^*_m(\mathbf{k})\, f_n(\mathbf{k}')\\
&\quad \times \sum_{m',n'} f_{m'}\left(\frac{\mathbf{l}+\mathbf{k}+\mathbf{k}'}{2}\right) f^*_{n'}\left(\frac{\mathbf{l}-\mathbf{k}-\mathbf{k}'}{2}\right) D^{b_1\ldots b_4}_{m',n'}(\mathbf{k}-\mathbf{k}'),
\end{aligned} \tag{3.27}$$

$$\begin{aligned}
\hat{P}\left[\Phi^{\mathrm{C}}\right]^{b_1\ldots b_4}_{m,n}(\mathbf{l}) &= \int d\mathbf{k}\, d\mathbf{k}'\, f^*_m(\mathbf{k})\, f_n(\mathbf{k}')\, \Phi^{\mathrm{C},\, b_1\ldots b_4}_{\mathbf{k}+\mathbf{k}',\, \frac{\mathbf{l}+\mathbf{k}-\mathbf{k}'}{2},\, \frac{\mathbf{l}-\mathbf{k}+\mathbf{k}'}{2}}\\
&= \int d\mathbf{k}\, d\mathbf{k}'\, f^*_m(\mathbf{k})\, f_n(\mathbf{k}')\\
&\quad \times \sum_{m',n'} f_{m'}\left(\frac{\mathbf{l}+\mathbf{k}-\mathbf{k}'}{2}\right) f^*_{n'}\left(\frac{\mathbf{l}-\mathbf{k}+\mathbf{k}'}{2}\right) C^{b_1\ldots b_4}_{m',n'}(\mathbf{k}+\mathbf{k}'),
\end{aligned} \tag{3.28}$$

$$\begin{aligned}\hat{D}\left[\Phi^{\mathrm{P}}\right]^{b_1\ldots b_4}_{m,n}(\mathbf{l}) &= \int d\mathbf{k}\, d\mathbf{k}'\, f^*_m(\mathbf{k})\, f_n(\mathbf{k}')\, \Phi^{\mathrm{P},\, b_1\ldots b_4}_{\mathbf{k}+\mathbf{k}',\frac{\mathbf{k}-\mathbf{k}'+\mathbf{l}}{2},\frac{\mathbf{k}-\mathbf{k}'-\mathbf{l}}{2}} \\ &= \int d\mathbf{k}\, d\mathbf{k}'\, f^*_m(\mathbf{k})\, f_n(\mathbf{k}') \\ &\quad \times \sum_{m',n'} f_{m'}\left(\frac{\mathbf{k}-\mathbf{k}'+\mathbf{l}}{2}\right) f^*_{n'}\left(\frac{\mathbf{k}-\mathbf{k}'-\mathbf{l}}{2}\right) P^{b_1\ldots b_4}_{m',n'}(\mathbf{k}+\mathbf{k}')\,, \end{aligned} \tag{3.29}$$

$$\begin{aligned}\hat{D}\left[\Phi^{\mathrm{C}}\right]^{b_1\ldots b_4}_{m,n}(\mathbf{l}) &= \int d\mathbf{k}\, d\mathbf{k}'\, f^*_m(\mathbf{k})\, f_n(\mathbf{k}')\, \Phi^{\mathrm{C},\, b_1\ldots b_4}_{\mathbf{k}-\mathbf{k}',\frac{\mathbf{k}+\mathbf{k}'+\mathbf{l}}{2},\frac{\mathbf{k}+\mathbf{k}'-\mathbf{l}}{2}} \\ &= \int d\mathbf{k}\, d\mathbf{k}'\, f^*_m(\mathbf{k})\, f_n(\mathbf{k}') \\ &\quad \times \sum_{m',n'} f_{m'}\left(\frac{\mathbf{k}+\mathbf{k}'+\mathbf{l}}{2}\right) f^*_{n'}\left(\frac{\mathbf{k}+\mathbf{k}'-\mathbf{l}}{2}\right) C^{b_1\ldots b_4}_{m',n'}(\mathbf{k}-\mathbf{k}')\,, \end{aligned} \tag{3.30}$$

$$\begin{aligned}\hat{C}\left[\Phi^{\mathrm{P}}\right]^{b_1\ldots b_4}_{m,n}(\mathbf{l}) &= \int d\mathbf{k}\, d\mathbf{k}'\, f^*_m(\mathbf{k})\, f_n(\mathbf{k}')\, \Phi^{\mathrm{P},\, b_1\ldots b_4}_{\mathbf{k}+\mathbf{k}',\frac{\mathbf{k}-\mathbf{k}'+\mathbf{l}}{2},\frac{\mathbf{k}'-\mathbf{k}+\mathbf{l}}{2}} \\ &= \int d\mathbf{k}\, d\mathbf{k}'\, f^*_m(\mathbf{k})\, f_n(\mathbf{k}') \\ &\quad \times \sum_{m',n'} f_{m'}\left(\frac{\mathbf{k}-\mathbf{k}'+\mathbf{l}}{2}\right) f^*_{n'}\left(\frac{\mathbf{k}'-\mathbf{k}+\mathbf{l}}{2}\right) P^{b_1\ldots b_4}_{m',n'}(\mathbf{k}+\mathbf{k}')\,, \end{aligned} \tag{3.31}$$

$$\begin{aligned}\hat{C}\left[\Phi^{\mathrm{D}}\right]^{b_1\ldots b_4}_{m,n}(\mathbf{l}) &= \int d\mathbf{k}\, d\mathbf{k}'\, f^*_m(\mathbf{k})\, f_n(\mathbf{k}')\, \Phi^{\mathrm{D},\, b_1\ldots b_4}_{\mathbf{k}-\mathbf{k}',\frac{\mathbf{k}+\mathbf{k}'+\mathbf{l}}{2},\frac{\mathbf{k}+\mathbf{k}'-\mathbf{l}}{2}} \\ &= \int d\mathbf{k}\, d\mathbf{k}'\, f^*_m(\mathbf{k})\, f_n(\mathbf{k}') \\ &\quad \times \sum_{m',n'} f_{m'}\left(\frac{\mathbf{k}+\mathbf{k}'+\mathbf{l}}{2}\right) f^*_{n'}\left(\frac{\mathbf{k}+\mathbf{k}'-\mathbf{l}}{2}\right) D^{b_1\ldots b_4}_{m',n'}(\mathbf{k}-\mathbf{k}')\,. \end{aligned} \tag{3.32}$$

For the sensible choices of form factor basis already discussed, their real space representation takes the form of delta functions centered at given bond positions in the lattice, or linear combinations thereof. Therefore, it is generally more convenient to perform the inter-channel projections in real space, which then amounts to just checking whether the delta functions overlap, together with the corresponding calculation of Fourier transforms. They read

$$\begin{aligned}\hat{P}\left[\Phi^{\mathrm{D}}\right]^{b_1\ldots b_4}_{m,n}(\mathbf{l}) = \sum_{\mathbf{R}_1,\mathbf{R}_2,\mathbf{R}_3} \sum_{m',n'} & f^*_m\left(\frac{\mathbf{R}_1+\mathbf{R}_2}{2}+\mathbf{R}_3\right) f_n\left(-\frac{\mathbf{R}_1+\mathbf{R}_2}{2}+\mathbf{R}_3\right) \\ & \times f_{m'}(\mathbf{R}_1)\, f^*_{n'}(\mathbf{R}_2)\, D^{b_1\ldots b_4}_{m',n'}(\mathbf{R}_3)\, e^{-i\,\mathbf{l}\cdot\left(\frac{\mathbf{R}_1-\mathbf{R}_2}{2}\right)}\,, \end{aligned} \tag{3.33}$$

$$\begin{aligned}\hat{P}\left[\Phi^{\mathrm{C}}\right]^{b_1\ldots b_4}_{m,n}(\mathbf{l}) = \sum_{\mathbf{R}_1,\mathbf{R}_2,\mathbf{R}_3} \sum_{m',n'} & f^*_m\left(\frac{\mathbf{R}_1+\mathbf{R}_2}{2}+\mathbf{R}_3\right) f_n\left(\frac{\mathbf{R}_1+\mathbf{R}_2}{2}-\mathbf{R}_3\right) \\ & \times f_{m'}(\mathbf{R}_1)\, f^*_{n'}(\mathbf{R}_2)\, C^{b_1\ldots b_4}_{m',n'}(\mathbf{R}_3)\, e^{-i\,\mathbf{l}\cdot\left(\frac{\mathbf{R}_1-\mathbf{R}_2}{2}\right)}\,, \end{aligned} \tag{3.34}$$

$$\hat{D}\left[\Phi^{\mathrm{P}}\right]^{b_1\ldots b_4}_{m,n}(\mathbf{l}) = \sum_{\mathbf{R}_1,\mathbf{R}_2,\mathbf{R}_3}\sum_{m',n'} f^*_m\left(\frac{\mathbf{R}_1-\mathbf{R}_2}{2}+\mathbf{R}_3\right) f_n\left(\frac{\mathbf{R}_1-\mathbf{R}_2}{2}-\mathbf{R}_3\right) \times f_{m'}(\mathbf{R}_1)\, f^*_{n'}(\mathbf{R}_2)\, P^{b_1\ldots b_4}_{m',n'}(\mathbf{R}_3)\, e^{-i\,\mathbf{l}\cdot\left(\frac{\mathbf{R}_1+\mathbf{R}_2}{2}\right)}, \quad (3.35)$$

$$\hat{D}\left[\Phi^{\mathrm{C}}\right]^{b_1\ldots b_4}_{m,n}(\mathbf{l}) = \sum_{\mathbf{R}_1,\mathbf{R}_2,\mathbf{R}_3}\sum_{m',n'} f^*_m\left(\frac{\mathbf{R}_1-\mathbf{R}_2}{2}+\mathbf{R}_3\right) f_n\left(-\frac{\mathbf{R}_1-\mathbf{R}_2}{2}+\mathbf{R}_3\right) \times f_{m'}(\mathbf{R}_1)\, f^*_{n'}(\mathbf{R}_2)\, C^{b_1\ldots b_4}_{m',n'}(\mathbf{R}_3)\, e^{-i\,\mathbf{l}\cdot\left(\frac{\mathbf{R}_1+\mathbf{R}_2}{2}\right)}, \quad (3.36)$$

$$\hat{C}\left[\Phi^{\mathrm{P}}\right]^{b_1\ldots b_4}_{m,n}(\mathbf{l}) = \sum_{\mathbf{R}_1,\mathbf{R}_2,\mathbf{R}_3}\sum_{m',n'} f^*_m\left(\frac{\mathbf{R}_1+\mathbf{R}_2}{2}+\mathbf{R}_3\right) f_n\left(\frac{\mathbf{R}_1+\mathbf{R}_2}{2}-\mathbf{R}_3\right) \times f_{m'}(\mathbf{R}_1)\, f^*_{n'}(\mathbf{R}_2)\, P^{b_1\ldots b_4}_{m',n'}(\mathbf{R}_3)\, e^{-i\,\mathbf{l}\cdot\left(\frac{\mathbf{R}_1-\mathbf{R}_2}{2}\right)}, \quad (3.37)$$

$$\hat{C}\left[\Phi^{\mathrm{D}}\right]^{b_1\ldots b_4}_{m,n}(\mathbf{l}) = \sum_{\mathbf{R}_1,\mathbf{R}_2,\mathbf{R}_3}\sum_{m',n'} f^*_m\left(\frac{\mathbf{R}_1-\mathbf{R}_2}{2}+\mathbf{R}_3\right) f_n\left(-\frac{\mathbf{R}_1-\mathbf{R}_2}{2}+\mathbf{R}_3\right) \times f_{m'}(\mathbf{R}_1)\, f^*_{n'}(\mathbf{R}_2)\, D^{b_1\ldots b_4}_{m',n'}(\mathbf{R}_3)\, e^{-i\,\mathbf{l}\cdot\left(\frac{\mathbf{R}_1+\mathbf{R}_2}{2}\right)}. \quad (3.38)$$

Provided that the momentum dependence of the bosonic propagators is finely discretized, as allowed by the TUfRG scheme, their Fourier transforms to real space should be accurate enough. The main inaccuracy is introduced by truncating the form factor basis, which leads to truncated sums in $\mathbf{R}_1, \mathbf{R}_2, \mathbf{R}_3$. It can be readily seen that the expressions above will only produce non-zero contributions for $\mathbf{R}_1$ and $\mathbf{R}_2$ values which are covered by the truncated basis. This limits the feedback terms (3.33) - (3.38) to a soft dependence in the transfer momentum $\mathbf{l}$. Similarly, the contributing values of the propagator arguments $\mathbf{R}_3$ are also bound by the maximal radius included in the form factor basis. Taking $\hat{P}\left[\Phi^{\mathrm{D}}\right]$ as an example, and using the individual bond basis for simplicity, where $f_n(\mathbf{R}) = \delta(\mathbf{R}-\mathbf{R}_n)$, the product of four form factors yields the overlap condition $\delta(\mathbf{R}_{n'}+\mathbf{R}_{m'}+\mathbf{R}_n-\mathbf{R}_m)$ after summation. Having that $\mathbf{R}_3 = 1/2\,(\mathbf{R}_{n'}+\mathbf{R}_{m'})+\mathbf{R}_n = -1/2\,(\mathbf{R}_{n'}+\mathbf{R}_{m'})+\mathbf{R}_m$, its maximum possible values that satisfy the overlap condition result from $\mathbf{R}_{n'}+\mathbf{R}_{m'} = \mathbf{0}$ and both $\mathbf{R}_n, \mathbf{R}_m$ taking the same bond vector value with maximal radius.

Note that the $\mathbf{R}_1$ and $\mathbf{R}_2$ vectors are constrained to the real space Bravais lattice, and since the combination $1/2(\mathbf{R}_1 \pm \mathbf{R}_2)$ can yield half integer coordinates on the lattice vector basis, $\mathbf{R}_3$ also takes half integer values. This is consistent with the translational symmetry properties of bosonic propagators and projected Vs, which are in turn inherited from the properties of the single channel coupling functions. Remember that the single channel couplings have weak dependences on the extension of the corresponding fermionic bilinears, which can only take lattice vector values, and a strong dependence on the relative distance between the bilinears' midpoints, which can take half lattice vector values. See Sec. /refsec:symmetries or App. A for more details.

Generally, the real space sums above are most conveniently evaluated in the form factor basis of individual bonds. In the form factor basis of irreducible representations, which include up to 12 bond vectors per form factor, each m, n, m', n' combination results in an upper estimate of 12^4 evaluations versus just a single one in the individual bond basis. Since the rest is calculated in the irreducible representa-

tion basis for the use of symmetries and an easier physical interpretation, one has to previously transform the bosonic propagators into the individual bond basis and afterwards transform the projected Vs back to the irreducible representation basis. In some cases, the additional cost of these transformations may overturn the benefits of using the individual bond basis. Both computations, that of feedback terms and the transformation between bases scale with the fourth power of the total number of form factors considered. Thus, in the case of a very high number of form factors it may not be worth transforming into the individual bond basis. The same is true for a low number of form factors but a very high number of momentum sampling points in $\mathbf{l}$ and several bands, since transformations would still be relatively costly, but the first few shells of form factors in the irreducible representation basis include only up to 6 bonds each.

Another relevant consideration is the fact that in the right hand side of Eqs. (3.33) - (3.38) only the bosonic propagators are dependent on the renormalization scale Ω. Therefore, the Fourier exponentials and overlap of delta functions can be computed once and pre-stored instead of having to repeat their calculation at every RG step. Inter-channel projection operations then take the form

$$\hat{B}\left[\Phi^{\tilde{\mathrm{B}}}\right]_{m,n}^{b_1\ldots b_4}(\mathbf{l}) = \int d\mathbf{q} \sum_{m',n'} A^{\mathrm{B},\tilde{\mathrm{B}}}_{m,n,m',n'}(\mathbf{q},\mathbf{l})\, \tilde{B}^{b_1\ldots b_4}_{m',n'}(\mathbf{q})\,, \tag{3.39}$$

where, for the example case of $\hat{P}\left[\Phi^{\mathrm{D}}\right]$, the object $\mathbf{A}^{\mathrm{P,D}}$ corresponds to

$$A^{\mathrm{P,D}}_{m,n,m',n'}(\mathbf{q},\mathbf{l}) = \sum_{\mathbf{R}_1,\mathbf{R}_2,\mathbf{R}_3} f^*_m\left(\frac{\mathbf{R}_1+\mathbf{R}_2}{2}+\mathbf{R}_3\right) f_n\left(-\frac{\mathbf{R}_1+\mathbf{R}_2}{2}+\mathbf{R}_3\right) \times f_{m'}\left(\mathbf{R}_1\right) f^*_{n'}\left(\mathbf{R}_2\right) e^{i\mathbf{q}\mathbf{R}_3}\, e^{-i\,\mathbf{l}\cdot\left(\frac{\mathbf{R}_1-\mathbf{R}_2}{2}\right)}\,. \tag{3.40}$$

In the irreducible representation basis of form factors, this alternative brings a considerable speedup. Unfortunately, it is only applicable for sparse samplings in momentum space and truncations with a low number of form factors. Having a fourth power scaling in number of form factors and a quadratic scaling in momentum discretization points, the $\mathbf{A}$ objects above quickly become too big to be efficiently stored. They satisfy some symmetries which can be used to mitigate the memory consumption, but the symmetry reduced objects do not allow for a contiguous memory reading in (3.39), which limits efficiency for vectorized computer implementations. Furthermore, transforming the problem from compute bound to memory bound has an overall detrimental effect on its parallel scalability. In the form factor basis of individual bonds, this latter approach does not bring much benefit since there is only one non-vanishing term in the real space sums for a given m, n, m', n' combination, as already discussed. However, due to the one-to-one correspondence between real space vectors and form factor indices in that basis, the $\mathbf{l}$ dependent part in $\mathbf{A}$ can be stored in a separate array, since the m', n' values unequivocally determine the value of $1/2(\mathbf{R}_1 \pm \mathbf{R}_2)$. This splitting leads to much smaller objects. Despite the lower memory consumption, the computation would still become memory bound for high numbers of form factors and momentum sampling points.

A better compromise follows from the fact that, in either basis, both $\mathbf{R}_3$ and $1/2(\mathbf{R}_1 \pm \mathbf{R}_2)$ are bound inside the maximal radius of the truncation, with a total number of possible values equal to the number of form factor functions. Thus, at each RG step, the Fourier transforms of bosonic propagators to real space need only be done once for each possible position vector prior to the $\mathbf{R}_3$ sum, where they are reused. One may still pre-compute and store the $\mathbf{l}$ dependent part.

3.3.3. Symmetry relations

Here we summarize some useful symmetry properties of the different objects encountered so far. These will rely on a choice of form factor basis following the irreducible representations of the lattice point group, which renders them real valued in momentum space and with a well defined parity under wavevector inversion. For simplicity, we will first discuss the symmetries satisfied in one-band systems, and extrapolate to the multiband case afterwards.

The main symmetries of bosonic propagators and projected Vs stem from those of the coupling function $V(k_1, k_2, k_3, k_4)$, which obeys

$$V(k_1, k_2, k_3, k_4) = V(k_2, k_1, k_4, k_3) \tag{3.41}$$

$$V(k_1, k_2, k_3, k_4) = \Big(V(\hat{k}_3, \hat{k}_4, \hat{k}_1, \hat{k}_2)\Big)^* = V(k_3, k_4, k_1, k_2)\,, \tag{3.42}$$

where $\hat{k} = (-\omega, \mathbf{k})$, and we subsequently made use of the fact that the coupling function is mapped to its complex conjugate under frequency inversion. In practice, since we will always set external frequencies to zero, the coupling function in a one-band system will be real. Although discrete translational invariance is assumed, and thus momentum is conserved, the more general case was written above including k_4 to clearly indicate that incoming and outgoing particles are either swapped among themselves ($1 \leftrightarrow 2$, $3 \leftrightarrow 4$) or between each other ($1 \leftrightarrow 3$, $2 \leftrightarrow 4$). The first symmetry, referred to as remnant antisymmetry in [61], follows from the analogous property of the vertex $\Gamma^{(4)}$, since $\mathcal{A}^{(4)}$ in Eq. (2.9) stays invariant under such a swap among Grassmann fields. The second symmetry, called particle hole symmetry in [61] and Osterwalder-Schrader positivity in [91], follows from the hermiticity of the Hamiltonian, or equivalently from the invariance of the partition function as functional integral under $\psi \to i\bar{\psi}$, $\bar{\psi} \to i\psi$. These symmetries translate into the single channel coupling functions as

$$\begin{aligned}
\Phi^{\mathrm{P}}_{\mathbf{l},\mathbf{k},\mathbf{k}'} &= \Phi^{\mathrm{P}}_{\mathbf{l},-\mathbf{k},-\mathbf{k}'} = \Phi^{\mathrm{P}}_{\mathbf{l},\mathbf{k}',\mathbf{k}}\,,\\
\Phi^{\mathrm{C}}_{\mathbf{l},\mathbf{k},\mathbf{k}'} &= \Phi^{\mathrm{C}}_{-\mathbf{l},\mathbf{k}',\mathbf{k}} = \Phi^{\mathrm{C}}_{\mathbf{l},\mathbf{k}',\mathbf{k}}\,,\\
\Phi^{\mathrm{D}}_{\mathbf{l},\mathbf{k},\mathbf{k}'} &= \Phi^{\mathrm{D}}_{-\mathbf{l},\mathbf{k}',\mathbf{k}} = \Phi^{\mathrm{D}}_{-\mathbf{l},\mathbf{k},\mathbf{k}'}\,,
\end{aligned}$$

where the first and second equality in each line corresponds to the symmetries (3.41) and (3.42), respectively.

From these relations it follows that both the bosonic propagators and projected Vs are symmetric under the exchange of form factor indices

$$\begin{aligned}
B_{m,n}(\mathbf{l}) &= B_{n,m}(\mathbf{l})\,,\\
V^{\mathrm{B}}_{m,n}(\mathbf{l}) &= V^{\mathrm{B}}_{n,m}(\mathbf{l})
\end{aligned}$$

with $B \in \{P, C, D\}$. Moreover, it also follows that

$$\begin{aligned}
P_{m,n}(\mathbf{l}) &= \pi_m \pi_n\, P_{m,n}(\mathbf{l})\,,\\
C_{m,n}(\mathbf{l}) &= C_{m,n}(-\mathbf{l})\,,\\
D_{m,n}(\mathbf{l}) &= D_{m,n}(-\mathbf{l})
\end{aligned} \tag{3.43}$$

where π_m denotes the parity eigenvalue of the m-th form factor, $f_m(-\mathbf{k}) = \pi_m\, f_m(\mathbf{k})$. Analogous relations hold for the projected Vs. Since the form factors are chosen to transform with irreducible representations of the point group, some form factor

components of propagators and projected Vs vanish at points of high symmetry in the Brillouin zone due to Schur's second lemma [90]. The point group symmetries allow to reduce the description of momentum dependences to the irreducible Brillouin zone. Whereas the coupling function transforms trivially under point group operations $\hat{S}$, the form factors are generally mapped onto a linear combination in their basis, whose coefficients $C^{\hat{S}}_{m,\tilde{m}}$ allow to compose $f_m\left(\hat{S}\,\mathbf{k}\right)$, i.e.,

$$f_m\left(\hat{S}\,\mathbf{k}\right) = \sum_{\tilde{m}} C^{\hat{S}}_{m,\tilde{m}}\, f_{\tilde{m}}\left(\mathbf{k}\right) .$$

With that, point group symmetries can be exploited via

$$B_{m,n}\left(\hat{S}\,\mathbf{l}\right) = \sum_{\tilde{m},\tilde{n}} C^{\hat{S}}_{m,\tilde{m}} C^{\hat{S}}_{n,\tilde{n}} B_{\tilde{m},\tilde{n}}(\mathbf{l}) \tag{3.44}$$

and analogously for projected Vs.

In the multiorbital case, the symmetries (3.41) and (3.42) involve an additional exchange of orbital or band indices, and interactions are not necessarily real anymore. In band picture and momentum space they read

$$\begin{aligned} V^{b_1b_2b_3b_4}(\mathbf{k}_1,\mathbf{k}_2,\mathbf{k}_3,\mathbf{k}_4) &= V^{b_2b_1b_4b_3}(\mathbf{k}_2,\mathbf{k}_1,\mathbf{k}_4,\mathbf{k}_3) \\ V^{b_1b_2b_3b_4}(\mathbf{k}_1,\mathbf{k}_2,\mathbf{k}_3,\mathbf{k}_4) &= \left(V^{b_3b_4b_1b_2}(\mathbf{k}_3,\mathbf{k}_4,\mathbf{k}_1,\mathbf{k}_2)\right)^* . \end{aligned}$$

For the honeycomb lattice considered in this thesis, bare interactions between charge bilinears will be real in orbital picture and position space, as detailed in Sec. 3.3.4. However, having a bipartite lattice, they are complex in momentum space, both for the orbital and band pictures. In the case of an overall real coupling function in orbital picture, whether it stays real or not in band picture depends on the definition for the transformation (2.19). In multiband systems, the exchange of form factor indices takes the form

$$\begin{aligned} P^{b_1b_2b_3b_4}_{m,n}(\mathbf{l}) &= \left(P^{b_3b_4b_1b_2}_{n,m}(\mathbf{l})\right)^* , \\ C^{b_1b_2b_3b_4}_{m,n}(\mathbf{l}) &= \left(C^{b_3b_4b_1b_2}_{n,m}(\mathbf{l})\right)^* , \\ D^{b_1b_2b_3b_4}_{m,n}(\mathbf{l}) &= \left(D^{b_4b_3b_2b_1}_{n,m}(\mathbf{l})\right)^* \end{aligned} \tag{3.45}$$

and the inversion symmetries in Eqs. (3.43) now read

$$\begin{aligned} P^{b_1b_2b_3b_4}_{m,n}(\mathbf{l}) &= \pi_m\pi_n P^{b_2b_1b_4b_3}_{m,n}(\mathbf{l}) , \\ C^{b_1b_2b_3b_4}_{m,n}(\mathbf{l}) &= \left(C^{b_4b_3b_2b_1}_{m,n}(-\mathbf{l})\right)^* , \\ D^{b_1b_2b_3b_4}_{m,n}(\mathbf{l}) &= \left(D^{b_3b_4b_1b_2}_{m,n}(-\mathbf{l})\right)^* \end{aligned} \tag{3.46}$$

with analogous relations being satisfied by the projected Vs. The exploit of point group symmetries in the $\mathbf{l}$ dependence can be done as in Eq. (3.44) for the single band case, provided that one chooses a suitable Bloch basis in band picture which also transforms trivially under point group operations [90]. In addition, if the system's dispersion satisfies some given symmetries under the exchange of band indices, these will in turn become manifest in the bosonic propagators and projected Vs. For instance, the Hubbard model on the honeycomb lattice considered in this work has a symmetric band structure respect to the Fermi level for zero chemical potential. The dispersion satisfies $\epsilon^b(\mathbf{k}) = -\epsilon^{\hat{b}}(\mathbf{k})$, where if b is the upper band, $\hat{b}$ denotes the lower

band and vice versa. This translates to

$$B^{b_1 b_2 b_3 b_4}_{m,n}(\mathbf{l}) = B^{\hat{b}_1 \hat{b}_2 \hat{b}_3 \hat{b}_4}_{m,n}(\mathbf{l}) \,,$$
$$V^{\mathrm{B},\, b_1 b_2 b_3 b_4}_{m,n}(\mathbf{l}) = V^{\mathrm{B},\, \hat{b}_1 \hat{b}_2 \hat{b}_3 \hat{b}_4}_{m,n}(\mathbf{l})$$

with $B \in \{P, C, D\}$. The manifestation of this symmetry can be seen from the transformation elements (3.51) introduced in Sec. 3.3.4.

Since the form factors are real, form factor projected bubbles are also real, and it can be directly read from their definition in Eq. (3.16) that they are symmetric under form factor index exchange

$$\chi^{\mathrm{pp/ph}}_{m,n}(\mathbf{l}) \;=\; \chi^{\mathrm{pp/ph}}_{n,m}(\mathbf{l}) \,.$$

An inversion of the integration variable shows that in the particle-particle case only elements corresponding to form factors with the same parity may be nonzero

$$\chi^{\mathrm{pp}}_{m,n}(\mathbf{l}) \;=\; \pi_m \, \pi_n \, \chi^{\mathrm{pp}}_{m,n}(\mathbf{l}) \,,$$

which is consistent with the fact that since $\mathbf{P}$ and $\mathbf{V}^{\mathrm{P}}$ satisfy that same property, no nonzero elements with mixed parity (i.e. $\pi_m \neq \pi_n$) should be generated in the RG flow of P. An analogous property holds for the particle-hole bubble if the dispersion is inversion symmetric, $\epsilon(\mathbf{k}) = \epsilon(-\mathbf{k})$.

The usage of point group symmetries yields

$$\chi^{\mathrm{pp/ph}}_{m,n}\left(\hat{S}\,\mathbf{l}\right) \;=\; \sum_{\tilde{m},\tilde{n}} C^{\hat{S}}_{m,\tilde{m}} \, C^{\hat{S}}_{n,\tilde{n}} \, \chi^{\mathrm{pp/ph}}_{\tilde{m},\tilde{n}} \left(\mathbf{l}\right) \,.$$

In a multiband system, the form factor exchange and point group symmetries apply just as in the single band case. The parity relations only hold for intra-band components in the general case. For band symmetric situations like the honeycomb lattice system at half filling, there is also the additional symmetry

$$\chi^{\mathrm{pp/ph},\, bb'}_{m,n}(\mathbf{l}) \;=\; \chi^{\mathrm{pp/ph},\, \hat{b}\hat{b}'}_{m,n}(\mathbf{l}) \,,$$

which leads to the parity relations also holding for inter-band components. The fulfillment of band symmetries can be explicitly seen in the loop integrand for the Ω-regulated flow in App. B.

For the aforementioned possibility of calculating the scale independent parts of the projection operations at the start of the flow and storing them, exploiting symmetries can reduce the substantial increase in memory usage. The objects $\mathbf{A}^{\mathrm{B},\tilde{\mathrm{B}}}$ from Eq. (3.39) are all real valued, and the 6 possible combinations of $B, \tilde{B}$ are related in pairs

$$\mathbf{A}^{\mathrm{P,C}} = \pi_n \mathbf{A}^{\mathrm{P,D}} \,,$$
$$\mathbf{A}^{\mathrm{C,P}} = \pi_{n'} \mathbf{A}^{\mathrm{D,P}} \,,$$
$$\mathbf{A}^{\mathrm{D,C}} = \mathbf{A}^{\mathrm{C,D}}$$

so that only three of them have to be computed and stored. Furthermore, each of

these has given symmetries with respect to the exchange of form factor indices

$$\begin{aligned}
A^{\mathrm{P,D}}_{n,m,m',n'}(\mathbf{q},\mathbf{l}) &= A^{\mathrm{P,D}}_{m,n,m',n'}(-\mathbf{q},\mathbf{l})\,,\\
A^{\mathrm{P,D}}_{m,n,n',m'}(\mathbf{q},\mathbf{l}) &= \pi_m\pi_n A^{\mathrm{P,D}}_{m,n,m',n'}(-\mathbf{q},\mathbf{l})\,,\\
A^{\mathrm{D,P}}_{n,m,m',n'}(\mathbf{q},\mathbf{l}) &= \pi_m\pi_n A^{\mathrm{D,P}}_{m,n,m',n'}(-\mathbf{q},\mathbf{l})\,,\\
A^{\mathrm{D,P}}_{m,n,n',m'}(\mathbf{q},\mathbf{l}) &= \pi_m\pi_n\pi_{m'}\pi_{n'} A^{\mathrm{D,P}}_{m,n,m',n'}(-\mathbf{q},\mathbf{l})\,,\\
A^{\mathrm{C,D}}_{n,m,m',n'}(\mathbf{q},\mathbf{l}) &= A^{\mathrm{C,D}}_{m,n,m',n'}(-\mathbf{q},\mathbf{l})\,,\\
A^{\mathrm{C,D}}_{m,n,n',m'}(\mathbf{q},\mathbf{l}) &= \pi_m\pi_n\pi_{m'}\pi_{n'} A^{\mathrm{C,D}}_{m,n,m',n'}(-\mathbf{q},\mathbf{l})\,,
\end{aligned} \tag{3.47}$$

and all of them fulfill the following symmetry under momentum inversion

$$A^{\mathrm{B,B'}}_{m,n,m',n'}(-\mathbf{q},-\mathbf{l}) = \pi_m\pi_n\pi_{m'}\pi_{n'} A^{B,B'}_{m,n,m',n'}(\mathbf{q},\mathbf{l})\,.$$

The use of point group symmetries reads

$$A^{B,B'}_{m,n,m',n'}(\hat{S}\,\mathbf{q},\hat{S}\,\mathbf{l}) = \sum_{\tilde{m},\tilde{n},\tilde{m}',\tilde{n}'} C^{\hat{S}}_{m,\tilde{m}}\, C^{\hat{S}}_{n,\tilde{n}}\, C^{\hat{S}}_{m',\tilde{m}'}\, C^{\hat{S}}_{n',\tilde{n}'}\, A^{B,B'}_{\tilde{m},\tilde{n},\tilde{m}',\tilde{n}'}(\mathbf{q},\mathbf{l})\,.$$

The relations in Eqs. (3.47) can be used to draw additional conclusions about the feedback terms $\hat{B}\left[\Phi^{\tilde{\mathrm{B}}}\right]$. For example, from the symmetry of bosonic propagators and projected Vs under exchange of form factor indices, having that $\hat{P}\left[\Phi^{\mathrm{C/D}}\right]$ should respect that same symmetry automatically leads to

$$\hat{P}\left[\Phi^{\mathrm{C/D}}\right]_{m,n}(\mathbf{l}) = \pi_m\pi_n \hat{P}\left[\Phi^{\mathrm{C/D}}\right]_{m,n}(\mathbf{l})\,,$$

which is consistent with the fact that $\mathbf{V}^{\mathrm{P}}$ has no nonzero elements with mixed parity. Applying the same reasoning to the feedback among C and D channels leads to a more interesting consequence

$$\hat{D}\left[\Phi^{\mathrm{C}}\right]_{m,n}(\mathbf{l}) = \pi_m\pi_n \sum_{m',n'} \pi_{m'}\pi_{n'} \int d\mathbf{q}\, A^{\mathrm{D,C}}_{m,n,m',n'}(\mathbf{q},\mathbf{l})\, C_{m',n'}(\mathbf{q})\,,$$

and equivalently for $\hat{C}\left[\Phi^{\mathrm{D}}\right]$, which means that there is no cross talk between pure parity and mixed parity components in the feedback between particle-hole channels.

The symmetries of the $\mathbf{A}^{\mathrm{B},\tilde{\mathrm{B}}}$ objects apply regardless of whether the system is a single-band or multiband one, since they do not carry band indices. However, the latter parity properties of feedback terms do not generally transfer to the multiband case.

Lastly, we also comment on the translational symmetry properties of the objects encountered so far. For a translationally invariant system, the coupling function $V(\mathbf{k}_1,\mathbf{k}_2,\mathbf{k}_3)$ is in turn invariant under translations of any of its momentum arguments by a reciprocal lattice vector $\mathbf{G}$. After the rearrangement of wavevector dependences involved in the definition of the single channel coupling functions, the translational

symmetries imply

$$\begin{aligned}\Phi^{\mathrm{P}}_{\mathbf{l},\mathbf{k},\mathbf{k}'} &= \Phi^{\mathrm{P}}_{\mathbf{l}+\mathbf{G},\,\mathbf{k}+\frac{\mathbf{G}}{2},\,\mathbf{k}'-\frac{\mathbf{G}}{2}} \\ &= \Phi^{\mathrm{P}}_{\mathbf{l}+\mathbf{G},\,\mathbf{k}-\frac{\mathbf{G}}{2},\,\mathbf{k}'-\frac{\mathbf{G}}{2}} \\ &= \Phi^{\mathrm{P}}_{\mathbf{l}+\mathbf{G},\,\mathbf{k}-\frac{\mathbf{G}}{2},\,\mathbf{k}'+\frac{\mathbf{G}}{2}}\end{aligned}$$

for the example of the pairing channel, under the translations $\mathbf{k}_1 \to \mathbf{k}_1 + \mathbf{G}$, $\mathbf{k}_2 \to \mathbf{k}_2 + \mathbf{G}$, and $\mathbf{k}_3 \to \mathbf{k}_3 + \mathbf{G}$, respectively. From these, it can be seen that $\Phi^{\mathrm{P}}_{\mathbf{l},\mathbf{k},\mathbf{k}'}$ is symmetric under reciprocal vector translations in $\mathbf{k}$ and $\mathbf{k}'$, but only under translations of $2\mathbf{G}$ in $\mathbf{l}$. The same conclusion follows for the other two channels. Nevertheless, as it will be shown in the following, the full information about the transfer momentum dependence is still fully contained in the first Brillouin zone. The translational symmetry properties of the weak momentum dependences underly our choices for an appropriate form factor basis. As already mentioned, in a real space formulation of the form $\Phi^{\mathrm{B}}_{\mathbf{R}_B,\mathbf{R}_\mathbf{k},\mathbf{R}_{\mathbf{k}'}}$, the weak dependences on $\mathbf{R}_\mathbf{k}$ and $\mathbf{R}_{\mathbf{k}'}$ represent the extension of the corresponding fermionic bilinears, whose possible values are defined on the Bravais lattice, and the strong dependence $\mathbf{R}_B$ represents the relative distance between the midpoints of the bilinears involved, and is therefore defined on a smaller lattice with a lattice constant which is a half of the original one. As shown in App. A, whether $\mathbf{R}_B$ is a lattice vector or half a lattice vector ultimately depends on $\mathbf{R}_\mathbf{k}$ and $\mathbf{R}_{\mathbf{k}'}$, taking the general form

$$\mathbf{R}_B = \tilde{\mathbf{R}} - \frac{\mathbf{R}_\mathbf{k} \pm \mathbf{R}_{\mathbf{k}'}}{2}\,,$$

where $\tilde{\mathbf{R}}$ is a Bravais lattice vector. Therefore, the single channel couplings in momentum space will either be symmetric or antisymmetric under translation of $\mathbf{l}$ by a reciprocal lattice vector. This is also true for bosonic propagators and projected Vs in the individual bond basis of form factors, where form factor indices denote a unique value for $\mathbf{R}_\mathbf{k}$ and $\mathbf{R}_{\mathbf{k}'}$. In the form factor basis of irreducible representations, they have a mixed nature, with their symmetric and antisymmetric contributions being nonetheless picked apart in the real space sums of the interchannel projections. For the Fourier transforms of bosonic propagators to real space it suffices to integrate over the first Brillouin zone, because for antisymmetric components the sign change in further Brillouin zones is cancelled by another sign coming from the Fourier phase factor. It is straightforward to corroborate that for a half lattice vector $\mathbf{R}_B$, since $\mathbf{R}_B \cdot \mathbf{G} = n\pi$ with n being odd, then the integrand is indeed symmetric under translations by $\mathbf{G}$

$$\begin{aligned}B_{m,n}(\mathbf{R}_B) &= \int d\mathbf{q}\, e^{i\mathbf{q}\cdot\mathbf{R}_B} B_{m,n}(\mathbf{q}) = \int d\mathbf{q}\, e^{i(\mathbf{q}+\mathbf{G})\cdot\mathbf{R}_B} B_{m,n}(\mathbf{q}+\mathbf{G}) \\ &= \int d\mathbf{q}\, e^{i\mathbf{q}\cdot\mathbf{R}_B} e^{in\pi}\,(-B_{m,n}(\mathbf{q})) = \int d\mathbf{q}\, e^{i\mathbf{q}\cdot\mathbf{R}_B} B_{m,n}(\mathbf{q})\,,\end{aligned}$$

where the bosonic propagator was assumed to be in the individual bond basis.

All these translational symmetry properties also apply in multiorbital systems.

3.3.4. Initialization procedure

As explained in Sec. 2.1 about the functional Renormalization Group, the flow of the generating functional for one-particle irreducible vertex functions starts at an

infinite energy scale where the generating functional takes the form of the bare action. Assuming that there are only pairwise interactions at the bare level, a complete description of the system is contained in the level-2 truncation of the hierarchy for vertex functions. The initial condition for the SU(2) symmetric flow equations of Sec. 2.3 is then the bare coupling function. In practice, numerical calculations start at a finite energy scale Ω_0. For the common choice of a momentum-shell cutoff as regulator, which takes the the form of a step function i.e. $\Theta\left(|\epsilon\left(\mathbf{k}\right)| - \Omega\right)$, the initial energy scale can be set at the value of the bandwidth W because the regulated loop integrals are zero above W. However, with the frequency regulator of the Ω-scheme introduced in Sec. 2.4, the loops have support at all finite energies. Therefore, Ω_0 is chosen to take a high enough value so that the bubbles are sufficiently suppressed. The results at the end of the flow generally converge respect to Ω_0 when it is set to be two to three orders of magnitude larger than the bandwidth.

For the sake of generality and unbiasedness, the initial bare coupling $V^{\Omega_0}_{\mathbf{k}_1,\mathbf{k}_2,\mathbf{k}_3}$ was kept as a separate term in the channel decompositions of Sec. 3.1. This way, bosonic propagators are zero at the start of the flow, and the initial conditions for projected Vs are the corresponding channel projections of the bare coupling function. However, in practice it may be more convenient to assign the channel projections of V^{Ω_0} as initial condition in the bosonic propagators, especially when dealing with long-ranged Coulomb interactions, as it will be explained at the end of this section. The explicit V^{Ω_0} term is then absent in the decomposition, and both the bosonic propagators and projected Vs share the same initial condition in each channel.

We will consider the following general form for the interaction part of the Hamiltonian H_{int}, consisting on an onsite-U term and non-local density-density contributions

$$\begin{aligned} H_{\text{int}} = & U \sum_{i,o} n_{i,o,\uparrow} n_{i,o,\downarrow} \\ & + \sum_{\substack{i \neq j,\, o,o' \\ \sigma,\sigma'}} \frac{U^{o,o'}_{i,j}}{2} n_{i,o,\sigma} n_{j,o',\sigma'} \,, \end{aligned}$$

where $n_{i,o,\sigma} = c^{\dagger}_{i,o,\sigma} c_{i,o,\sigma}$ represents the electron density operator, with $c^{(\dagger)}_{i,o,\sigma}$ annihilating (creating) an electron at site i in sublattice o with spin $\sigma \in \{\uparrow,\downarrow\}$, and interaction coefficients read

$$U^{o,o'}_{i,j} = U_{i,j} \begin{cases} \delta_{o,o'} & \text{for intra-orbital } (i,j) \text{ pairs} \\ 1 - \delta_{o,o'} & \text{for inter-orbital } (i,j) \text{ pairs} \end{cases} \tag{3.48}$$

For better clarity when Fourier transforming the interaction, and to connect to previous notation, we will denote these coefficients via a coupling function in real space and orbital picture i.e. $V^{o_1 o_2 o_3 o_4}(\mathbf{R}_1, \mathbf{R}_2, \mathbf{R}_3, \mathbf{R}_4)$ with $\mathbf{R}_1 = \mathbf{R}_3$, $o_1 = o_3$ and $\mathbf{R}_2 = \mathbf{R}_4$, $o_2 = o_4$ since the bare interactions involve just local density bilinears. One then has

$$V^{o_1 \cdots o_4}(\mathbf{R}_1 - \mathbf{R}_2, \mathbf{0}, \mathbf{R}_1 - \mathbf{R}_2, \mathbf{0}) = \tilde{V}^{o_1 \cdots o_4}(\mathbf{R}_n) = \left(U \delta_{n,0} \delta_{o_1,o_2} + U^{o_1,o_2}_{i,i+n}\right) \delta_{o_1,o_3} \delta_{o_2,o_4} \,,$$

with $\mathbf{R}_n = \mathbf{R}_1 - \mathbf{R}_2$ denoting n^{th} nearest neighbor bond distances on the actual lattice including the different sublattice positions. The coupling strengths for $\tilde{V}^{o_1 \cdots o_4}(\mathbf{R}_n)$ acting at a given $\mathbf{R}_n$ will often be just denoted by V_n. Transforming the bare coupling function to momentum space and band picture via Eq. (2.19) yields

$$V^{b_1 \ldots b_4}(\mathbf{k}_1, \mathbf{k}_2, \mathbf{k}_3) = \sum_{\substack{o_1 o_2 \\ o_3 o_4}} \sum_{\mathbf{R}_n} \tilde{V}^{o_1 \ldots o_4}(\mathbf{R}_n)\, e^{i(\mathbf{k}_3 - \mathbf{k}_1)\cdot \mathbf{R}_n}\, \hat{T}^{b_1,o_1}_{\mathbf{k}_1}\, \hat{T}^{b_2,o_2}_{\mathbf{k}_2} \left(\hat{T}^{b_3,o_3}_{\mathbf{k}_3}\right)^* \left(\hat{T}^{b_4,o_4}_{\mathbf{k}_4}\right)^* .$$

From this last expression for V^{Ω_0}, the initial condition in each channel is obtained by applying the projections in Eqs. (3.8)

$$\begin{aligned}
\hat{P}\left[V^{\Omega_0,\,b_1\ldots b_4}\right]_{m,m'}(\mathbf{l}) &= \sum_{\substack{o_1 o_2\\ o_3 o_4}}\sum_{\mathbf{R}_n}\tilde{V}^{o_1\ldots o_4}(\mathbf{R}_n)\int d\mathbf{k}\, f^*_m(\mathbf{k})\, e^{-i\mathbf{k}\cdot\mathbf{R}_n}\hat{T}^{b_1,o_1}_{\frac{1}{2}+\mathbf{k}}\,\hat{T}^{b_2,o_2}_{\frac{1}{2}-\mathbf{k}}\\
&\quad\times\int d\mathbf{k}'\, f_{m'}(\mathbf{k}')\, e^{i\mathbf{k}'\cdot\mathbf{R}_n}\left(\hat{T}^{b_3,o_3}_{\frac{1}{2}+\mathbf{k}'}\right)^*\left(\hat{T}^{b_4,o_4}_{\frac{1}{2}-\mathbf{k}'}\right)^*,\\
\hat{C}\left[V^{\Omega_0,\,b_1\ldots b_4}\right]_{m,m'}(\mathbf{l}) &= \sum_{\substack{o_1 o_2\\ o_3 o_4}}\sum_{\mathbf{R}_n}\tilde{V}^{o_1\ldots o_4}(\mathbf{R}_n)\int d\mathbf{k}\, f^*_m(\mathbf{k})\, e^{-i\mathbf{k}\cdot\mathbf{R}_n}\hat{T}^{b_1,o_1}_{\mathbf{k}+\frac{1}{2}}\left(\hat{T}^{b_4,o_4}_{\mathbf{k}-\frac{1}{2}}\right)^*\\
&\quad\times\int d\mathbf{k}'\, f_{m'}(\mathbf{k}')\, e^{i\mathbf{k}'\cdot\mathbf{R}_n}\hat{T}^{b_2,o_2}_{\mathbf{k}'-\frac{1}{2}}\left(\hat{T}^{b_3,o_3}_{\mathbf{k}'+\frac{1}{2}}\right)^*, \qquad (3.49)\\
\hat{D}\left[V^{\Omega_0,\,b_1\ldots b_4}\right]_{m,m'}(\mathbf{l}) &= \sum_{\substack{o_1 o_2\\ o_3 o_4}}\sum_{\mathbf{R}_n}\tilde{V}^{o_1\ldots o_4}(\mathbf{R}_n)e^{-i\mathbf{l}\cdot\mathbf{R}_n}\int d\mathbf{k}\, f^*_m(\mathbf{k})\,\hat{T}^{b_1,o_1}_{\mathbf{k}+\frac{1}{2}}\left(\hat{T}^{b_3,o_3}_{\mathbf{k}-\frac{1}{2}}\right)^*\\
&\quad\times\int d\mathbf{k}'\, f_{m'}(\mathbf{k}')\,\hat{T}^{b_2,o_2}_{\mathbf{k}'-\frac{1}{2}}\left(\hat{T}^{b_4,o_4}_{\mathbf{k}'+\frac{1}{2}}\right)^*.
\end{aligned}$$

Note that in a more rigorous notation, one may also put explicit orbital dependences on the real space vectors, since each orbital subspace in the bipartite lattice contains a different set of bonds. Inter-orbital combinations in the honeycomb lattice do not form a Bravais lattice, and satisfy $\mathbf{R}_n^{oo'} = -\mathbf{R}_n^{o'o}$. Writing the initial projections in Eqs. (3.49) as an explicit sum over the real space contributions allows to factorize the four dimensional momentum integral of the projections (3.8) as a sum of products of two dimensional integrals. Furthermore, since the transformation elements for the honeycomb lattice, which are be specified below, satisfy $\hat{T}^{b,o}_{-\mathbf{k}} = \left(\hat{T}^{b,o}_{\mathbf{k}}\right)^*$, one just needs to calculate the integral

$$\int d\mathbf{k}\, f_m(\mathbf{k})\, e^{i\mathbf{k}\cdot\mathbf{R}_n}\hat{T}^{b,o}_{\mathbf{k}-\frac{1}{2}}\left(\hat{T}^{b',o'}_{\mathbf{k}+\frac{1}{2}}\right)^* \qquad (3.50)$$

for all f_m, $\mathbf{l}$, b, b', o, o' and corresponding $\mathbf{R}_n$s to construct the result of all three projections, where the D channel integrands amount to the special case involving just the on-site bond vector.

The unitary transformation $\hat{\mathbf{T}}_{\mathbf{k}}$ between orbital and band degrees of freedom in the honeycomb lattice reads

$$\begin{aligned}
\hat{\mathbf{T}}_{\mathbf{k}} &= \frac{1}{\sqrt{2}}\begin{pmatrix}\frac{h(\mathbf{k})}{|h(\mathbf{k})|} & -1\\ 1 & \frac{h^*(\mathbf{k})}{|h(\mathbf{k})|}\end{pmatrix} \qquad (3.51)\\
h(\mathbf{k}) &= \sum_{\boldsymbol{\delta}} e^{i\mathbf{k}\cdot\boldsymbol{\delta}}
\end{aligned}$$

where $\{\boldsymbol{\delta}\}$ are the three nearest neighbor bond vectors connecting the two sublattices, as shown in Fig. 3.5a. The distance between nearest neighbors is set to unity, so that they read $\boldsymbol{\delta}_1 = (\sqrt{3}/2, 1/2)$, $\boldsymbol{\delta}_2 = (-\sqrt{3}/2, 1/2)$, and $\boldsymbol{\delta}_3 = (0, -1)$. If the kinetic part of the Hamiltonian follows from a tight binding model with just nearest neighbor hopping terms of amplitude t, the dispersion then reads $\epsilon^{\pm}(\mathbf{k}) = \pm t\,|h(\mathbf{k})|$. Thus, the electronic band structure is invariant under local U(1) transformations of the form $h(\mathbf{k}) \to e^{i\phi_{\mathbf{k}}}h(\mathbf{k})$, akin to a gauge freedom. Rigorously speaking, it amounts to having different choices of Bloch basis in the transformation (3.51) rather than fixing a gauge. With a $\phi_{\mathbf{k}}$ linear in $\mathbf{k}$, it can be seen as a redefinition of $\{\boldsymbol{\delta}\}$. Our

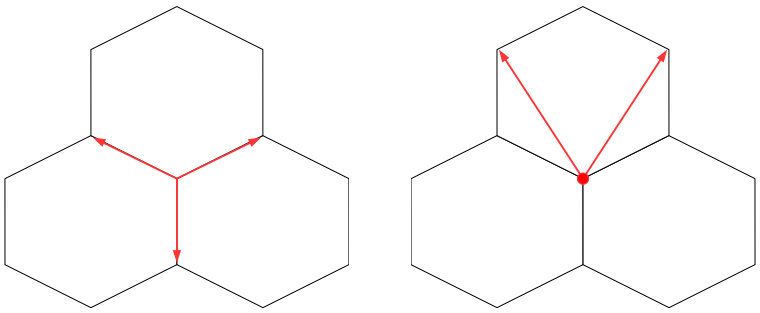

(a) (b)

Figure 3.5.: Different choices of the set $\{\boldsymbol{\delta}\}$ involved in the transformation $\hat{\mathbf{T}}_{\mathbf{k}}$ depending on the Bloch basis chosen: (a) natural basis, and (b) proper basis. In the proper basis, the third vector $\boldsymbol{\delta}_3$ is a zero vector and has been represented by a circle.

choice of Bloch basis will be that of Fig. 3.5a, which we will call the *natural basis*. Another possible choice is the so-called *proper basis* [90], which offsets one of the $\boldsymbol{\delta}$ vectors to zero, and is shown in Fig. 3.5b for $\phi_{\mathbf{k}} = -\mathbf{k} \cdot \boldsymbol{\delta}_3$. This gauge has the advantage that coupling functions respect the periodicity of reciprocal space, since the Wannier functions corresponding to different sublattices are localized on the same Bravais lattice. The transformation to band degrees of freedom involves Bravais lattice vectors only, ensuring that all the various objects in our calculations will be continuous and smooth across the borders of the Brillouin zone. In the natural basis, since $\{\boldsymbol{\delta}\}$ are half lattice vectors, $\hat{\mathbf{T}}_{\mathbf{k}}$ does not have the periodicity of reciprocal space and one must deal with discontinuities in the integrands (3.50) when back-folding them into the first Brillouin zone. The reason behind choosing the natural basis over the proper one resides in the fact that the latter obscures the otherwise symmetric momentum structure of transformation elements and inter-orbital coupling terms. For example, a first nearest neighbor interaction in the proper basis has the real space structure depicted in Fig. 3.5b, which relative to the direct lattice, looks like an on-site term plus two second nearest neighbor terms. When projected onto a form factor basis of lattice harmonics, it translates mainly into components of mixed p and d character. In contrast, in the natural basis the symmetry of intra-orbital couplings is preserved, and they mainly correspond to diagonal components in the form factor basis. The less trivial symmetry of inter-orbital coupling terms in the proper basis complicates the physical interpretation and the exploit of point group symmetries. One could switch Bloch bases at the end of the RG flow, and settle for only having a clear interpretation about the correlation's symmetry character at the end of the flow. However, since in practice the computation is not exact, the leading terms of mixed symmetry in the flow often lead to spurious behavior.

Note that the basis referred to as natural basis in Ref. [90] leads to coupling functions with the additional property of transforming trivially under all point group operations. For that matter, a piecewise definition of $\hat{\mathbf{T}}_{\mathbf{k}}$ is employed, with a different form for Brillouin zone regions of positive and negative k_x. This adds a further discontinuity along $k_x = 0$ to our choice of transformation elements, which are already challenging enough to integrate accurately. Despite transforming non-trivially, the result of point group operations in the basis of our choice is not complicated. All elements of C_{6v} can be constructed by composing reflections respect to two axes, depicted in Fig. 3.6. The coupling function is symmetric under the action of $\hat{I}_1$, inversions around the axis connecting M-points. However, it is mapped to its complex

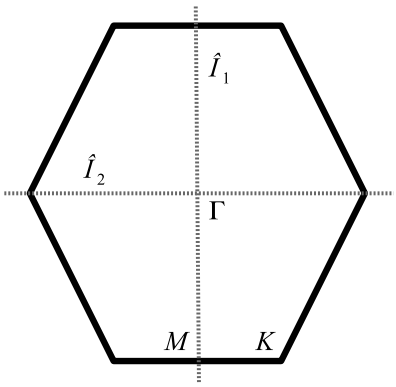

Figure 3.6.: The two inversion symmetry operations of C_{6v} on the Brillouin zone. $\hat{I}_1$ maps sublattices onto themselves, and $\hat{I}_2$ maps them onto one another.

conjugate under inversions around the axis connecting K-points. This can be directly seen from the fact that $\hat{I}_1\, h(\mathbf{k}) \to h(\mathbf{k})$, $\hat{I}_2\, h(\mathbf{k}) \to h^*(\mathbf{k})$. Therefore, anytime we apply a point group symmetry which is related to $\hat{I}_2$, it must be accompanied by complex conjugation. This directly translates to the exploit of symmetries for bosonic propagators and projected Vs.

As mentioned above, the initial projections in the natural Bloch basis yield mainly diagonal contributions in the form factor basis, which are mostly of plain s-wave type for the D channel. In a one-band model, $\hat{B}\left[V^{\Omega_0}\right]_{m,n}$ are strictly diagonal, and for $\hat{B} = \hat{D}$ the only non-zero components are for on-site form factors. In a multiband system, due to the additional momentum structure brought via orbital makeup, the density-density bare interactions in band picture depend on all three transfer momenta, despite its strongest dependence still being on the transfer momentum of the charge channel. Without this additional dependence, i.e. in the absence of transformation elements $\hat{\mathbf{T}}_{\mathbf{k}}$ in the integrals (3.50), it is possible to calculate the initial projections analytically. Since form factors are composed of plane waves, which are orthogonal to the factor $e^{i\mathbf{k}\cdot\mathbf{R}_n}$, only the form factors which correspond to a bond distance $\mathbf{R}_n$ in real space will contribute in the integral. It is thus trivial to see that, for the form factor basis of individual bonds, initial projections are diagonal in the P and C channels and only plain s-wave in the D channel. Using Eq. (3.21) in the transformation (3.24) of a diagonal object, it is also clear that the initial projections are diagonal in the form factor basis of irreducible representations too. For the multiband case, although initial projections are non-zero for all form factor combinations, the main contribution of a density-density interaction acting at a distance $\mathbf{R}_n$ in the P and C channels is still on the form factor components which correspond to that same $\mathbf{R}_n$. Having a bipartite lattice, the projection of intra-orbital interactions is expected to be less accurate than that of intra-orbital ones, since they act at distances $\mathbf{R}_n$ which are not directly reflected on the form factor basis, and their weight is then spread mainly among the two form factor shells which enclose the corresponding $\mathbf{R}_n$. As an illustrative test, let us consider the channel projection of a pure on-site bare interaction, normalized to $U/t = 1$. Being just on-site, the projection integrals take an analogous form in all three channels. The result is shown in Fig. 3.7, where the maximum component of $\hat{P}\,[U]_{m,n}^{b_1\cdots b_4}(\mathbf{l})$ is plotted for different fixed values of m in the form factor basis of irreducible representations. As expected, the weight sits mainly at the on-site form factor component and decays quickly enough for further form factor shells, so that truncating the basis after the first few nearest neighbors should capture short-ranged bare interactions rather accurately.

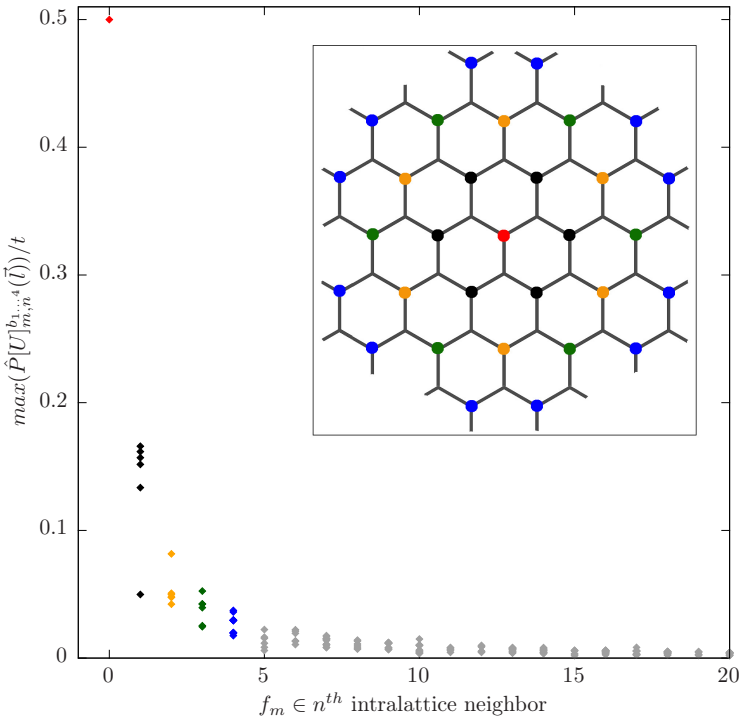

Figure 3.7.: Maximal component out of all choices for $f_n, \mathbf{l}, \{b\}$ of the pairing channel projection of an on-site bare interaction $U = 1\,t$ for each f_m. The different f_ms which belong to the same shell are grouped together under the same color, which corresponds to the coloring shown in the inset figure. The different shells are enumerated along the horizontal axis by increasing intra-lattice neighbor distance in real space.

Apart from the U(1) gauge freedom discussed above, one is also free to do U(1) transformations on the individual eigenvectors that constitute $\hat{\mathbf{T}}_{\mathbf{k}}$, which amount to a redistribution of the phase weight contributed by each sublattice. Denoting the $\mathbf{k}$-dependent transformation elements by

$$h(\mathbf{k})/|h(\mathbf{k})| = \tilde{h}(\mathbf{k}) = e^{i\,\varphi_{\mathbf{k}}} \tag{3.52}$$

the second eigenvector $\left(1, e^{-i\,\varphi_{\mathbf{k}}}\right)$ may as well be chosen as $\left(e^{i\,\frac{\varphi_{\mathbf{k}}}{2}}, e^{-i\,\frac{\varphi_{\mathbf{k}}}{2}}\right)$ or $\left(e^{i\,\varphi_{\mathbf{k}}}, 1\right)$ for example. The latter choice has some numerical advantages, and will therefore be preferred over the initial one, leading to

$$\hat{\mathbf{T}}_{\mathbf{k}} = \frac{1}{\sqrt{2}} \begin{pmatrix} \frac{h(\mathbf{k})}{|h(\mathbf{k})|} & -1 \\ \frac{h(\mathbf{k})}{|h(\mathbf{k})|} & 1 \end{pmatrix} \tag{3.53}$$

The main difference between transformations (3.51) and (3.53) is that, in the integrands (3.50), the second favors combinations of the form $\tilde{h}(\mathbf{k} + \frac{1}{2})\tilde{h}^*(\mathbf{k} - \frac{1}{2})$, which just amount to 1 for $\mathbf{l} = 0$. This eases the numerical computation of initial conditions of the flow, which generally have their more relevant structure at the center of the Brillouin zone. This can be seen for the simple case of on-site form factor components in the projections of a purely on-site bare interaction, i.e. $\tilde{V}^{o_1 \ldots o_4}(\mathbf{R}_n)$ is non-zero for $\mathbf{R}_n = 0$ and all orbital indices being the same. In Eqs. (3.49), using this latter transformation, all the band combinations with two pairs of indices being equal involve

the aforementioned integrals of $\tilde{h}(\mathbf{k}+\frac{\mathbf{l}}{2})\tilde{h}^*(\mathbf{k}-\frac{\mathbf{l}}{2})$. In the former choice of transformation, the combinations $\int d\mathbf{k}\,\tilde{h}(\mathbf{k}+\frac{\mathbf{l}}{2})\int d\mathbf{k}\,\tilde{h}(\mathbf{k}-\frac{\mathbf{l}}{2})$ and $\int d\mathbf{k}\,\tilde{h}(\mathbf{k}+\frac{\mathbf{l}}{2})\int d\mathbf{k}\,\tilde{h}^*(\mathbf{k}-\frac{\mathbf{l}}{2})$ also appear, which are harder to integrate accurately and lead to imbalances among the inter-band components. The difference between these transformation choices obviously impact the computation time too, with the latter variant requiring much less computational effort.

Lastly, we would like to comment on the aforementioned possibilities of either keeping the bare interaction as a separate term in the channel decomposition or assigning it as initial condition in the single channel coupling functions. As it turns out, the latter is more convenient when considering bare interactions whose range greatly exceeds the maximal bond length covered by the form factor basis, as it will be the case for Coulomb interactions. The extended density-density bare interactions considered in this work are most accurately described in the D channel, whereas for the constant on-site bare term it is more natural to split the contribution equally among channels. This can be understood from Eqs. (3.49) if one momentarily ignores the multiorbital case. In a one-band situation, a Coulomb interaction projected onto the D channel is fully contained in the $\mathbf{l}$ dependence of the on-site form-factor components. In contrast, the projection of a Coulomb interaction into the P and C channels takes the form $\sum_{\mathbf{R}_n}\frac{1}{|\mathbf{R}_n|}\int d\mathbf{k}\,f_m^*(\mathbf{k})\,e^{-i\mathbf{k}\cdot\mathbf{R}_n}\int d\mathbf{k}'\,f_n(\mathbf{k}')\,e^{i\mathbf{k}'\cdot\mathbf{R}_n}$, which as already explained, yields non-zero contributions for all diagonal terms in the form-factor indices, with no dependence in $\mathbf{l}$. These values correspond to the interaction strength at the distance where the form-factors are defined in real space. Thus, a given interaction would need as many form-factors as lattice positions covered by its range, in order to be completely captured in each and every channel. This is not feasible for long-ranged interactions, and it suffices to have them properly captured in one channel, and truncated in the remaining two. We normally include form-factors covering at least till the 10^{th} nearest-neighbor, so that channels other than D still get their fair share of the Coulomb interaction, though truncated. In the two-band situation considered in this work, the discussion above holds, although non-diagonal form-factor components take finite but small initial values, as already explained.

Going back to the original point, the main problem that arises when keeping V^{Ω_0} separate in the decomposition is that V^{P} and V^{C} often display spurious behavior. In this decomposition, D collects big counter-terms to V^{Ω_0} when the effective charge interaction gets screened. In turn, the feedback from D into the other two channels should also counter the respective projections of V^{Ω_0}, so that all three projected Vs describe approximately the same screened interaction. However, due to inaccuracies in the inter-channel projections, mainly due to the form-factor basis truncation, some V^{P} and V^{C} components remain unbalanced, vertex symmetries are not satisfied, and the flow usually ends up signaling unphysical instabilities when interactions get enhanced at lower scales, as shown in Fig. 3.8. Instead of separating bare couplings and their renormalized corrections, and having to rely on their accurate counterbalancing in all channels, keeping them together results in more numerically stable flows, as shown in Fig. 3.9. From the two top panels in Figs. 3.8-3.9, one can see that the maximal initial components for the different form factors within each shell have closer values in the second variant. Intuitively, one would expect the latter to be less accurate since these initial values for V^{C} come from the feedback of a bare interaction which is fully contained in the D channel, and they are thus also affected by the limits put by the form factor truncation on the inter-channel feedback. However, the direct momentum space integration done in $\hat{C}\left[V^{\Omega_0}\right]_{m,n}$ for the first variant also has a questionable accuracy, since the integrands are not well behaved. In addition to the discontinuities brought by the transformation elements in the natural basis, there are further discontinuities which arise when projecting inter-orbital interaction terms in

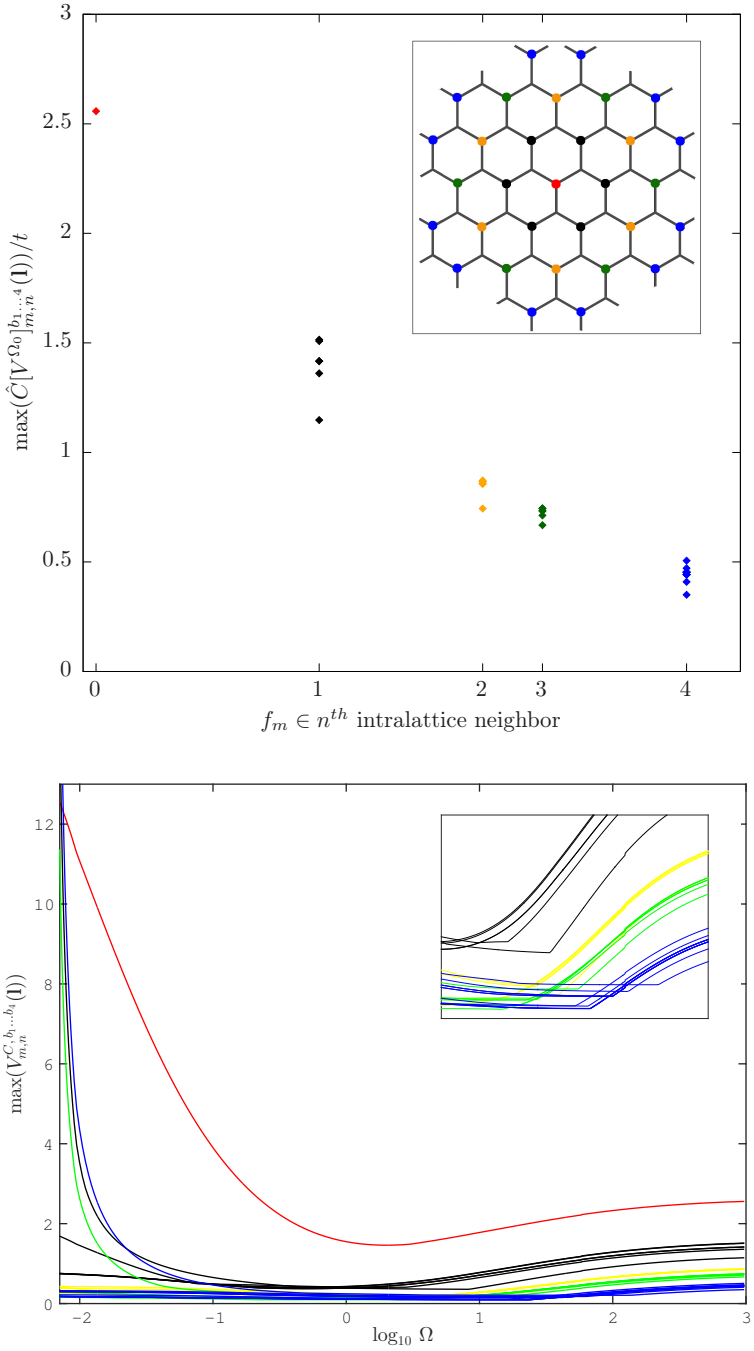

Figure 3.8.: *Top*: Maximal component out of all choices for $f_n, \mathbf{l}, \{b\}$ of the spin channel projection of a Coulomb bare interaction for each f_m. The different f_ms which belong to the same shell are grouped together under the same color, which corresponds to the coloring shown in the inset figure. The horizontal axis denotes the shell number, with their location on the axis being scaled according to the corresponding intra-lattice neighbor distance in real space, for a better appreciation of their Coulombic decay with distance. As a reference, the coupling strengths at the first few bond positions are $U = 3.5\,t$, $V_1 = 2\,t$, $V_2 = 1.5\,t$.
Bottom: Scale evolution of maximal V^{C} components for each form factor, starting at $\Omega = 10^3\,t$ from the initial values plotted in the top panel. The inset shows a zoom of the region around $\Omega = 10\,t$, where their suppression due to charge screening inaccurately saturates.

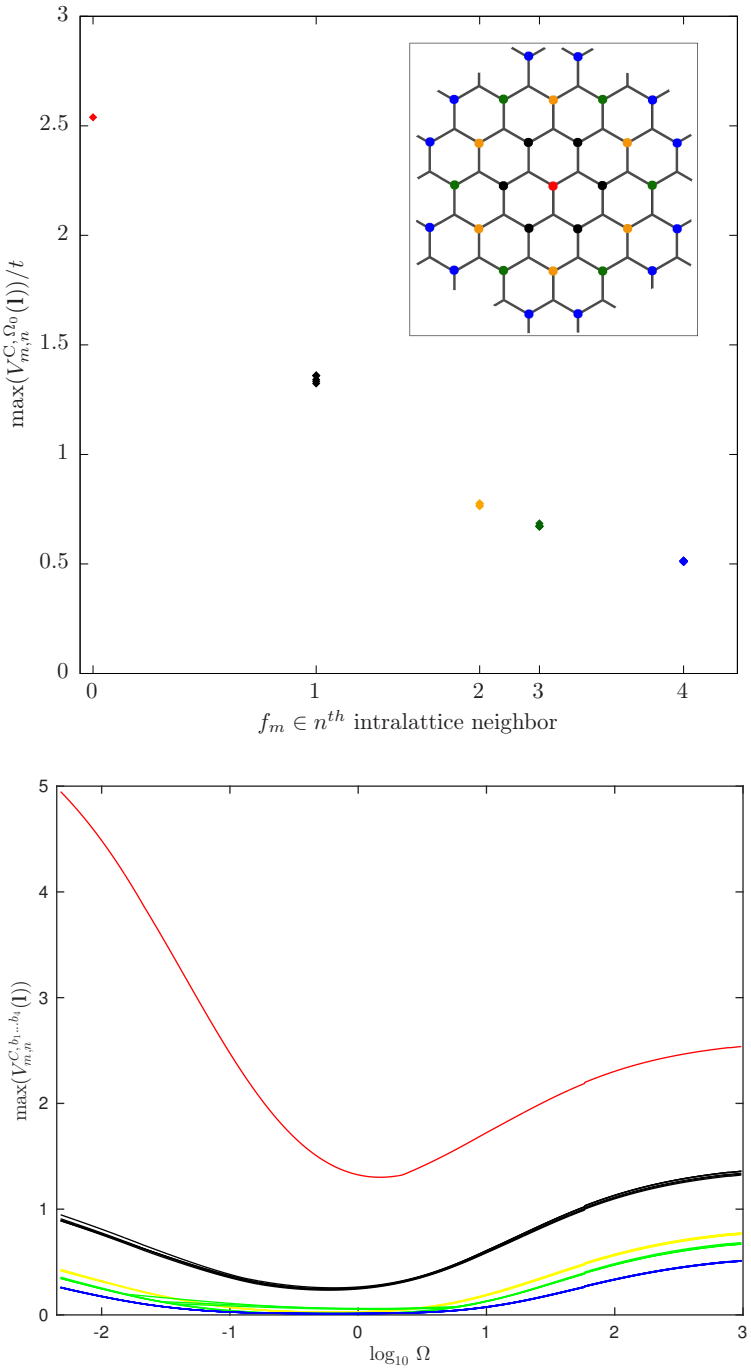

Figure 3.9.: *Top*: Maximal component out of all choices for $f_n, \mathbf{l}, \{b\}$ of the feedback into the spin channel from a D channel projection of a Coulomb bare interaction for each f_m. The different f_ms which belong to the same shell are grouped together, under the same color, which corresponds to the coloring shown in the inset figure. The horizontal axis denotes the shell number, with their location on the axis being scaled according to the corresponding intra-lattice neighbor distance in real space, for a better appreciation of their Coulombic decay with distance. As a reference, the coupling strengths at the first few bond positions are $U = 3.5\,t$, $V_1 = 2\,t$, $V_2 = 1.5\,t$.
Bottom: Scale evolution of maximal V^{C} components for each form factor, starting at $\Omega = 10^3\,t$ from the initial values plotted in the top panel.

the P and C channels, since they involve $\mathbf{R}_n$s which are not Bravais lattice vectors and the complex phases $e^{i\mathbf{k}\cdot\mathbf{R}_n}$ must also be back-folded onto the first Brillouin zone. The second variant avoids computing such challenging integrals, since extended interactions are all put into the D channel where the complex exponential containing $\mathbf{R}_n$ vectors lies outside the integrals. The price to pay is some loss of unbiasedness, since with finite precision and a truncated form-factor basis, different assignments of the bare interaction onto the channels may produce different results. In particular, the Hubbard on-site term U can be equivalently formulated as either density-density, spin-spin, or pairing interaction. One then introduces a slight bias towards magnetism when initializing U fully as spin-spin interaction, for instance. Although splitting U equally among the three channels is the most neutral choice, other possibilities can be considered for consistency checks. The two bottom panels in Figs. 3.8-3.9 represent the two extremal cases out of the possible choices, with the first corresponding to both local and extended bare interactions being treated equally in all three channels, and in the second all coupling terms being fully initialized in the D channel. This explains the differing enhancement of the on-site form factor component in the two variants, which represents a tendency towards an antiferromagnetic spin density wave.

As a side note, we clarify that we will not be considering truly long-ranged Coulomb interactions. The challenging aspect of including long-ranged interactions in the model is that a $\frac{1}{|\mathbf{r}|}$ potential in two-dimensions leads to a $\frac{1}{|\mathbf{l}|}$ behavior in momentum space, and thus the coupling diverges for $|\mathbf{l}| \to 0$ in the D channel. In our case, since we will not be taking the continuum limit, we have a discrete real space sum on the lattice which will be truncated after a certain distance, and therefore the coupling in the D channel stays finite albeit sharply peaked at zero momentum. This is also motivated by the fact that we will not always have an analytic expression for bare interactions in real space, but specific values at given bond distances instead, which follow from ab-initio results in the literature. Moreover, it will also be desirable to be able to modify individual coupling strengths to check their effects on the resulting instabilities or lack thereof. Keeping the explicit form of the Fourier transform from real space also allows to separate the $\mathbf{k}$ and $\mathbf{k}'$ dependences in the four dimensional integrals involved in the initial projections for the P and C channels. Otherwise, one would have $\frac{1}{|\mathbf{k}-\mathbf{k}'|}$ instead of $e^{-i(\mathbf{k}-\mathbf{k}')\cdot\mathbf{R}_n}$ inside the integrals. This last difficulty is nonetheless avoided by initializing extended interactions in the D channel. However, one would still need to introduce some form of artificial screening into the bare interaction in order to have a finite value for $|\mathbf{l}| \to 0$ in the D channel. A natural choice would be a Yukawa potential with screening parameter λ, i.e. $\frac{e^{-\lambda|\mathbf{r}|}}{|\mathbf{r}|}$, leading to a bound $\frac{1}{\sqrt{\lambda^2+|\mathbf{l}|^2}}$ interaction in momentum space. Results can then be checked for convergence as λ is reduced.

On a more technical level, we would like to comment on the criteria to stop the flow when including long-ranged interactions. As already mentioned, in the usual instability analyses, the flow typically begins with a weakly coupled situation and it must be stopped as soon as coupling function components grow beyond the order of magnitude of the single-particle bandwidth. This only applies till inclusions of very few nearest-neighbor interaction terms in the bare coupling. With a high enough number of neighbors included, the bare coupling function for zero momentum transfer in the charge channel takes values which are well over the order of magnitude of the single-particle bandwidth. The alternative is to impose the stopping condition on the difference between renormalized and bare coupling. That way, even though the flow starts with a projected bare coupling in the charge channel exhibiting a strong peak, attention is paid to whether new sharp structures are generated during the flow. In systems with a finite density of states at the Fermi level, the Coulomb peak

at the Brillouin zone center will flatten as charge interactions get screened during the RG flow, posing no real trouble to the identification of an instability signal. In the honeycomb lattice at half-filling, the screening behavior is more complicated, as discussed in Sec. 5.4.1. To distinguish the Coulomb peak from a charge ordering instability, one can perform a minimal transformation to orbital picture as mentioned at the end of Sec. 3.3.1 in case that the peak sharpens during the flow. If no orbital combinations have become attractive, it means that the system is still in a stable metallic or semimetallic state.

4. Application: The extended honeycomb Hubbard model

In this chapter we investigate the quantum many-body instabilities for electrons on the honeycomb lattice at half-filling with extended interactions going up to the second-nearest neighbor, motivated by a description of graphene and related materials. We employ the recently developed TUfRG scheme which allows for highly resolved calculations of wavevector dependences in the low-energy effective interactions. The high momentum resolution is necessary in order to shed light on the possibility of a topological Mott insulator being the favored tendency for dominating second nearest neighbor interactions. We encounter the expected anti-ferromagnetic spin density wave for a dominant on-site repulsion between electrons, and charge order with different modulations for dominant pure n-th nearest neighbor repulsive interactions. Novel instabilities towards incommensurate charge density waves take place when non-local density interactions among several bond distances are included simultaneously. The topologically insulating phase is not realized in our results with high momentum resolution. We also include the effect of a second-nearest neighbor hopping t' in the dispersion relation, and study its impact on the critical scales and critical coupling strength for ordering. The high momentum resolution allows to properly describe the deformation of the band structure brought by t'.

Parts of this chapter have already been published in Refs. [123, 124]

Contents

4.1. Introduction

Since the experimental realization of graphene [103], its unique properties have taken the spotlight due to a wide range of promising applications. It also constitutes a theoretical playground for unusual many-body phenomena [15, 34]. We analyze the possible groundstates of extended Hubbard models on the two-dimensional honeycomb lattice at charge neutrality, focusing on implications for single-layer graphene. Considerable effort has been made through a diversity of methods to address this matter [16–18, 39, 48–52, 55, 95, 135, 136, 138, 140, 144, 145].

In this work, we employ the newly developed *Truncated Unity functional Renormalization Group* scheme (TUfRG) [87], building on prior channel-decomposed fRG [61] and SMfRG [151] schemes. The cornerstone of fRG methods for interacting fermions is their unbiasedness in comparison with mean-field treatments or single-channel calculations like the *random phase approximation*. The fRG treats all ordering tendencies on equal footing, and directly provides a description of the effective low-energy degrees of freedom without the need for prior assumptions about the dominating low-energy correlations. Previous results within the widely used *Fermi surface patching* fRG scheme [45, 53, 162] were computationally limited in their resolution of wavevector dependences of the arising effective interactions. The TUfRG scheme has enabled us to increase the wavevector resolution in a highly scalable [87, 88] and numerically efficient way. The main motivation behind a finer momentum resolution of effective interactions in graphene is twofold. On the one hand, there is evidence about the influence of wavevector resolution on qualitative predictions of fRG results [78, 79, 129, 151, 152], particularly for the realization of exotic topological groundstates in the honeycomb lattice [112, 129]. A higher momentum-resolved calculation could shed light on the inconclusive fate of such topologically non-trivial phases. On the other hand, a finite second-nearest neighbor hopping t' together with an appropriate shift of the chemical potential does not affect the Fermi surface, but alters the band structure. Continuum low energy models and Fermi surface patching schemes cannot properly capture the dependence of effective interactions across the whole Brillouin Zone, and are thus limited in reproducing the effect of band deformations on the interplay among ordering tendencies. Controlled methods like Quantum Monte-Carlo require $t' = 0$ to avoid sign problems.

4.2. Model

The relevant physics in our system of interest can be captured by extended repulsive Hubbard models for interacting spin-1/2 fermions in a honeycomb lattice. The non-interacting part is described by a tight-binding Hamiltonian H_0 with nearest neighbor hoppings of amplitude t, second-nearest neighbor hoppings of amplitude t', and chemical potential μ

$$\begin{aligned} H_0 = &- t \sum_{\langle i,j\rangle,\sigma} \left(c^\dagger_{i,A,\sigma} c_{j,B,\sigma} + \text{H.c.} \right) - t' \sum_{\langle\langle i,j\rangle\rangle,\sigma} \left(c^\dagger_{i,A,\sigma} c_{j,A,\sigma} + c^\dagger_{i,B,\sigma} c_{j,B,\sigma} + \text{H.c.} \right) \\ &- \mu \sum_{i,\sigma} \left(c^\dagger_{i,A,\sigma} c_{i,A,\sigma} + c^\dagger_{i,B,\sigma} c_{i,B,\sigma} \right) , \end{aligned} \tag{4.1}$$

where fermionic operators $c^{(\dagger)}_{i,\sigma,o}$ annihilate (create) an electron at lattice site i and orbital $o \in \{A, B\}$ with spin $\sigma \in \{\uparrow, \downarrow\}$. By orbital degrees of freedom we are referring to sublattice indices, not to be confused with the different orbitals within

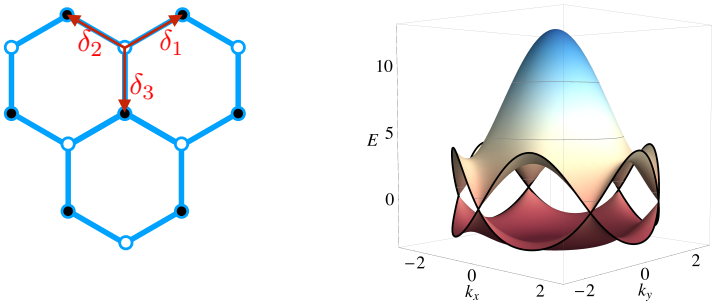

Figure 4.1.: *Left*: Real space lattice structure.
Right: Band energy dispersion for the tight-binding parameters $t = 2.7\,\mathrm{eV}$ and $t' = 0.2\,t$ with adjusted chemical potential $\mu = 3t'$. Energy units are given in eV.

a single atom. The hopping amplitude $t \approx 2.7\,\mathrm{eV}$ sets the energy unit relative to which the interaction strengths and energy scales will be expressed, and the second-nearest neighbor hopping lies in the range $0.02t \lesssim t' \lesssim 0.2t$, as estimated by *ab-initio* calculations [113]. Angled brackets $\langle i, j\rangle$ denote lattice position pairs which differ by a nearest neighbor vector $\boldsymbol{\delta}$ of the honeycomb lattice, depicted in Fig. 4.1. The inter-atomic distance between nearest neighbors is normalized to unity, i.e. $|\boldsymbol{\delta}| = 1$.

This kinetic part can be diagonalized in momentum space to reveal two energy bands featuring two inequivalent Dirac cones at the $\mathbf{K}, \mathbf{K}'$ points in the Brillouin zone corners, as shown in Fig. 4.1. The dispersion relation is given by $\epsilon^{\pm}(\mathbf{k}) = \pm t\sqrt{3 + d(\mathbf{k})} - t'd(\mathbf{k}) - \mu$ with $d(\mathbf{k}) = 2\cos\left(\sqrt{3}k_y\right) + 4\cos\left(\frac{\sqrt{3}}{2}k_y\right)\cos\left(\frac{3}{2}k_x\right)$. At half-filling and $t' = 0$, the single-particle density of states vanishes at the Fermi level due to the presence of linear band crossing points in the low-energy dispersion. For a finite t', the Dirac points remain at the Fermi level if one sets $\mu = 3t'$. The vanishing density of states translates to a semimetallic behavior which is stable against spontaneous symmetry breaking tendencies induced by interactions, at least up to some finite critical interaction strengths. It also implies that interaction processes away from the Fermi level play a more relevant role in comparison with cases where the density of states stays finite or even diverges at the Fermi level. Thus a fine Brillouin zone discretization is required, as evidenced in Ref. [129].

The interacting part of the Hamiltonian up to second nearest neighbor reads

$$H_{\mathrm{int}} = U\sum_{i,o} n_{i,\uparrow,o}\, n_{i,\downarrow,o} + V_1 \sum_{\substack{<i,j> \\ \sigma,\sigma'}} n_{i,\sigma,A}\, n_{j,\sigma',B} + V_2 \sum_{\substack{<<i,j>> \\ \sigma,\sigma',o}} n_{i,\sigma,o}\, n_{j,\sigma',o} \tag{4.2}$$

where $n_{i,\sigma,o} = c^{\dagger}_{i,\sigma,o}\, c_{i,\sigma,o}$ are local density operators, and $<< i, j >>$ represents second nearest neighbor pairs.

Since the RG flow will be calculated in the band picture, where the kinetic part is diagonal, H_{int} also has to be transformed from orbital to band degrees of freedom. That unitary transformation produces some extra momentum structure for the bare interactions, the so-called *orbital makeup*, which also has to be properly sampled in momentum space, as discussed in Sec. 3.3.4. The results shown in Sec. 4.4.1 have been produced using the transformation of Eq. (3.51), and those of Sec. 4.4.2 using the transformation of Eq. (3.53).

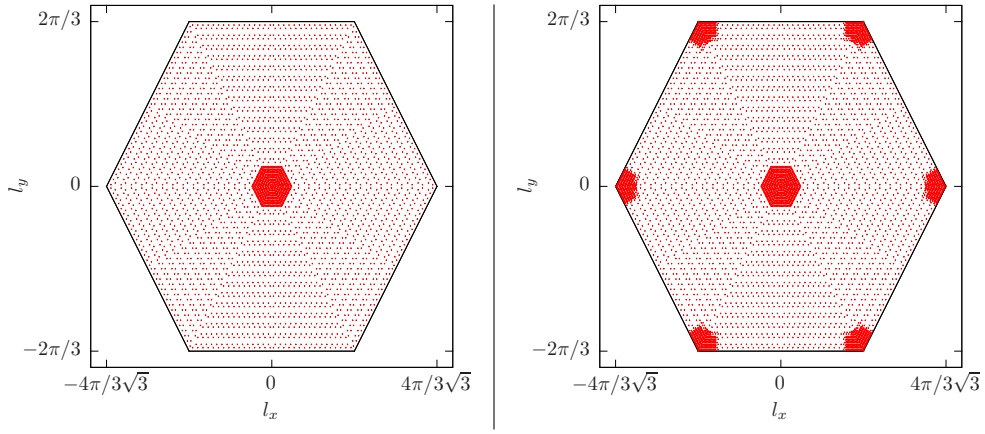

Figure 4.2.: Example discretization for the dependence on transfer momenta $\mathbf{l}$, denser where the ordering vectors are expected.
Left: Mesh of $N_k = 3217$ points for momentum transfers in the particle-particle channel.
Right: Mesh of $N_k = 3661$ points for momentum transfers in particle-hole channels, specifically the one used for a pure V_2 bare interaction. For pure onsite and pure V_1 interactions, the mesh used for momentum transfers in particle-hole channels is the same as that used in the particle-particle channel.

4.3. Method and implementation

We employ a functional Renormalization Group method within the one-loop, one-particle-irreducible (1PI) formalism for fermionic systems introduced in Ch. 2 to perform a weak-coupling instability analysis as explained in Sec. 2.6. The choice of regulator follows the so-called Ω-scheme [61], i.e. infrared divergences are regularized by a soft frequency cutoff introduced in Sec. 2.4. External frequency dependences and self-energies are ignored. For the implementation of the fRG we use the Truncated Unity scheme presented in Ch. 3, which leads to the flow equations in Eqs. (3.18). Briefly put, the scheme splits the two-particle coupling function into a bare part and three channels P, C, D which absorb the renormalization corrections to the bare interaction. These channels are defined so that each of them carries a single dependence $\mathbf{l}$ on one of the possible singular momentum dependences of the coupling function. The remaining weaker dependences in each channel are expanded onto a form factor basis of lattice harmonics (see Sec. 3.3.1 and App. D). The different channels start the flow taking zero values (see Sec. 3.3.4), and may diverge in the case of an instability towards an ordered phase. The channels P, C, D correspond to pairing, magnetic, and charge correlations, respectively. The nature of an ordering tendency is read from the channel where it occurs, with the momentum $\mathbf{l}$ indicating the ordering vector and the form factor indices reflecting the symmetry character of the order parameter to be induced at the instability.

The TUfRG flow equations are solved numerically by a discretization of wavevector dependences in the Brillouin zone into N_k regions, reducing the integro-differential flow equation to a coupled system of $N_b^4 \times N_{ff}^2 \times N_k$ non-linear ordinary differential equations per channel, where N_b is the number of bands and N_{ff} is the number of form factor functions. The ODE system is then solved using a fifth order Adams-Bashforth method. The transfer momenta are discretized into meshes of typically over 3200 points for the particle-particle channel and over 3600 points for particle-

hole channels, as shown in Fig. 4.2. The form factor basis is normally truncated after the second shell of nearest intra-lattice neighbors (fifth nearest real neighbor). In convergence tests we have included form factors up to the fourth shell, and meshes of up to 5000 points for momentum transfers. This meshes are fixed during the flow, making sure that the minimum density of points is high enough to detect instabilities of any ordering vector, and later repeating the calculation with a refined discretization around the relevant regions of the Brillouin zone. However, the momentum integration of the one-loop integrals is done adaptively using denser discretizations of at least a few million points, ensuring that the relative error of these integrals falls below 1%.

4.4. Results

4.4.1. Instabilities in the extended honeycomb Hubbard model at half-filling

Here we present the results of weak-coupling instability analyses for the honeycomb lattice at half-filling and zero temperature. We consider the kinetic Hamiltonian (4.1) with $t' = \mu = 0$, and the bare interactions contained in (4.2). The different tendencies towards symmetry broken ground states are characterized and a tentative phase diagram is obtained. We also provide estimates for the critical scales at which such transitions may occur. Possible deviations due to the approximations involved in our scheme are also discussed.

Emerging ordering tendencies

• *Antiferromagnetic spin density wave* (SDW) *instability*

This tendency is driven by an on-site bare interaction exceeding a critical value $U_c \approx 3.5\,t$, as shown in Fig. 4.3. It manifests itself in the flow as a divergence in the magnetic propagator at zero momentum transfer and plain s-wave form factor components, as depicted in Fig. 4.4. The low-energy effective Hamiltonian obtained reads

$$H_{\mathrm{SDW}} = -\frac{1}{\mathcal{N}} \sum_{o,o'} V_{o,o'} \epsilon_o \epsilon_{o'} \mathbf{S}^o \cdot \mathbf{S}^{o'} \tag{4.3}$$

with $\mathbf{S}^o = \frac{1}{2} \sum_{\mathbf{k},\sigma,\sigma'} \boldsymbol{\sigma}_{\sigma,\sigma'} c^\dagger_{\mathbf{k},\sigma,o} c_{\mathbf{k},\sigma',o}$, $V_{o,o'} > 0$ and $\epsilon_o = +1$ for $o \in \{\mathrm{A}\}$, $\epsilon_o = -1$ for $o \in \{\mathrm{B}\}$. $\boldsymbol{\sigma}$ is to be understood as a vector of the three Pauli matrices. The interaction becomes infinitely ranged, and is attractive for intra-sublattice scatterings and repulsive for inter-sublattice scatterings. The system adopts anti-ferromagnetic order as opposite net spin moments are induced on the different sublattices. The spin quantization axis is not fixed. This transition opens a gap in the electronic spectrum.

As a consequence of numerics, the precise choice for the unitary transformation from orbital to band degrees of freedom affects the resulting value for the critical coupling strength. The value shown above is fortuitously near the exact numerical results [136] (of about $3.8\,t$) although fRG calculations are expected to underestimate critical coupling strengths by a wider margin, due to the neglect of bosonic collective fluctuations. The results shown in Fig. 4.3 are obtained using the transformation from orbital to bands of Eq. (3.51). With a different choice of orbital makeup, namely that of Eq. (3.53), a value of $U_c \approx 2.7\,t$ is obtained, in much better agreement with the most recent and finely discretized Fermi-surface patching results available [149].

This matter has only a quantitative effect on results and does not play a role in the qualitative discussion that follows.

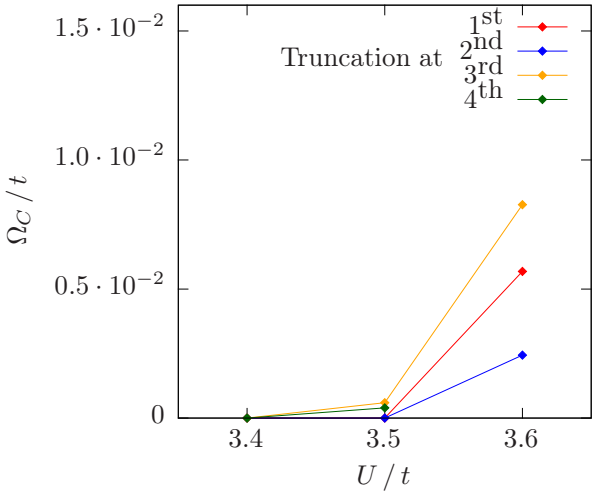

Figure 4.3.: Critical coupling strength for a pure on-site interaction with different truncations of the form factor basis. The reduction in U_c for truncations including further neighbors can be understood as an effect of contributions coming from higher lattice harmonics.

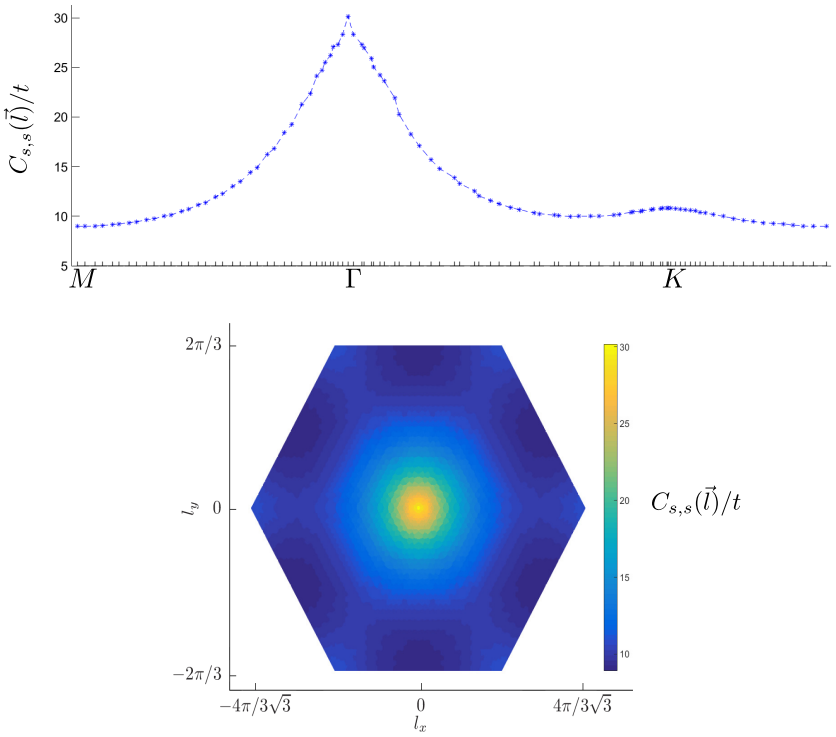

Figure 4.4.: Two dimensional plot (top) and color surface plot (bottom) for the momentum structure of the magnetic propagator signaling a SDW instability. The shown plots correspond to orbital index combinations with $o_1 = o_2 = o_3 = o_4$. For $o_1 = o_3 \neq o_2 = o_4$, the sign structure is reversed as explained in the text.

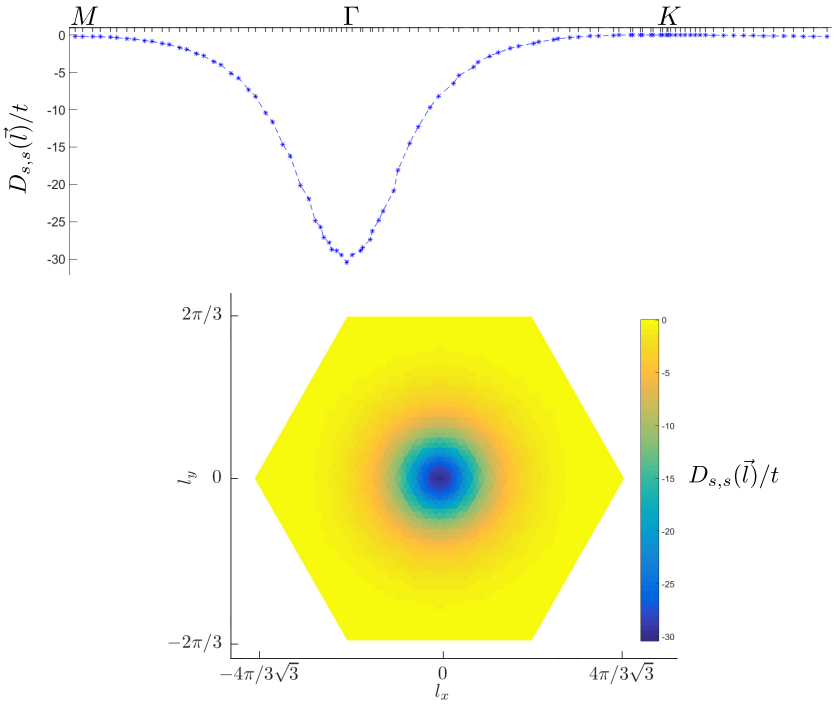

Figure 4.5.: Two dimensional plot (top) and color surface plot (bottom) for the momentum structure of the charge propagator signaling a CDW instability. The shown plots correspond to orbital index combinations with $o_1 = o_2 = o_3 = o_4$. For $o_1 = o_3 \neq o_2 = o_4$, the sign structure is reversed as explained in the text.

• *Charge density wave* (CDW,CDW$_3$,iCDWs) *instabilities*

We find several types of charge order emerging in the honeycomb lattice model. A nearest neighbor bare interaction over a critical value drives a conventional charge density wave (CDW), signaled by diverging couplings in the charge channel with zero momentum transfer and plain s-wave form factor components, as shown in Fig. 4.5. The low-energy effective Hamiltonian is

$$H_{\mathrm{CDW}} = -\frac{1}{\mathcal{N}} \sum_{o,o'} V_{o,o'} \epsilon_o \epsilon_{o'} N^o N^{o'} \tag{4.4}$$

with $N^o = \sum_{\mathbf{k},\sigma} c^\dagger_{\mathbf{k},\sigma,o} c_{\mathbf{k},\sigma,o}$. The orbital sign structure is the same as in the previous instability, which here translates to an infinitely ranged attraction for sites on the same sublattice and repulsion between different sublattice sites. Consequently, the system develops a higher charge occupancy in one of the sublattices. In this phase the energy spectrum becomes gapped as well.

Another charge ordering is found with an enlarged unit cell, named as three-sublattice charge density wave (CDW$_3$) due to the splitting of each sublattice intro three with redistributed charge densities (see Fig. 3 in Ref. [126] or Fig. 4 in Ref. [20]). It is driven by a supercritical second nearest neighbor bare interaction V_2, and shows up as a divergence in the charge channel with momentum transfer $\mathbf{Q} = \mathbf{K} - \mathbf{K}'$ and plain s-wave form factor components, as depicted in Fig. 4.6. The low-energy effective

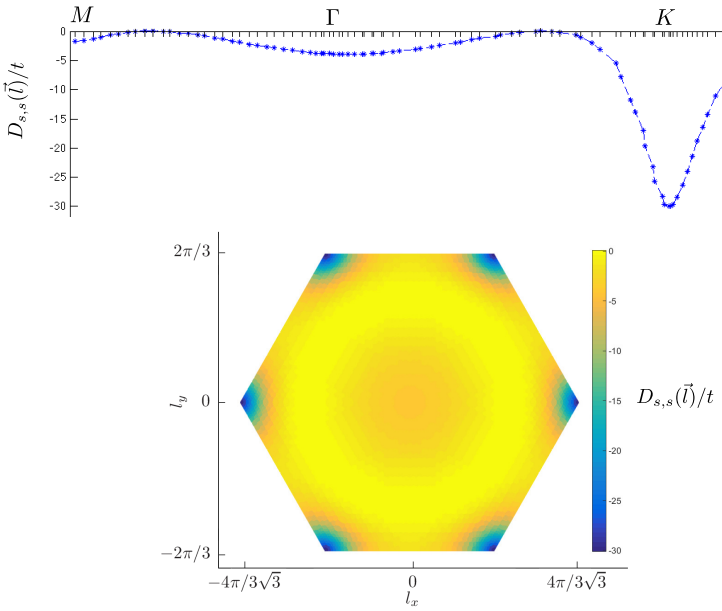

Figure 4.6.: Two dimensional plot (top) and color surface plot (bottom) for the momentum structure of the charge propagator signaling a CDW_3 instability. The shown plots correspond to orbital index combinations with $o_1 = o_2 = o_3 = o_4$. For $o_1 = o_3 \neq o_2 = o_4$, the sign structure is reversed as explained in the text.

Hamiltonian becomes

$$H_{\mathrm{CDW}_3} = -\frac{1}{\mathcal{N}} \sum_{o,o'} V_{o,o'} \epsilon_o \epsilon_{o'} (N^o_{\mathbf{Q}} N^{o'}_{-\mathbf{Q}} + N^o_{-\mathbf{Q}} N^{o'}_{\mathbf{Q}}) \tag{4.5}$$

with $N^o_{\mathbf{Q}} = \sum_{\mathbf{k},\sigma} c^\dagger_{\mathbf{k}+\mathbf{Q},\sigma,o} c_{\mathbf{k},\sigma,o}$ and the same orbital sign structure once again. In this case there is a modulated charge occupancy of the form $\sim \cos(\mathbf{Q} \cdot \mathbf{R} + \alpha)$ for lattice site $\mathbf{R}$, and depending on a phase factor α which controls the relative charge distribution between the three emergent sublattices. A more detailed description of the mean-field order parameter and energy spectrum of this phase can be found in Ref. [126, 127].

Finally, when both V_1 and V_2 are supercritical we find incommensurate charge density waves (iCDWs). The system exhibits geometrical frustration since the charge ordering patterns minimizing either first or second nearest neighbor repulsions cannot be realized simultaneously. The ordering vector depends on the ratio V_1/V_2, wandering gradually between the two commensurate orderings discussed above as the ratio is modified, as displayed in Fig. 4.10. The effective Hamiltonian takes the same form as H_{CDW_3} but with an ordering vector different from $\mathbf{Q}$. Such incommensurate charge orderings had not yet been observed in previous fRG studies on the honeycomb lattice due to the limited momentum resolution. In the usual Fermi surface patching schemes, which discretize momentum dependences just around a small ring centered on the Dirac points, only momentum transfers in a vicinity of either a zero or a $\mathbf{Q} = \mathbf{K} - \mathbf{K}'$ ordering vector are considered. Increasing the radius of such rings widens the allowed transfer momenta at the expense of resolution around the aforementioned ordering vectors. Since even the multi-patch approaches of Ref. [129, 149] only detect commensurate cases, it seems a rather dense discretization is necessary to capture the competition between them that leads to the frustration observed here.

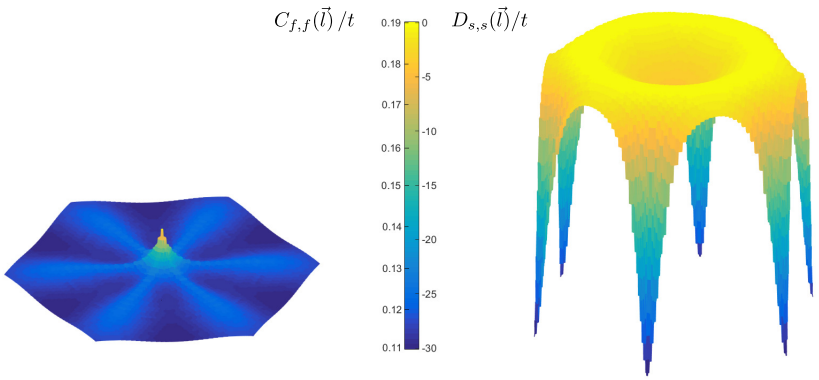

Figure 4.7.: Color surface plots for the momentum structure of the dominating propagators in the magnetic (left) and charge (right) channels. Note the difference in scale for the two plots, with the overall leading tendency being towards a CDW_3 instability.

• *Quantum Spin Hall* (QSH) *instability*

A more exotic tendency has caught a lot of interest in recent years. The possibility of a topological Mott insulator [112], an interaction-induced quantum spin hall state, being realized in the honeycomb lattice is currently a source of ongoing debate. In previous results using less refined fRG methods the QSH was triggered by a high enough second neighbor repulsion term. The characteristic correlations for this phase take place in the spin channel for zero wavevector transfer, with the distinctive feature of having an f-wave symmetry. It results in the effective Hamiltonian of the form

$$H_{\mathrm{QSH}} = -\frac{1}{\mathcal{N}} \sum_{o,o'} V_{o,o'} \epsilon_o \epsilon_{o'} \mathbf{S}_f^o \cdot \mathbf{S}_f^{o'} \tag{4.6}$$

with $\mathbf{S}_f^o = \frac{1}{2} \sum_{\mathbf{k},\sigma,\sigma'} f_{\mathbf{k}} \boldsymbol{\sigma}_{\sigma,\sigma'} c^\dagger_{\mathbf{k},\sigma,o} c_{\mathbf{k},\sigma',o}$ and $f_{\mathbf{k}} = \sin(\sqrt{3}k_x) - 2\sin(\frac{\sqrt{3}k_x}{2})\cos(\frac{3k_y}{2})$. The orbital sign structure is the same as before, but interactions have now an additional f-wave modulation that alternates sign between the K and K' points. In a mean-field decoupling of H_{QSH} an imaginary Kane-Mele order parameter is induced, indicating the formation of an ordered pattern of spin currents with opposite chiralities for the two spin projections. Note that it is called a topological Mott insulator since the state is driven purely by electron-electron interactions, without the need for a prior magnetic flux arrangement as in the original Haldane model [46] or the presence of an explicit spin-orbit coupling term as in the Kane-Mele model [7, 69].

In our results, the tendency towards a QSH state is not found to be the dominant instability for any choice of bare interaction parameters. In previous fRG calculations with a pure second neighbor bare coupling, once the value of V_2 was chosen to be high enough, the QSH eventually dominated [112]. In contrast, we only observe the CDW_3, even up to very high values of V_2 where the weak-coupling condition is not fulfilled anymore. In any case, if the ratio U/V_2 is small enough, the leading correlations in the spin channel are indeed those responsible for the QSH state. However, their enhancement remains rather modest in comparison with the leading correlations in the charge channel, which are two orders of magnitude bigger at the stopping scale, as shown in Fig. 4.7. This scenario of non-dominance for the QSH versus charge order has already been addressed for the QAH in the spinless case with different methods [14, 20, 65, 99, 129], and more recently for the spinful case using fRG [149]. Exact Diagonalization methods have difficulties achieving large system sizes in the spinful

case, and have thus focused mainly on the spinless version. Quantum Monte-Carlo methods have been so far inconclusive [39] on this matter, since they require extended interactions to have a strict decay with distance [51,144] to avoid sign problems. For example, the study of Ref. [39] was limited to coupling strengths $V_2 \leq U/3$. The prevalence of the QSH instability in previous fRG studies on the honeycomb lattice, including single layer [16, 112] and multilayer systems [122, 126, 127], was likely a numerical artifact caused by the insufficient momentum resolution of the effective interactions. All these works rely on a Fermi surface patching with a small patch radius around the Dirac points, which as shown by Ref. [129] artificially favors the QSH respect to discretizations including a broader region of the Brillouin Zone.

Phase diagrams and critical scales

The phase diagrams obtained are shown in Figs. 4.8-4.9. Apart from the semimetallic phase prevailing in the absence of an instability, the observed tendencies are either towards antiferromagnetic order or towards charge order with different modulations. As discussed in the previous part of this section, the QSH instability is absent from the phase diagram. We do not observe dominant tendencies towards the Kekulé valence-bond-solid either, which has been found in other studies [14,76,99,125,130] including a Fermi surface patching fRG approach that takes into account the effect of phonons [16] and also observes nematic bond dimers. In accordance with previous work on the undoped honeycomb lattice system, we do not find any leading instabilities in the pairing channel.

In comparison with previous fRG phase diagrams, aside from the differing ordering tendencies, the present scheme is apparently more sensitive to competition effects, as evidenced by the stronger critical scale variations across the different phases. Though less pronounced, the suppression of critical scales around the boundaries between different tendencies was already captured in previous schemes. Now, even for all

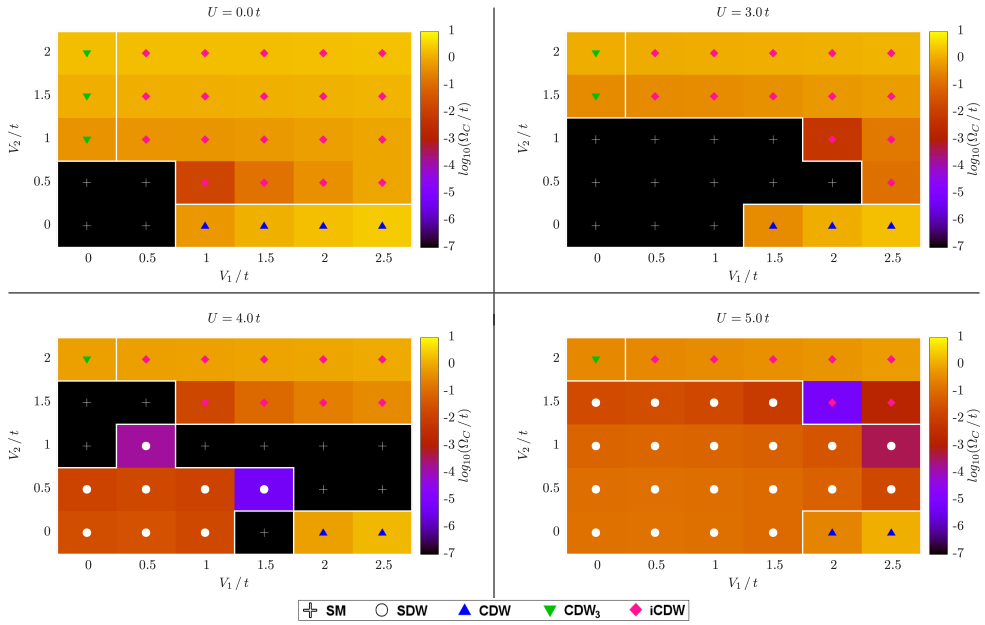

Figure 4.8.: Dominant instabilities and critical scales for different bare interaction parameters.

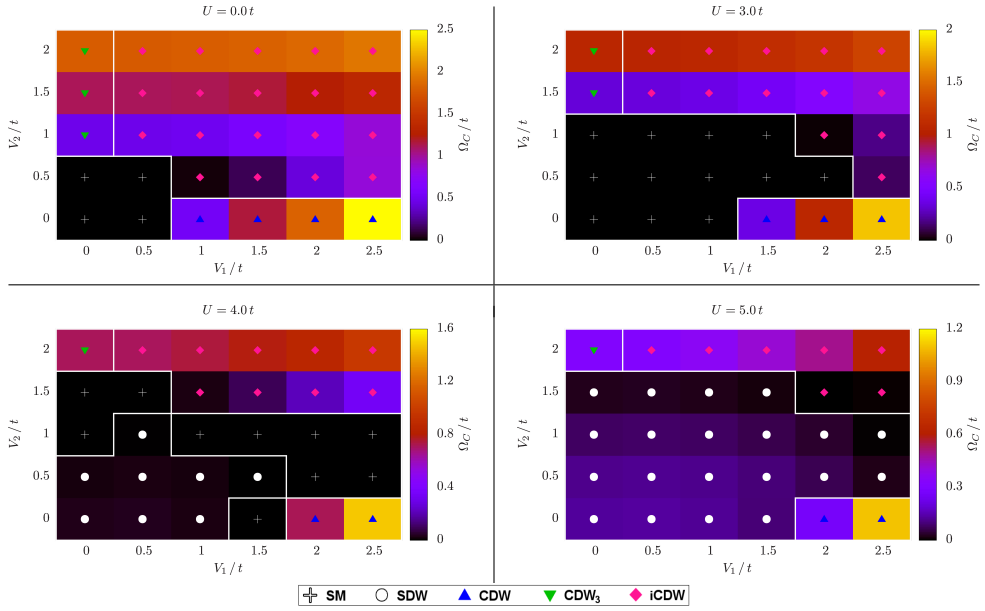

Figure 4.9.: Phase diagrams of Fig. 4.8 with a linear plot of critical scales.

three bare coupling parameters taking values which are higher than their individual critical strength, there are regions where the system stays semimetallic, or where there is at least a very strong suppression of several orders of magnitude for the critical scale. Despite currently available fRG schemes being certainly not exact, the physical plausibility of a semimetallic state being stabilized by competition effects makes these results worth considering, although this interesting proposal has yet to

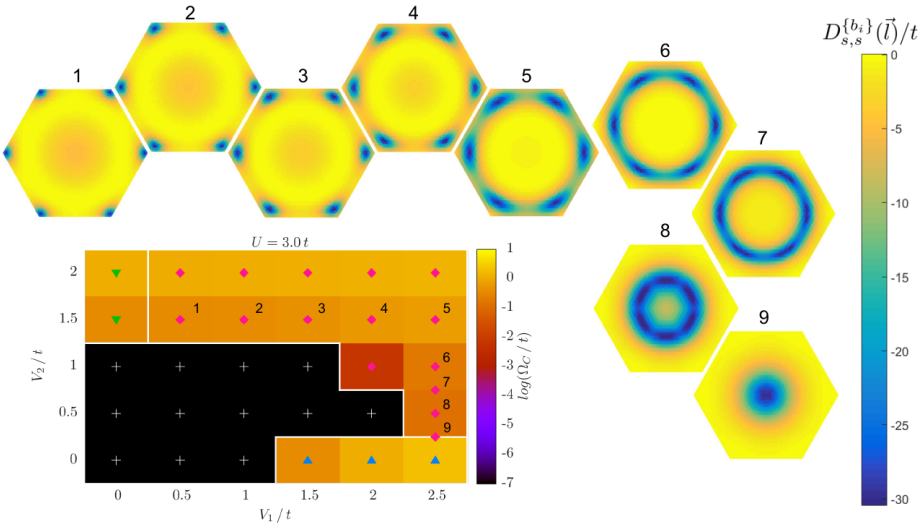

Figure 4.10.: Plots of the $\mathbf{l}$ dependence of $D_{s,s}(\mathbf{l})$ at the stopping scale for different V_1/V_2 ratios. The ordering vectors in plots 1 and 9 are still incommensurate, though very close to K and Γ respectively. Since U is subcritical and there is no significant enhancement of magnetic correlations, the behavior of the more physically meaningful $K_{s,s}(\mathbf{l})$ obtained from Eq. (3.5) is almost indistinguishable from that of the D propagator above.

be contrasted with other methods. In the following chapter, this idea will be pursued further, including additional repulsive interaction terms among neighbors at longer distances than here considered.

The resulting instabilities are robust with respect to the inclusion of further shells of form factors or the use of denser meshes, so long as the locations for ordering vectors in the Brillouin zone are finely discretized. Quantitatively speaking, the truncation of the form factor basis may influence the critical scales in some regions of the phase diagram. As shown in Ref. [87] for the square lattice, the truncation of the form factor basis has an effect on regions where there is a strong competition between channels. For systems with a vanishing density of states at the Fermi level, the truncation also affects regions around the critical coupling strengths (Fig. 4.3). Thus the truncation may affect the critical scales at boundaries between magnetic and charge ordered phases, and at boundaries between the semimetal and ordered phases in general. Including the third shell of form factors for selected points at such boundaries, some experience an increase in critical scale whereas others find it further suppressed. For instance, for $U = 4\,t$, $V_1 = 1.5\,t$, $V_2 = 0.5\,t$ the critical scale comes out an order of magnitude higher, but for $U = 5\,t$, $V_1 = 2.5\,t$, $V_2 = 1.5\,t$ it is an order of magnitude lower than in the 2^{nd} shell truncation.

4.4.2. Antiferromagnetism in the $t - t'$ honeycomb Hubbard model

Starting from a well-tested setup for the pure $t-U$ model without further interactions, we add a second-nearest neighbor hopping amplitude t' in order to better model the full band structure of graphene, cf. Eq. (4.1). In particular, we investigate for the first time the effect of t' on the value for U_c/t, i.e. the critical Hubbard-interaction that induces the ordering transition to the AF-SDW, and on the critical scales for ordering. As the second-nearest neighbor hopping is known only approximately, we sweep through a range of values for t' that are expected to be relevant for graphene, explicitly $|t'| \in [0, 0.2\,t]$. Simultaneously, for $t' \neq 0$, we adjust the chemical potential to $\mu = 3t'$ so that the Fermi level lies at the Dirac point.

For $t' = 0$, employing the TU-fRG approach, we obtain a critical Hubbard interaction of $U_c \approx 2.7\,t$. We note that this value is smaller than the numerical value of $U_{c,\text{QMC}} \approx 3.8\,t$. With the instability already appearing at smaller U_c/t, the TU-fRG seems to overestimate the effect of fermionic fluctuations, as already commented in Sec. 4.4.1. Another effect that tentatively increases the value of U_c/t is the logarithmic renormalization of the Fermi velocity [29]. This effect is not included within our truncation scheme since we do not take into account the flow of the self-energy. Therefore, we note that we do not expect our results to be quantitatively precise. Nevertheless, we can give estimates for parameter trends in situations which are inaccessible to controlled methods like QMC.

We go on to study the impact of t' on the critical scales Ω_c of the Hubbard-model which we interpret as an estimate for the typical gap size of the system, see Fig. 4.11. We observe, that a finite t' does not significantly change the value of the critical onsite interaction. This can be rationalized as close to the critical interaction, the instability will only appear for small scales and therefore is governed by the dispersion close to the Dirac points. This dispersion is not changed by the presence of t' except for the shift in the Fermi level, which we have absorbed by adjusting the chemical potential. On the other hand, a finite t' changes the critical scales above U_c considerably, as can also be appreciated in Fig. 4.11. We therefore predict that a finite second-nearest neighbor hopping t' has a sizable impact on the expected size of the many-body mass gaps and transition temperatures. For example, for $U/t = 2.85$, the critical scale

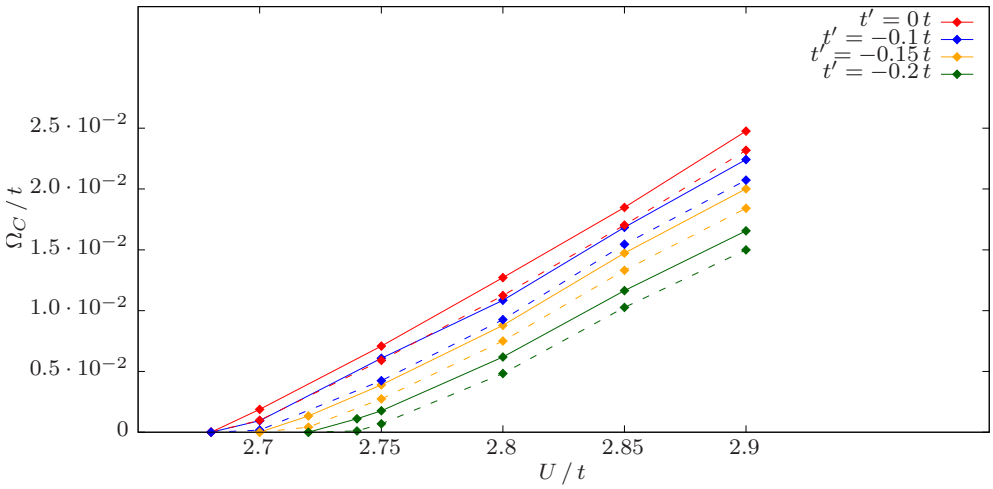

Figure 4.11.: Effect of t' on the critical scale Ω_c for a model with pure onsite interaction and truncation at the second shell of form-factors (solid) and at the third shell of form factors (dashed). Results including the fourth form-factor shell do not deviate from those including only till the third, indicating good convergence.

Ω_c/t is reduced by about 40% upon inclusion of a second-nearest neighbor hopping $t' = -0.2t$, suggesting smaller gaps than the one that would be predicted in a simple tight-binding model with nearest-neighbor hopping only.

This suppression of the critical scale is an effect beyond mean-field or single-channel ladder summations. For comparison, switching off the particle-particle channel, i.e. resorting to an effective single-channel resummation, and setting $U = 2.85\,t$, a second-nearest neighbor hopping $t' = -0.2\,t$ leads to only a 4% critical scale reduction respect to $t' = 0$. The result is the same for all truncations up to the 4^{th} form-factor shell, since without particle-particle channel, there is no significant inter-channel feedback and there is a fast convergence with respect to the number of form-factor shells. That smaller suppression of the critical scale is due to the breaking of particle-hole symmetry. At $t' = 0$, the whole Brillouin zone is perfectly nested with respect to interband scatterings with zero momentum transfer in the magnetic channel. A finite t' respects the approximate particle-hole nesting around the Fermi level, and therefore its influence on the critical scale is mild in terms of the particle-hole channel alone. Note that apart from the energy shift, which is absorbed in the chemical potential, a finite t' only affects the low energy spectrum through quadratic corrections to the linear dispersion, and does not affect the Fermi velocity to linear order. On the other hand, it flattens the lower energy band, leading to higher particle-particle correlations, which are known to inhibit magnetism [68]. We therefore conclude that the strong suppression of about 40% seen in Fig. 4.11 is a consequence of the interplay between different channels.

4.5. Conclusion

In this chapter we have investigated the effect of improved wavevector resolution of effective interactions on fRG predictions for possible groundstate orderings of electrons in the honeycomb lattice with extended bare interactions up to the second nearest neighbor. The effect of a finite second nearest neighbor hopping term on antiferro-

magnetic instabilities was also studied.

Although the commonly used Fermi-surface patching scheme has brought many insights over the years in capturing the competition of ordering tendencies in an unbiased way, limitations on its predictive power have led to some qualitative discrepancies respect to other theoretical methods and experimental measurements. The TUfRG scheme constitutes a further step to already existing improved parametrizations of the fRG flow [24–26, 61, 91, 151, 161], providing an efficient and highly scalable way to refine the Brillouin zone discretization of momentum dependences. There is room for improvement of the scheme, with the most natural extensions being the inclusion of Matsubara frequency dependences and self-energy flows. Nevertheless, the present implementation has already brought some new perspectives on the possible interplay of ordering tendencies in the honeycomb lattice. More specifically, the high wavevector resolution achieved in this work has allowed us to observe a continuous evolution of incommensurate charge orderings for the first time, originating in the frustrated nature of competing interactions in the density channel. This competition also led to a strong suppression of critical scales for parameter combinations such that tendencies are balanced, opening the door for a robust stability of the semimetallic state if additional competing density-density terms are included. Furthermore, our results support the recent findings about the non-dominance of a topological QSH state versus charge order [14, 20, 65, 99, 129, 149]. Using less refined momentum discretizations, the QSH had been found dominant for strong enough second nearest neighbor interactions. Within the present scheme, however, such an instability is strongly suppressed in the whole phase diagram for short-ranged interactions. In addition to the study of different interaction parameter combinations, we also extended the kinetic parameters to include a second nearest neighbor hopping t'. We found a sizable reduction of up to 40% for the critical scales in the antiferromagnetic transition of the honeycomb Hubbard model upon inclusion of a t' chosen within the range of suggested *ab initio* values. We showed that this effect is beyond single-channel resummations and results from the complex interplay between different interaction channels. This finding suggests that a finite t' causes a considerable reduction of expected gap sizes in the honeycomb Hubbard model.

5. Application: The strained honeycomb Hubbard model with long-ranged Coulomb interactions

In this chapter we study the quantum many-body ground states of electrons on the honeycomb lattice with long-ranged density-density interactions as a model for graphene. To this end, we employ the recently developed truncated-unity functional renormalization group (TUfRG) approach which allows for a high resolution of the interaction vertex' wavevector dependence. We connect to previous lattice quantum Monte Carlo (QMC) results which predict a stabilization of the semimetallic phase for realistic ab initio *interaction parameters and confirm that the application of a finite biaxial strain can induce a quantum phase transition towards an ordered ground state. In contrast to lattice QMC simulations, the TUfRG is not limited in the choice of tight-binding and interaction parameters to avoid the occurrence of a sign problem. Therefore, we also investigate a range of parameters relevant to the realistic graphene material which are not accessible by numerically exact methods. Although a plethora of charge density waves arises under medium-range interactions, we find the antiferromagnetic spin-density wave to be the prevailing instability for long-range interactions. We further explore the impact of an extended tight-binding Hamiltonian with second-nearest neighbor hopping and a finite chemical potential for a more accurate description of the band structure of graphene's p_z electrons.*

Parts of this chapter have already been published in Ref. [124]

Contents

5.1. Introduction

The experimental realization of graphene in 2004 [34,103] has inspired many ideas for a wide range of possible technological applications due to its superior physical properties [15,21], such as its excellent electrical conductivity. The semi-metallic behavior of graphene's two-dimensional electron gas is protected by the nature of its low-energy excitations, which come in the form of Dirac fermions featuring a linearly vanishing density of states (DOS) close to the Fermi level. This has fundamental consequences for the possible effects of many-body interactions [81]: For weak electron-electron interactions, the material remains semi-metallic. Instead, it requires intermediate to strong interactions to turn it into a Mott insulator or any other ordered many-body ground state [48, 77, 135]. Experimental observations for suspended graphene confirm the stability of the semi-metallic ground state even for very low temperatures [29, 93] indicating a subleading role of electronic interactions in graphene. On the other hand, specific manipulations of the material such as the application of a uniform and isotropic strain have recently been proposed and theoretically found to facilitate the opening of an interaction-induced band gap [138]. This could pave the way towards an even broader range of possible technological applications as, e.g., a graphene transistor.

The question of whether electronic interactions can induce a metal-insulator transition in an accessible experimental setup can be approached by theoretical methods in two steps:

(1) Identification of a suitable model to study interacting electrons in graphene including a determination of model parameters from *ab initio* methods. (2) Application of appropriate many-body methods to the model to predict the ground state of the system.

As for (1), the paradigmatic model which is used for the description of the p_z electrons in graphene is composed of a tight-binding Hamiltonian, H_0, describing electrons hopping on a honeycomb lattice and an interaction Hamiltonian, H_{int}, which parametrizes the two-body interactions including a short-ranged part and a long-range tail. For the *ab initio* parameters of the tight-binding Hamiltonian, various works agree on amplitudes of $t \approx 2.7\,\text{eV}$ and $0.02t \lesssim t' \lesssim 0.2t$ for the hopping of an electron to its nearest-neighbor and second-nearest neighbor on the honeycomb lattice, respectively [113]. For the determination of the interaction parameters from first principles different methods are available providing different interaction profiles of graphene's p_z electrons [66,133,138,146,156]. Despite the differences in the details, all methods suggest that the interaction parameters are located in the intermediate coupling regime defining a considerable challenge for many-body methods.

Resulting from considerations of the effects of the different interaction parameters many qualitative studies have revealed a rich ground state manifold depending on the magnitude and ratio of the different local and non-local electron-electron interaction parameters [5,14,20,23,33,43,48,50,55,77,105,112,123,129,134,135,140,149]. Possible ground states include an antiferromagnetic spin-density wave state, different commensurate and incommensurate charge density wave states, a Kekulé dimerization pattern and more. More recently, numerically exact methods, i.e. quantum Monte Carlo (QMC) simulations have become available which can explore a range of realistic parameters for the graphene model [12, 134, 144]. These works confirm the experimentally found semi-metallic behavior of the material. It was further suggested that a biaxial strain of about 15% can turn graphene into an antiferromagnetic Mott insulator [138] at least when the Thomas-Fermi method for the determination of the interaction profile [66] is assumed. On the other hand, the *ab initio* interac-

tion profile suggested by the constrained random phase approximation (cRPA) [156] did not indicate a semi-metal-insulator transition up to 18% strain [138]. It may be noted, however, that QMC methods are limited by the choice of band structure and interaction parameters [12, 138], i.e. to avoid the occurrence of a sign problem, the long-range tail of the electronic interaction profile has to decrease fast enough. Therefore, a third option for the interaction parameters from the Pariser-Parr-Pople model [146] could not be investigated in Ref. [138]. Also, band structure parameters other than the nearest-neighbor hopping t have to be neglected within QMC simulations. This introduces a bias to the range of available results when aiming at the description of realistic graphene models. More specifically, the limitation of the interaction profile to a long-range behavior that pronounces the local part of the interaction leads to a preference of the antiferromagnetic ground state. In fact, the antiferromagnetic ground state is the only ordered state that has been accessed by QMC simulations with one exception: In Ref. [12] a model with onsite interaction U and nearest-neighbor interaction V_1 was studied and indications for a competition between spin- and charge-density wave order have been found for specific choices of parameters giving rise to a multicritical point in parameter space, cf. also Refs. [17, 18].

In this chapter, we overcome the limitations in the choice of interaction profiles by employing the TUfRG [87, 123] which allows for a high resolution of the interaction vertex' wavevector dependence, as explained in Ch. 3. In particular, this allows to explore a large set of band structure parameters, e.g., a second-nearest neighbor hopping term and a chemical potential as well as an extended range of realistic interaction parameters. It also addresses the necessity of explicitly dealing with the coupling of energy modes across the whole band structure [123, 129, 149], instead of directly resorting to an effective low energy description as in a continuum Dirac model or only considering the scattering among low energy modes as in usual Fermi surface patching fRG schemes. Aiming at quantitative results, one must include interactions between modes from the whole Brillouin zone and not just from the vicinity of its corners, especially since at the latter the density of states vanishes.

Recent TUfRG calculations for an explorative set of short-ranged interaction parameters already suggest that the semimetallic nature of graphene's groundstate is not due to interaction terms that are too weak to induce an ordered state, but rather because of a complex interplay between different competing instabilities which leads to an effective frustration [123]. Moreover, it has been found that the leading instability is not necessarily an antiferromagnetic spin density wave state, but can also be an incommensurate charge density wave and other charge modulated states [123]. We note that the fRG is not a method which provides numerically exact results, however, numerically exact methods have a much narrower scope. In the situations accessible to exact methods, a systematic comparison with fRG results provides confidence for the method's application to other regimes. This provides important insights on the real material, allowing to go beyond the statements that are possible within a single theoretical method alone.

In this work, we employ the TUfRG to facilitate an unbiased approach to identify the leading instability of electrons on the honeycomb lattice with realistic band structure parameters and a long-range interaction tail provided by *ab initio* approaches. As a particular strength of the TUfRG approach in this context, we emphasize that it does take into account the fermionic fluctuations in an unbiased way. Furthermore, the TUfRG is not bound to a sufficiently fast decay of the (partially screened) Coulomb tail and provides a sufficient wavevector resolution to resolve the long-range tail. In particular, it can explore the effect of arbitrary ratios of short-ranged (non-local) interaction terms which are known to trigger very different types of order. This is a clear advantage to the numerically exact QMC methods which have a sign problem

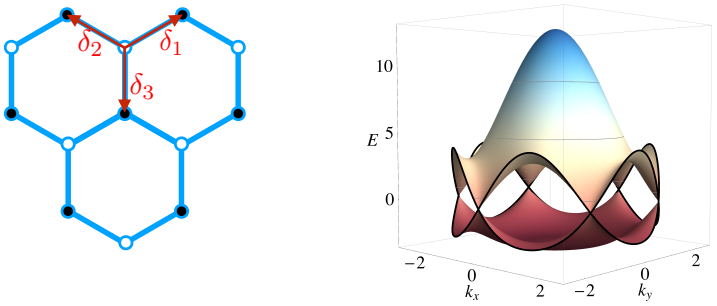

Figure 5.1.: *Left*: Real space lattice structure.
Right: Band energy dispersion for the tight-binding parameters $t = 2.7\,\mathrm{eV}$ and $t' = 0.2\,t$ with adjusted chemical potential $\mu = 3t'$. Energy units are given in eV.

if the Coulomb tail does not decay sufficiently fast and are therefore 'biased' towards antiferromagnetic order. So, while our results will not give quantitative estimates for gaps or transition temperatures, we will be able to resolve the qualitative effects and competing orders that are induced by an extended range of realistic interaction profiles.

A broader scope of the insights obtained in this work is given by the more general set of low-dimensional *sp*-electron systems of adatoms on semiconductor surfaces such as Si(111):X with X=C, Si, Sn, Pb which exhibit both strong local and non-local Coulomb interactions. In these surface systems, e.g., for Si:X, Mott transitions have been observed, cf. Ref. [47].

5.2. Model and parameters

To model the interacting p_z electrons on graphene's half-filled honeycomb lattice, we consider a tight-binding model for spin-1/2 fermions enhanced by density-density interaction terms representing the long-ranged Coulomb interaction. Therefore, the Hamiltonian has a single-particle hopping term H_0 and an interaction term H_{int},

$$H = H_0 + H_{\mathrm{int}}\,, \tag{5.1}$$

to be specified in the following. H_0 is the tight-binding part

$$\begin{aligned} H_0 = &- t \sum_{\langle i,j\rangle,\sigma} \left(c^\dagger_{i,A,\sigma} c_{j,B,\sigma} + \mathrm{H.c.} \right) \\ &- t' \sum_{\langle\langle i,j\rangle\rangle,\sigma} \left(c^\dagger_{i,A,\sigma} c_{j,A,\sigma} + c^\dagger_{i,B,\sigma} c_{j,B,\sigma} + \mathrm{H.c.} \right) \\ &- \mu \sum_{i,\sigma} \left(c^\dagger_{i,A,\sigma} c_{i,A,\sigma} + c^\dagger_{i,B,\sigma} c_{i,B,\sigma} \right)\,, \end{aligned} \tag{5.2}$$

with nearest-neighbor hopping amplitude t, second-nearest neighbor hopping t' and chemical potential μ. The nearest-neighbors are given by the position vectors $\boldsymbol{\delta}_1, \boldsymbol{\delta}_2, \boldsymbol{\delta}_3$ of the hexagonal lattice, depicted in Fig. 5.1, which has a two-atomic basis with sublattice index $o \in \{A, B\}$. We will interchangeably denote o as sublattice or

orbital degrees of freedom, not to be confused with different orbitals within a single atomic site. The Carbon-Carbon distance is normalized to unity, i.e. $|\boldsymbol{\delta}_i| = a = 1$. Moreover, $c^{(\dagger)}_{i,o,\sigma}$ annihilates (creates) an electron at site i in sublattice o with spin $\sigma \in \{\uparrow, \downarrow\}$.

This tight-binding model gives graphene's characteristic valence and conduction bands which touch linearly at the two inequivalent corner points of the Brillouin zone (BZ), i.e. the K, K' or Dirac points as described by the energy dispersion $\epsilon^{\pm}(\mathbf{k}) = \pm t\sqrt{3 + d(\mathbf{k})} - t'd(\mathbf{k}) - \mu$ with $d(\mathbf{k}) = 2\cos\left(\sqrt{3}k_y\right) + 4\cos\left(\frac{\sqrt{3}}{2}k_y\right)\cos\left(\frac{3}{2}k_x\right)$. Close to the Dirac points the energy dispersion can be approximated by $\epsilon^{\pm}(\mathbf{k}) \approx 3t' \pm \frac{3t}{2}|\mathbf{k}|$, i.e. to put the Fermi-level to the Dirac points we have to adjust the chemical potential to $\mu = 3t'$. For the *ab initio* parameters of the tight-binding Hamiltonian, suggested amplitudes are $t \approx 2.7\,\mathrm{eV}$ and $0.02t \lesssim t' \lesssim 0.2t$, cf. Ref [113].

The interaction part H_{int} from the Coulomb interaction of the electrons is parametrized by local and non-local density-density contributions

$$\begin{aligned} H_{\mathrm{int}} = & U \sum_{i,o} n_{i,o,\uparrow} n_{i,o,\downarrow} \\ & + \sum_{\substack{i \neq j,\, o,o' \\ \sigma,\sigma'}} \frac{U^{o,o'}_{i,j}}{2} n_{i,o,\sigma} n_{j,o',\sigma'} \,, \end{aligned} \tag{5.3}$$

where $n_{i,o,\sigma} = c^{\dagger}_{i,o,\sigma} c_{i,o,\sigma}$ represents the electron density operator, and interaction coefficients read

$$U^{o,o'}_{i,j} = U_{i,j} \begin{cases} \delta_{o,o'} & \text{for intra-orbital } (i,j) \text{ pairs} \\ 1 - \delta_{o,o'} & \text{for inter-orbital } (i,j) \text{ pairs} \end{cases} \tag{5.4}$$

Different kinds of ordered states occur when the individual interaction parameters exceed critical values. Sizable onsite interactions $U > 0$ trigger a phase transition towards an antiferromagnetic spin-density wave (SDW) state. Each n^{th} nearest-neighbor repulsion term $U_{i,i+n} = V_n$ supports a different ordering transition towards charge order, with the nearest-neighbor term V_1 triggering the conventional charge-density wave (CDW).

5.2.1. Modification of hopping amplitudes from strain

The hopping amplitudes in the tight-binding Hamiltonian in Eq. (5.2) are subject to modifications upon lattice distortions as a result of the change in wave-function overlap. For the *ab initio* model parameters from the constrained random phase approximation of Ref. [156], t has a linear decay vs. strain η. To model the effect of strain on other choices of *ab initio* model parameters, where direct results are not available, we assume an exponential decay of the hopping amplitudes following the empirical relation [100, 106]

$$t_{ii'} = t_0 e^{-\beta\left(\frac{|\boldsymbol{\delta}_{ii'}|}{a} - 1\right)} \,, \tag{5.5}$$

where a is the unstrained lattice constant which we have set to $a = 1$ and t_0 is the unstrained nearest-neighbor hopping amplitude. The material-dependent factor β is estimated to $\beta = 3.37$ for graphene and $\boldsymbol{\delta}_{ii'}$ is the vector connecting sites i and i'. For

the unstrained second-nearest-neighbor hopping, this formula provides an numerical value of $t' = t_0 \exp(-3.37(\sqrt{3}-1)) \approx 0.085t$ which is located in the estimated range.

A finite and uniform strain η can be included using a strategy suggested in Ref. [138] by the replacement $|\boldsymbol{\delta}_{ii'}| = r \to (1+\eta)r$ with strain parameter η. Then, the strained hopping amplitudes are given by

$$t(r,\eta) = t_0 e^{-3.37\cdot[(1+\eta)r-1]}\,, \tag{5.6}$$

and r has to be evaluated at the equilibrium positions of the neighboring sites, i.e. $r = 1$ for the nearest neighbor and $r = \sqrt{3}$ for the second-nearest neighbor. This gives a strain-dependence of the nearest-neighbor hopping of $t(\eta) = t_0 \exp(-3.37\eta)$ and for the second-nearest neighbor hopping $t'(\eta) = t_0 \exp(-3.37((1+\eta)\sqrt{3}-1))$.

5.2.2. Ab initio interaction parameters

For the determination of the interaction parameters for p_z electrons in graphene from first principles various methods are available. In the context of biaxially strained graphene and its effect on the quantum many-body ground states, three of these methods have been explored in Ref. [138] for the case of graphene: The Thomas-Fermi (TF) method [66], the constrained random phase approximation (cRPA) [156] and the quantum-chemistry-Pariser-Parr-Pople (QC-PPP) method [146]. In this work, we disregard the TF method, which shows the strongest decay in the interaction parameters when going to larger distances. Therefore, this method can be considered to be well-covered by the QMC simulations. Instead, here we concentrate on the cRPA and the QC-PPP methods which have stronger non-local short-ranged interactions. In particular, due to a sign problem, it was not possible to study the interaction profile suggested by the QC-PPP method and we fill this gap here.

Constrained random phase approximation

In the cRPA the effective interaction profile for graphene's p_z electrons is described by the formula

$$V(r) = \frac{\bar{V}(r)}{1-\bar{V}(r)P(r)}\,, \tag{5.7}$$

where $\bar{V}(r)$ is the bare Coulomb potential and $P(r)$ is a polarization function. Explicit values for onsite interaction U, nearest-neighbor interaction V and the nearest neighbor hopping t for unstrained and strained graphene have been calculated in Ref. [156], exhibiting a linear dependence of U, V, t on strain. We directly take the values therein, available till the fourth-nearest neighbor, as the input for our calculations. The longer-ranged part of the Coulomb-tail is affected by the surrounding electrons leading to a modified dielectric constant, i.e. $1/r \to 1/[r(1+\pi\, r_s/2)]$ where $r_s = e^2/(\kappa\hbar v_F)$ is the Wigner-Seitz radius of monolayer graphene which depends on the fermi velocity $v_F = \frac{\sqrt{3}}{2} t\, a$, with $a = a_0(1+\eta)$. Alternatively, we parametrize the Coulomb-tail with an artificial dielectric constant ϵ, i.e. $1/r \to 1/(\epsilon\, r)$, which is extrapolated from the available short range terms.

We note that in the limit $r \to \infty$ the Coulomb potential approaches $1/r$ again, i.e. $\epsilon \to 1$, as the two-dimensional fermion degrees of freedom cannot modify the three-dimensional Coulomb potential. Here, we do not take into account this latter effect. For better comparison, the cRPA values of terms other than U, V under strain

are taken to be the same values as in Ref. [138].

Note the fact that the constrained RPA only includes particle-hole processes which involve high energy bands away from the Fermi level. Thus, the cRPA interaction parameters contain the screening effects from bands which are neglected in our tight binding model, but not those arising purely from the considered π-bands.

Ohno interpolation formula

In the context of biaxially strained graphene it was suggested in Ref. [156], that the Coulomb interaction can be modeled by the Ohno interpolation formula [104]

$$V(r_{ij}, \epsilon) = \frac{U}{\sqrt{1 + \left(\epsilon \frac{U}{e^2} r_{ij}\right)^2}}\,, \tag{5.8}$$

where $V(0) = U$ and ϵ is a variable screening and for large distances $r \to \infty$ approaches $V(r) \to e^2/(\epsilon\, r)$. The screening parameter ϵ can generally be tuned in the interval $\epsilon \in [0, \infty)$, where $\epsilon \to \infty$ results in a purely local onsite interaction $V(r_{ij}, \infty) = U\, \delta_{ij}$. Furthermore, $\epsilon = 0$ is the limit of a constant (non-local) interaction $V(r_{ij}, 0) = U$ and $\epsilon = 1$ represents the case of benzene [13]. Ref. [156] argues that employing the values for the interaction parameters U and V_1 as given for phenalenyl (3H – $C_{13}H_9$) molecule from the quantum chemistry Pariser-Parr-Pople (QC-PPP) method provide an upper bound for the Hubbard U and the interaction potential $V(r)$, see Ref. [146]. The transformation matrix for the interaction profile as given by the QC-PPP method is not positive definite, therefore it was not accessible to the QMC methods promoted in Ref. [146]. We explicitly study this type of interaction profile and variations of it taking account for the fact that the interaction parameters are only known approximately.

A finite strain η can be included employing the strategy suggested in Ref. [138]: Replace $r \to (1 + \eta)r$ in $V(r)$ and use $t \to t_0 e^{-3.37\eta}$. The QC-PPP method is designed to describe small system sizes and larger systems are expected to show stronger screening and therefore a smaller $V(r)$. We therefore interpret these parameters as providing an upper limit for a realistic choice of the interaction profile and note that extrapolation to larger systems has to be interpreted cautiously.

5.3. Method and implementation

We employ a functional Renormalization Group method within the one-loop, one-particle-irreducible (1PI) formalism for fermionic systems introduced in Ch. 2 to perform a weak-coupling instability analysis as explained in Sec. 2.6. The choice of regulator follows the so-called Ω-scheme [61], i.e. infrared divergences are regularized by a soft frequency cutoff introduced in Sec. 2.4. External frequency dependences and self-energies are ignored. For the implementation of the fRG we use the Truncated Unity scheme presented in Ch. 3, which leads to the flow equations in Eqs. (3.18). Briefly put, the scheme splits the two-particle coupling function into three channels P, C, D which correspond to pairing, magnetic, and charge correlations, respectively. These channels are defined so that each of them carries a single dependence $\mathbf{l}$ on one of the possible singular momentum dependences of the coupling function. The remaining weaker dependences in each channel are expanded onto a form factor basis of lattice harmonics (see Sec. 3.3.1 and App. D).

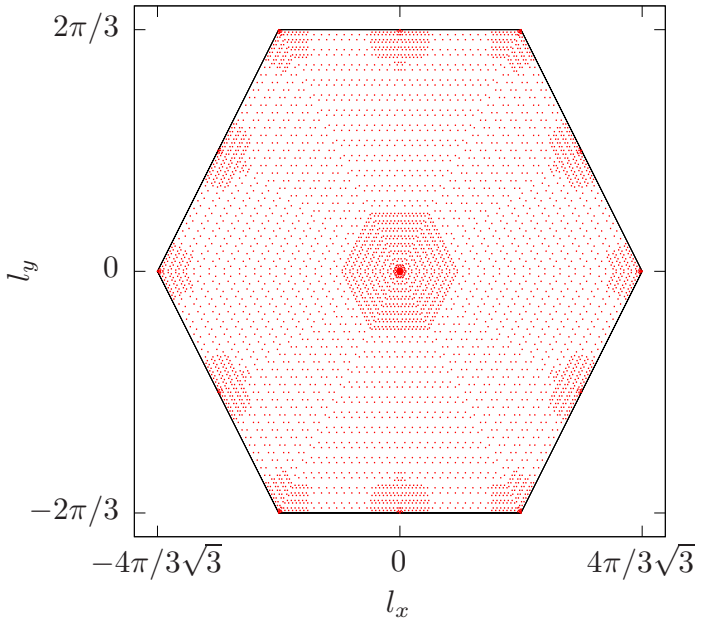

Figure 5.2.: Brillouin zone (BZ) of the honeycomb lattice with typical wave-vector discretization as implemented in the TUfRG approach. We choose a resolution of the wave-vector discretization with a higher density around high-symmetry points, i.e. close to the center of the BZ, Γ, the corners of the BZ, K and K', and the three M-points (M_1, M_2, M_3).

The initial condition for the flow is given by the microscopic bare coupling V_{Ω_0}, provided that the starting scale Ω_0 is several orders of magnitude bigger than the bandwidth. Extended density-density bare interactions are contained in the initial condition for the D channel, and the onsite bare interaction is split equally among channels, as explained in Sec. 3.3.4. Many-body instabilities towards ordered states become manifest as divergences of specific coupling components in the flow to lower energies. The nature of the symmetry-broken ground state is encoded by the diverging components, and the scale of divergence provides an upper estimate for the critical scale Ω_c, which, in turn, can be used as an order of magnitude estimate for a gap or an ordering temperature. The transfer momentum $\mathbf{l}$ and form factor indices m, n at which divergences occur reveal the ordering vector and the symmetry of the order parameter, respectively.

The TUfRG flow equations are solved numerically by a discretization of wavevector dependences in the Brillouin zone into N_k regions, reducing the integro-differential flow equation to a coupled system of $3N_b^4 \times N_{ff}^2 \times N_k$ non-linear ordinary differential equations, where N_b is the number of bands and N_{ff} is the number of form factor functions. The ODE system is then solved using a third order Adams-Bashforth method, and higher order for convergence tests.. The Brillouin zone mesh we normally use, representing the discretization of the transfer momentum, is that of Fig. 5.2, with 6097 points and a very high density around the Γ point. They are constructed in a recursive way, starting from the irreducible ΓMK triangle in the BZ and dividing it up into 4 similar triangles in each recursion. The minimal number of recursions is 5, the density around the M and K points corresponds to 7 and 8 recursions respectively, and over 40 recursive steps are done around the Γ point. This meshes are fixed during the flow, making sure that the minimum density of points is high enough to detect instabilities of any relevant ordering vector. However, the momentum integration of

the one-loop integrals is done adaptively using denser discretizations of at least a few million points, ensuring that the relative error of these integrals falls below 1%. The usual number of form-factor shells considered is 3 and 4, going up to the fifth one for convergence tests.

5.4. Results

We study the interaction-induced quantum-many-body instabilities of spin-1/2 fermions on graphene's honeycomb lattice starting from the pure $t-U$ model and systematically considering extended interactions and their effect on the system stability. The short-range regime is studied starting from the local model via a stepwise inclusion of interaction terms up to a few neighbors in order to motivate the lower bound for the study of long-range interactions. We later connect to the lattice QMC results that have studied the ground-state of the model using different sets of *ab-initio* interaction parameters and an effective long-range tail $\sim 1/(\epsilon\, r)$, cf. Ulybishev *et al.* and Tang *et al.*. For that matter, we include the effect of strain to profiles given by cRPA interaction parameters and the Ohno interpolation formula. Moreover, we study the effect of a second-nearest neighbor hopping on the strained long-range interacting system.

5.4.1. cRPA parameters without strain

Starting from the simple $t-U$ model, we add non-local repulsive terms in a stepwise fashion, using cRPA interaction parameters [156] available till the fourth nearest neighbor, and extrapolating them up to the twentieth neighbor. A nearest-neighbor repulsive coupling V_1 triggers a CDW where occupancy alternates between sublattices, and a V_2 coupling induces a modulated charge density wave with tripled unit cell. The interplay among these coupling terms caused some controversy regarding possible exotic ground states, hinting towards spin liquid and topologically non-trivial phases [112], where most studies focused on the case of spinless fermions. However, in more recent studies they are falling out of favor for the more mundane charge order, both in the spinless [129] as well as in the spin-1/2 case [123, 149]. As shown in Ref. [123] and in the previous chapter, results from our current method do not support exotic phases either, but the high momentum resolution allowed to see novel incommensurate charge ordering tendencies instead. These arise due to competition effects, with the charge ordering patterns triggered by first and second nearest neighbor interactions being incompatible and the system entering geometrical frustration.

Adding further agents to the competition, i.e. other non-local density-density interaction terms V_i with $i > 2$, reveals a rich and complex landscape of charge ordering instabilities, interspersed by points where the system remains semimetallic due to the charge ordering tendencies being balanced and suppressing magnetism. Here, we used cRPA interaction parameters as a reference. The complex picture obtained is expected to extrapolate to other realistic parameter choices on a qualitative level. Results are shown in Fig. 5.3, which can be viewed as a path in a 20-dimensional parameter space, starting from just onsite and first nearest neighbor cRPA parameters, and each step being taken in a new coupling direction. When considered alone, pure n^{th}-nearest-neighbor interactions result in different tendencies depending on whether the interaction is inter-lattice or intra-lattice. Inter-lattice repulsive terms are all equivalently minimized by the standard CDW, together with more complex patterns for interactions other than V_1, which are usually sub-leading due to degeneracy. Intra-

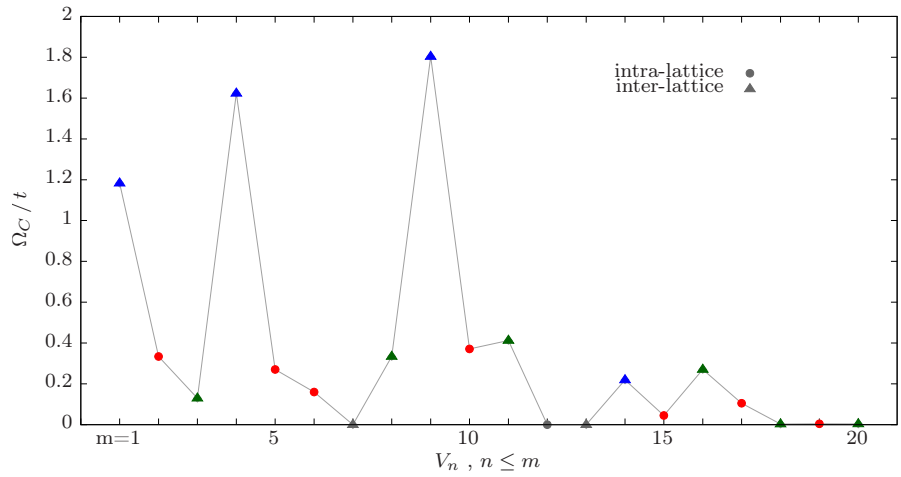

Figure 5.3.: Critical scales vs. the number of considered nearest neighbor interactions. Inter-lattice terms are marked by triangles, whereas intra-lattice terms are represented by circles. For inter-lattice terms, a further distinction is made depending on the location of the leading ordering vector. Blue triangles correspond to charge ordering tendencies with an ordering vector close to the Γ-point, with the point $m = 1$ being a standard CDW and the only commensurate case. Green triangles are ordering tendencies with ordering vectors anywhere in the BZ other than Γ. Grey points correspond to semimetallic behavior and the absence of an instability.

lattice repulsive terms each support differently modulated charge density waves, with tripled, 9x, and 12x extended unit cells for pure V_2, V_5, and V_6 terms respectively, to name some examples. The rich interplay that arises when considered together shows ordering vectors and critical scales going back and forth, from situations which are very unstable towards incommensurate charge order with a modulation close to that of the CDW, down to situations where the semimetal remains stable. The high critical scales take place when there is a big majority of inter-lattice terms, since they all have the CDW as common tendency. The ordering vectors may lie very close to the Γ point, but due to the presence of other tendencies they stay incommensurate. When the situation is better balanced and the scales drop, ordering vectors may appear anywhere in the BZ. For instance, as seen in Fig. 5.3, adding a V_3 coupling yields a lower Ω_c than for $m = 2$, and an ordering vector close to the K-point. Even though it supports the CDW, V_3 also triggers stripe ordering patterns, manifest as sub-leading peaks in the charge propagator which are 3-fold degenerate and not dominant, but still take part in the competition. To highlight the complexity of the interplay, it must be mentioned that the CDW triggering tendencies in V_1 and V_3 do actually reinforce each other, as critical scales are higher if they are considered together rather than separate, and with all other couplings set to zero. In contrast, if U and V_2 are not set to zero, the additional tendencies brought by V_3 to the interplay lead to a lower critical scale.

This analysis is meant to motivate our choice for the lower bound of the Coulomb tails considered next. We include at least interactions up to the 50^{th} neighbor, where charge order effects are sufficiently suppressed to have a robust semimetal. This is the case for both choices of interaction parameters, either from cRPA or from the Ohno interpolation formula. On the other hand, although the discussion of this intermediate-range physics might not be directly relevant to strained graphene, it is of importance in the context of cold atoms trapped in optical lattices, where this rich

charge order landscapes may be physically realized.

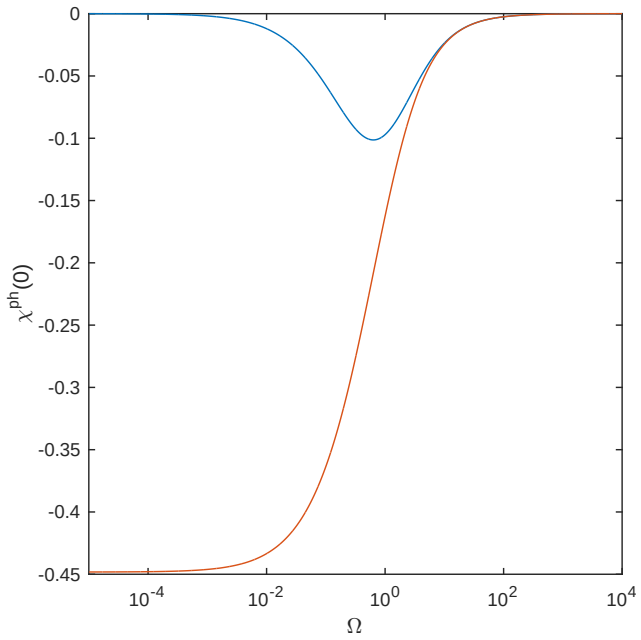

Figure 5.4.: Particle-hole bubble at zero momentum transfer vs. Ω, all in units of t, with intra-band (blue) and inter-band (red) components.

Here, we add a short technical discussion of the RG flow for a stable semimetal, before going into the study of strain-induced instabilities. At $T = 0$ and $t' = \mu = 0$, Coulomb interactions stay unscreened due to the vanishing DOS at the Fermi level. Using the soft frequency Ω-regulator of Ref. [61], the intra-band particle-hole bubble with zero momentum transfer is suppressed by the regulator itself when Ω is large, whereas for small Ω the vanishing DOS brings it down. The inter-band particle-hole bubble does not play a qualitatively relevant role for charge screening [63], and thus we focus on the intra-band components in this discussion. The particle-hole bubble's behavior in flows with the Ω-regulator is shown in App. B and plotted again in Fig. 5.4 for convenience. In the TUfRG flow equations, cf. Eqs. (3.18), the bubbles involved are differentiated respect to Ω. These exhibit a sign change at $\Omega \approx 0.63t$, where the bubble has an extremum. Thus, the Coulomb interaction experiences screening in the flow for $\Omega > 0.63t$, followed by anti-screening as Ω goes to zero, reconstructing the unscreened bare interaction one had for $\Omega \to \infty$. This works out well for single-channel flows with the charge channel only, which is equivalent to RPA. However, in the full flow with all three channels, the additional contributions from inter-channel feedback may prevent the neat reconstruction of the bare interaction, which either saturates to a screened interaction, or overshoots and becomes fully unscreened for a finite Ω. The overestimation is more problematic in practice, since Coulomb interactions suddenly grow huge and may even cause numerical overflows. Introducing a small chemical potential has no effect if it is smaller than the lowest scales we can flow to under this unscreening problematic. A larger μ of the order of such scales ($\sim 10^{-3} - 10^{-2}$) naturally leads to a saturation of unscreening behavior, and as it corresponds to a system with finite DOS, screening remains. Whether it saturates or overshoots depends very sensitively on the choice of parameters, and the order of the ODE solver and step size. Specifically, the unscreening problematic is exacerbated by increasing

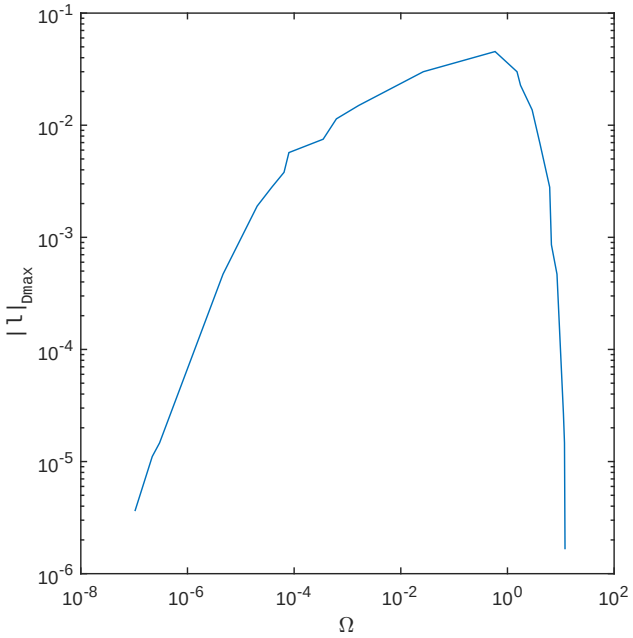

Figure 5.5.: Norm of transfer momentum $\mathbf{l}$ for which D is maximal vs Ω, all in units of t.

the order of the ODE's solver, being more prone to overestimation and even displaying oscillating behavior unless the steps in Ω are taken to be unfeasibly small. Going over to a predictor-corrector scheme like the Adams-Basforth-Moulton multistep method cures the oscillations. Therefore, this effect is most likely a numerical artifact, since we are attempting to obtain a divergent solution using explicit ODE solvers, which lack A-stability. It is thus unsurprising that inaccuracies in the inter-channel feedback, mainly due to form-factor basis truncation, may lead to more severe accumulated inaccuracies in the charge screening behavior. The latter mainly happens near critical values for a magnetic instability in the presence of long-ranged charge correlations (see grey areas in the phase diagrams of next section). In such situations we cannot flow below scales of $\Omega \sim 10^{-3} - 10^{-2}t$ without encountering numerical overflows in the charge channel, due to the overestimated anti-screening.

Fig. 5.5 illustrates another subtlety of the charge unscreening in the Ω-regulator scheme. In the reconstruction of the bare Coulomb interaction taking place at low scales, the maxima of both particle-hole bubble and D propagator do not stay at the Γ point, but at small wave-vectors, which nonetheless tend towards Γ as $\Omega \to 0$. The maxima of χ^{ph} start off at the K points for very high Ω, wander inwards in the BZ and outwards again to the M points as one sweeps across the van Hove singularities in the flow, and inwards again towards the Γ point. The D propagator is peaked at Γ almost for the whole screening stage. However, as the unscreening stage gets closer, both get peaked at small but finite momenta. The bubble peak is located at a slightly bigger wavevector than the propagator, but follows the same trend as depicted in Fig. 5.5.

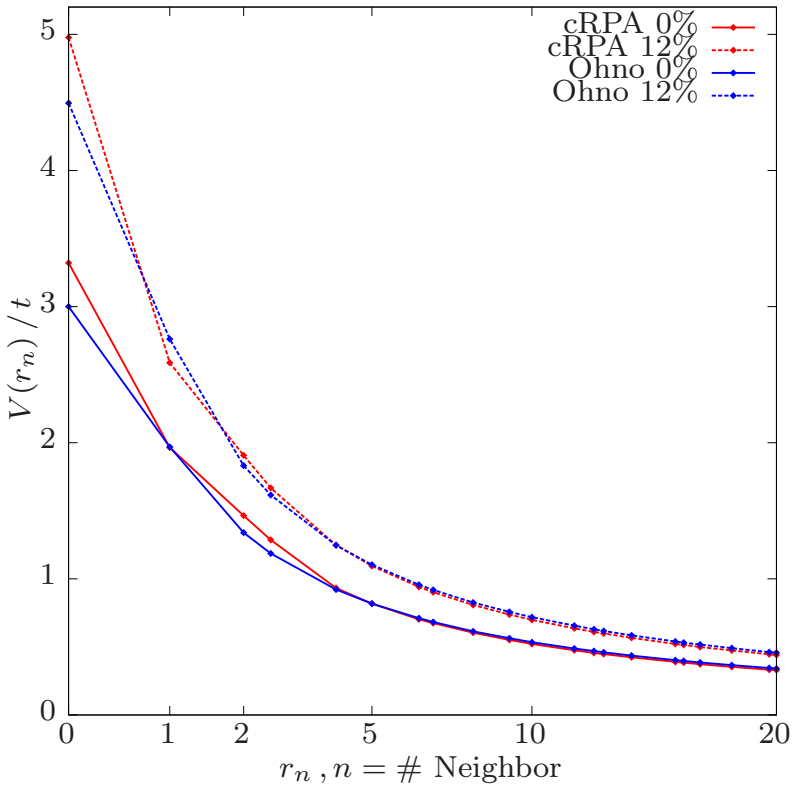

Figure 5.6.: cRPA and Ohno interaction profiles for $\lambda = 1/r_{10^3}$ with 0% and 12% strain.

5.4.2. Effects of strain

The Brillouin zone meshes used allow to resolve interaction profiles including beyond the 10^6-th nearest neighbor. To parameterize the interaction range, instead of including different number of neighbors as done in Sec. 5.4.1, all terms up to the 10^4-th nearest neighbor are considered and an artificial screening factor $e^{-\lambda r}$ is multiplied to the potential to smoothly switch off the long-range tail at the indicated number of nearest-neighbor interactions, i.e. $\lambda = 1/r_n$ with r_n being the distance to the furthest interaction parameter. Further ranged profiles are considered whenever critical strain values do not converge before $\lambda = 1/r_{10^4}$. Strain is accounted for as described in Sec. 5.2.2, with example profiles shown in Fig. 5.6. On the last subsection, we study the effect of including a finite second-nearest-neighbor hopping.

cRPA parameters with strain

Setting t' and μ to zero on our model parameters, we employ a cRPA interaction profile and study the effect of finite strain η on the system's many-body instabilities. The concrete values used are the same as in Refs. [138,156] We find that long-ranged cRPA interaction profiles give rise to an antiferromagnetic SDW instability for a strain larger than a critical value, see Fig. 5.7. The critical strain necessary to induce the instability converges with respect to the inclusion of yet longer ranged Coulomb tails, staying at 6% for profiles ranging up to the 10^5-th neighbor and a corresponding $\lambda = 1/r_{10^5}$. Importantly, we observe that this type of interaction profiles does not give rise to other leading instabilities, but the AF-SDW, i.e. no charge ordering

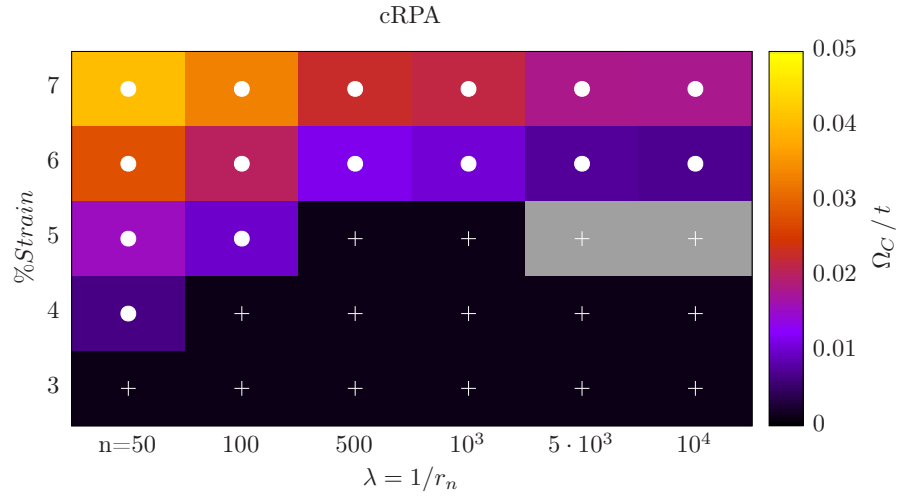

Figure 5.7.: Effect of strain on the electronic instabilities of the model with cRPA interaction parameters. The horizontal axis denotes an artificial screening length set at the n-th neighbor's bond distance. The black regions marked with white crosses represent the semimetallic behavior. Filled white circles indicate an instability towards a SDW-AFM, with corresponding critical scales encoded in the background color. Grey regions are expected to stay semimetallic, but unfortunately we cannot flow down to low enough scales for those points. See text for further details.

tendencies dominate the phase diagram. We have checked that our results are robust with respect to denser wave-vector meshes, the inclusion of a fifth form-factor shell, or the use of a fifth order ODE solver. The dominance of the AF-SDW ordering tendency agrees well with findings from the QMC simulations on a qualitative level. Based on our earlier considerations within the honeycomb-Hubbard model, we expect that our approach overestimates the effects from fermionic fluctuations and therefore gives rise to an underestimated critical strain. This expectation agrees with the result from the QMC calculations where for the cRPA parameters no semi-metal insulator transition could be observed for strains up to 18%.

We note, that there is some ambiguity in the initialization procedure, relating to which channel contains the on-site Hubbard contribution: The most neutral or unbiased choice is to assign 1/3 of it to each of the three channels, resulting in the phase diagram presented here. However, other formally equivalent ways to initialize the onsite term are expected to yield similar results, and we consider them as a consistency check. If the onsite Hubbard U is fully assigned to the magnetic channel, one introduces some bias towards magnetism and obtains a critical strain of 3% for the longer ranged profiles. In contrast, if U is fully assigned to the charge channel instead, a critical strain of 10% is obtained for long ranged profiles. A more detailed discussion of this issue can be found in Sec. 3.3.4. The qualitative picture that the cRPA interaction profile gives rise to an AF-SDW transition beyond a critical strain is nevertheless the same, independent of initialization.

Ohno formula and strain

Next, setting again t' and μ to zero on our model parameters, we study Ohno interaction profiles with finite strain η which remained elusive to the QMC calculations. We

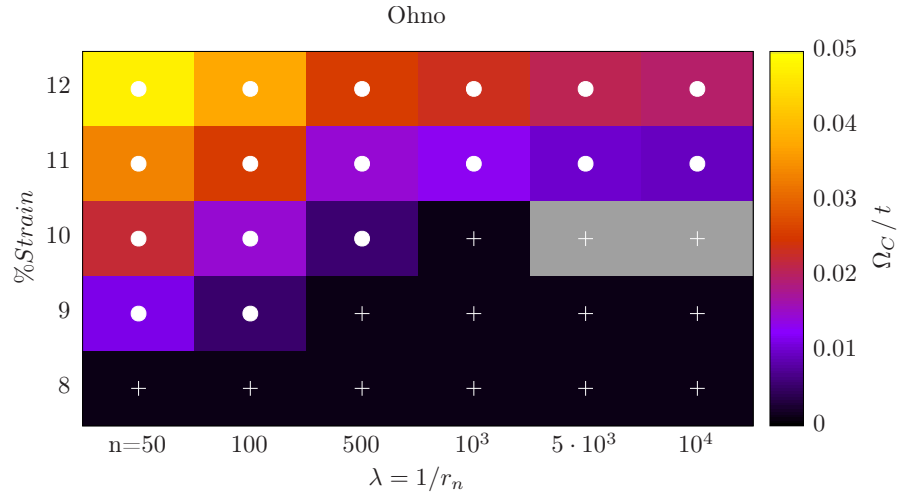

Figure 5.8.: Effect of strain on the electronic instabilities of the model with Ohno interaction parameters. The horizontal axis denotes an artificial screening length set at the n-th neighbor's bond distance. The black regions marked with white crosses represent the semimetallic behavior. Filled white circles indicate an instability towards a SDW-AFM, with corresponding critical scales encoded in the background color. Grey regions are expected to stay semimetallic, but unfortunately we cannot flow down to low enough scales for those points. See text for further details.

set the unstrained values in Eq. (5.8) to $U/t = 3.0$, and choose ϵ so that $V_1/t = 2.0$, then proceed analogously to the previous subsection, cf. Fig. 5.8. The choice of a slightly smaller U than in cRPA is purposely done for contrast, keeping a similarly strong non-local tail. Also note that under strain, the cRPA parameters tend faster towards a localized interaction than the Ohno parameters. This leads to a considerably larger critical strain for this interaction profile as compared to the strained cRPA parameters. In fact, the critical strain necessary to induce an instability converges to 11% when including up to the 10^5-th neighbor in the interaction. Also, in this case no leading instability other than the AF-SDW appears. Our results are as well robust respect to the use of denser wave-vector meshes, the inclusion of a fifth form-factor shell, or the use of a fifth order ODE solver. Again, there is some ambiguity in the initialization procedure. The results presented in Fig. 5.8 correspond to the most neutral or unbiased choice, distributing the onsite U contribution equally among the three channels. With the on-site Hubbard U fully contained in the magnetic channel, we get a critical strain of 8% for the longer ranged profiles, and if U is fully assigned to the charge channel instead, the critical strain is 15%. As a general trend, we observe that a more strongly pronounced long-range tail in the interaction profile tends to increase the critical strain required to induce a semi-metal-insulator transition or, in other words, it stabilizes the semi-metallic behavior of the graphene model.

We also consider deviations from the model parameters used so far, with the aim of testing the qualitative robustness of the SM to AF-SDW transition indicated by our instability analysis. We find that slight modifications of ϵ in Eq. (5.8) result in a shift of the critical strain, but does not change the nature of the instability, i.e. the tendency towards the AF-SDW instability prevails. In Fig. 5.9, we exhibit the effect of increasing ϵ to a value that yields $V_1/t = 1.75$, resulting in a smaller critical strain. This is in agreement with our earlier observation since the larger value of ϵ leads to a less-pronounced long-range tail. Setting smaller ϵ's aggravates

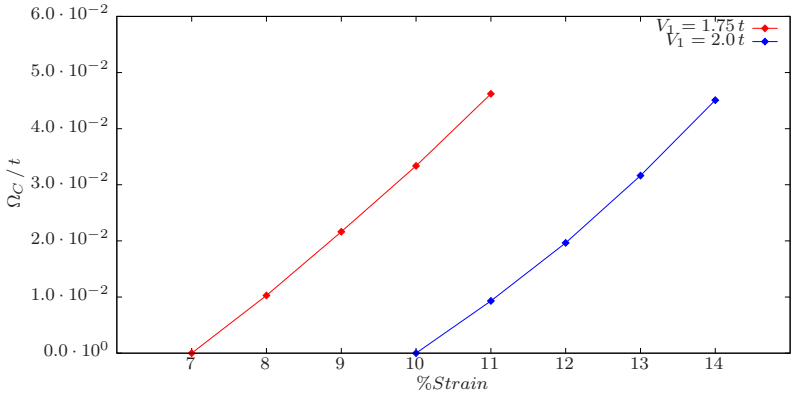

Figure 5.9.: Critical scales vs. strain for different interaction strengths of the Coulomb tail in the Ohno formula.

the aforementioned technical difficulties that arise with the unscreening of charge interactions. For instance, when choosing ϵ such that $V_1/t = 2.25$, we can only say that the critical strain is shifted to about 15-18%, but cannot give a more definite answer. Instead of rising the non-local terms to higher values, we can alternatively lower the on-site interaction strength. If we set $U/t = 2.5$, keeping the rest unchanged, we obtain an instability to incommensurate charge order for strains above 10-15%, and recover the antiferromagnet when strain reaches about 30%. In these comparisons, one has to push the ratio between on-site and extended terms to unrealistic values in order to trigger instabilities other than the AF-SDW. This is due to the fact that the Coulomb tail is modified as a whole, which does not sufficiently disturb the balanced competition among charge ordering tendencies. However, if we disturb that balance, charge order is much more likely to appear. In the original set of parameters, with $U/t = 3.0$ and $\epsilon = 1.25$, it suffices to increase $V_1/t = 2.0$ to $V_1/t = 2.25$ while keeping the rest unchanged, to make even the unstrained system unstable towards an iCDW. The quantitative impact of this deviations has not been tested for convergence.

t-t'-Hubbard-Coulomb model with strain

Finally, we study the full model Hamiltonian to explore a close-to-realistic model for graphene. To that end, we include a second-nearest neighbor hopping as well as the two interaction profiles from the cRPA and the Ohno method and investigate the effect of a finite amount of strain. Explicitly, we compare the critical scales for the appearance of a many-body instability for three different choices of the unstrained second-nearest neighbor hopping $t' \in \{0, -0.1t, -0.2t\}$. We note that the application of strain quickly reduces the value of the second-nearest neighbor hopping t' following the relation in Eq. (5.6), while increasing the interaction strength relative to t. Therefore, we expect a smaller impact of t' on the critical scales as compared to the pure modification of the Hubbard interaction as studied in the previous chapter. The results of this study are shown in Fig. 5.10 and confirm this expectation. For both, the cRPA as well as the Ohno interaction profiles, the critical scales for different values of strain only weakly depend on the chosen unstrained value of the second-nearest neighbor hopping t'.

Finally, we comment on a suggestion for an effective honeycomb Hubbard model derived from the honeycomb Hubbard-Coulomb model as put forward by Schüler *et al* in Ref. [133]. Noting that non-local charge interactions stabilize the Dirac semimetal against magnetic ordering, and provided the absence of other instabilities,

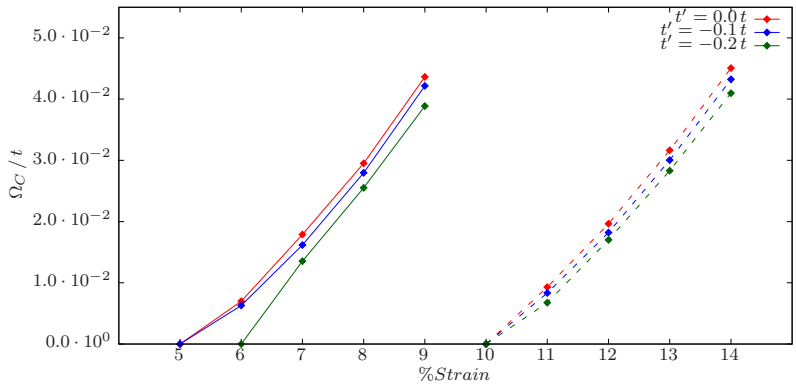

Figure 5.10.: Critical scales vs. strain for different values of the second-nearest-neighbor hopping with cRPA (solid) and Ohno (dashed) interaction parameters.

they proposed a pure on-site Hubbard model with downscaled local interaction U^* as a reasonable approximation. More specifically, one would then have $U^* = U - \bar{V}$, where $\bar{V}$ is a weighted average of non-local terms which they further approximate by $\bar{V} \approx V_1$. Concrete values for the interaction profiles considered in this work can be found in Table 5.1, where a common trend of $U_C^* \approx 1.75\,t$ can be inferred, which is to be compared to the $U_c \approx 2.7\,t$ of the original local Hubbard model. Nonetheless, quantitative differences aside, our results support the validity of an effective on-site model. The crucial aspect here is the absence of leading ordering tendencies other than antiferromagnetism.

Table 5.1.: Effective Hubbard repulsion according to Ref. [133] for the different interaction profiles at different values of strain. Ohno 1 and 2 denote the two different profiles considered in Fig. 5.9 with stronger and weaker Coulomb tails, respectively. See the text for further discussion.

i.a. profile	strain	U/t	V_1/t	U^*/t	instability
cRPA	0%	3.3	2.0	1.3	x
cRPA	6%	4.05	2.25	1.8	✓
cRPA	12%	5.0	2.6	2.4	✓
Ohno 1	0%	3.0	2.0	1.0	x
Ohno 1	12%	4.5	2.75	1.75	✓
Ohno 2	0%	3.0	1.75	1.25	x
Ohno 2	8%	3.9	2.15	1.75	✓

5.5. Conclusions

In the following, we summarize our main results. First, the consecutive inclusion of more and more remote non-local interaction terms up to the 20^{th}-nearest neighbor following the unstrained cRPA interaction profile provides a sequence of different incommensurate charge ordering patterns. The critical scales of these charge orders discontinuously jump from rather large values to zero and back, indicating a strong competition between these orders. Magnetic instabilities are suppressed. When including enough interaction terms, the competition between the charge ordering patterns drives the system into a frustrated regime where no instability appears and semi-

metallic behavior prevails. We conclude that the semi-metallic behavior of graphene is not a result of the smallness of interactions but due to a strong competition and an eventual frustration of different ordering tendencies.

This frustration can be lifted by application of a biaxial strain which we have studied by employing two different types of long-ranged interaction profiles, i.e. the cRPA and the Ohno interpolation to take account for the uncertainties in the determination of interaction parameters. We showed that for both the cRPA as well as the Ohno profiles, a critical strain exists beyond which the system develops a quantum many-body instability. The TUfRG values for the critical strain lie between about 5% (cRPA) and 11% (Ohno). Notably, the nature of the leading instability for these long-ranged interaction profiles is of AF-SDW type, i.e. charge ordering tendencies are never preferred despite their importance for intermediate-range potentials. This option could not be explored before, as the QMC calculations typically suffer from a sign-problem for interaction potentials with a strong tail. The nature of the possible instabilities turn out to be the same for both pure on-site and long-ranged interacting models, which also persists under inclusion of a finite second-nearest neighbor hopping term. Thus, this is supporting evidence for the qualitative validity of effective honeycomb t-U-Hubbard models in place of t-t'-Hubbard-Coulomb models.

Generally, the results of the TUfRG approach presented here overestimate the effect of fermionic fluctuations which leads to an earlier onset of ordering tendencies. We conjecture that this is in part caused by the neglect of self-energy effects which would, for example, lead to finite lifetime effects [41, 57, 58] and the renormalization of the Fermi velocity [29]. Therefore, for more quantitative estimates, an inclusion of self-energy effects within the fRG approach would be desirable. We expect this task to be numerically demanding but feasible in the future.

6. Conclusion

In this thesis we have developed a new functional Renormalization Group scheme for interacting fermions on two-dimensional lattices, which offers important computational advantages in terms of numerical efficiency and scalability, and applied it to the Hubbard model on the honeycomb lattice including the challenging description of long-ranged Coulomb interactions.

Our methodological developments build on previous work which introduced parametrizations of the two-particle vertex function that are more efficient than a straight discretization of its dependences. We followed mainly on the work by Husemann *et al.* [61] and Wang *et al.* [151], combining their approaches into a scheme which retains the advantages of both of its predecessors. These two earlier approaches both rely on reducing the three-momentum dependent two-particle interaction to several simpler objects, each of which contains only one of the singular momentum dependences of the original interaction. In the exchange boson parametrization by Husemann *et al.* [61], the two-particle coupling is split into three channels, whereas the Singular Mode fRG of Wang *et al.* [151] introduces three different approximations of the coupling itself. In the former scheme, performing the decomposition for every instance of the coupling in the flow equations leads to a complicated diagrammatic structure which compromises the numerical performance. The latter scheme has the disadvantage of introducing some ambiguity by having several different versions of the coupling.

In this work, we showed how the two aforementioned approaches can be related via an insertion of truncated partitions of unity, in the Truncated Unity fRG [87]. This new approach has allowed us to separate fermionic propagators in loop integrals from the exchange propagators which describe the channel decomposed interaction. This way, the loop integrals not only become much simpler, but its different components also stay independent of each other, providing a highly scalable numerical implementation. Moreover, the scheme keeps an unequivocal prescription to reconstruct the original coupling function in its full dependences, avoiding ambiguities.

The implementation of the TUfRG has been focused on achieving a high resolution of wavevector dependences of the effective interactions, leaving out frequency dependences and self-energy corrections for now. We first applied the TUfRG to the study of the extended Hubbard model on the honeycomb lattice at half-filling, including up to the second-nearest neighbor for bare interactions and hopping terms. Despite only including momentum and band degrees of freedom, the present implementation has provided us with a new scenario of ordering tendencies in the honeycomb lattice, compared with earlier fRG results using the Fermi surface patching scheme. In particular, it has allowed us to find agreement with recent studies which support a dominance of charge order over a topological Mott insulating state for strong second-nearest neighbor bare interactions [14, 20, 65, 99, 129, 149]. In contrast to previous fRG results, where the topological Mott insulator eventually dominates when second-nearest neighbor repulsion is strong enough, no such instability is seen by the TUfRG even for second-nearest neighbor coupling strengths exceeding the bandwidth. The high wavevector resolution achieved with the TUfRG has allowed us to detect novel charge ordering instabilities of incommensurate ordering wavevectors [123]. These

incommensurate charge density waves arise due to the geometrically frustrated situation which results from having several competing interactions in the density channel, each favoring different charge ordering patters which are mutually incompatible in terms of energy minimization. The competition among ordering tendencies has also led to a strong suppression of critical scales in boundary regions separating different dominating instabilities, in particular for parameter combinations which are close to the realistic values coming from *ab initio* calculations, where tendencies may find balance. In addition to the study of different interaction parameter combinations, we also extended the kinetic parameters to include a second nearest neighbor hopping t', which is taken together with a chemical potential shift in order to retain the Dirac cones at the Fermi level. Within the range of suggested *ab initio* values for t', we found no effect on the critical onsite coupling strength necessary to induce an antiferromagnetic instability, since a finite t' does not affect the low energy spectrum in the vicinity of the Dirac points. However, we did find a considerable suppression of critical scales in the antiferromagnetic transition, suggesting a reduction of up to 40% for the expected gap sizes and critical temperatures. We were able to confirm that this effect is not just a consequence of the breaking of particle-hole symmetry of the band structure and the subsequent deviation from perfect nesting in the particle-hole channel, but results from an enhanced particle-particle channel and the complex interplay between different interaction channels [124].

We continued by considerably extending the range of bare interaction terms included, refining the discretization of momentum dependences enough to resolve up to the 10^5-th nearest neighbor. We proceeded by first including repulsive bare interactions in a stepwise fashion up to the 20^{th}-nearest neighbor, using *ab initio* values from cRPA calculations in the literature [156]. Similarly to the analysis including only first and second-nearest neighbor interactions, incommensurate charge ordering patterns are observed, since such additional coupling terms induce yet further different charge ordering patters which compete with those driven by either V_1 or V_2. Intra-lattice repulsive terms each support differently modulated charge density waves, and though inter-lattice repulsive terms are all equivalently minimized by the standard CDW, they also drive more complex patterns for interactions other than V_1, which are usually sub-leading due to degeneracy but may impact the critical scales. All these charge ordering tendencies compete with each other and with magnetism, so that when enough competing terms are included and their relative strengths are balanced, the system stays semimetallic in spite of these coupling terms all being well above their respective individual critical values for inducing an instability. As a result, in this intermediate range connecting short and longer ranged interactions, a rich and complex landscape of charge ordering instabilities is revealed, interspersed by points where the system remains semimetallic. We found that including interactions up to the 50^{th}-nearest neighbor is enough to have a robust semimetal, using either cRPA values or other *ab initio* interaction parameters like those obtained from the Ohno formula. Thus, there we concluded that the semimetallic behavior of graphene is not necessarily a consequence of interactions being too weak to induce a symmetry breaking transition, but due to a strong competition and an eventual frustration of different ordering tendencies.

Finally, we considered the effects of isotropic strain on the destabilization of the semimetal by breaking the aforementioned balanced ordering tendencies. Strain provides a viable way to modify interaction parameters experimentally, strengthening interactions respect to kinetic terms, and altering the spatial profile of the interaction by changing the relative strength of the different interaction terms acting at different lattice distances. The higher the strain, the stronger and more localized interactions become, bringing the system closer to a purely local onsite interaction. Therefore,

there is a critical strain value above which the system becomes unstable towards entering a symmetry broken phase. We considered the two sets of *ab initio* interaction parameters for graphene mentioned above and their extension for a strained system, namely, cRPA parameters from the literature and parameters resulting from the application of the Ohno formula. We also studied the impact of including a second-nearest neighbor hopping term in the free kinetic dispersion. Earlier Quantum Monte-Carlo studies were limited in their choice of interaction parameters, which had to decay fast enough with distance to avoid a sign problem. They could not consider a finite second-nearest neighbor hopping either for the same reason. The TUfRG scheme is not bound by such limitations, but is not quantitatively accurate. Thus, although we refrain from giving a definite answer to the critical strain necessary to induce an instability, we could qualitatively confirm that the only arising instability is of antiferromagnetic nature. Moreover, we could also analyze the trends for the critical strain. Although formally both interaction profiles used have a Coulombic decay at long distances, they differ in the short-range regime, with the cRPA parameters taking a more localized shape. We saw that quicker spatial decays of the interaction profile lead to lower critical strains for antiferromagnetic order. This led to relatively lower critical strains for the cRPA parameters compared to the Ohno ones. Conversely, we also found that increasing the interaction strength of the long-range tail stabilizes the semi-metallic behavior, requiring higher critical strains. If one lowers the onsite interaction instead, keeping the rest unchanged, we observed that one eventually obtains an intermediate incommensurate charge density wave regime, in between semimetallic and antiferromagnetic regions. However, for that to happen, we had to lower the ratio between on-site and extended terms to unrealistic values in order to trigger instabilities other than the antiferromagnet.

Regarding the impact of including a second-nearest neighbor hopping in the strained long-range interacting system, we observed a much milder effect on critical scales than for the pure onsite model studied before. This was expected, since the application of strain reduces the value of the second-nearest neighbor hopping t' exponentially, while simultaneously increasing the onsite interaction strength relative to t. Since neither the long-range Coulomb tail in the interaction, nor further hopping terms in the kinetic part seem to disturb the qualitative nature of the semi-metal to antiferromagnet transition, we could also corroborate that the simpler pure onsite Hubbard model usually employed within other approaches does capture the relevant physics. The extensions considered in our work would definitely impact the quantitative predictions, but they would not deviate the system from its known qualitative behavior.

As for future prospects on fRG studies of graphene based systems, a more complete description including frequency dependences, self-energy corrections, and collective bosonic degrees of freedom emerging at the transition would be necessary for quantitatively reliable predictions. So far, the inclusion of long-ranged interactions has already allowed to reconcile the accepted semimetallic nature of single layer graphene with the fRG results, which within older implementation schemes had predicted ordered phases for realistic choices of interaction parameters. This discrepancy problem is not exclusive to the single-layer system, but affects predictions for many-layer systems as well. The current Fermi surface patching fRG results for critical scales in graphene bilayers are still a few orders of magnitude larger than those observed in experiments. Adding further competing tendencies in the form of longer ranged interactions could well cure this problem as it did for single-layer graphene. Moreover, despite bilayer honeycomb models being generally regarded as having a finite density of states at the Fermi level due to a parabolic dispersion, the inclusion of diagonal inter-layer hopping terms causing trigonal warping results in a linear low-energy dis-

persion. Recently, it has been argued that this effect may as well arise dynamically due to interactions [110]. In either case, and equivalently for other non-graphene based Dirac systems, the momentum resolution achievable in the TUfRG and the related inclusion of long-range couplings may well provide new qualitative perspectives or help to reach a better quantitative agreement. Aside from Dirac systems, where the long-ranged nature of interactions should persist, our approach can also be employed to study how screening develops in more general systems with a finite DOS at the Fermi level. This provides a more reliable account of charge screening than RPA and related methods. Moreover, even if we know that the relevant interaction terms for such systems are typically short-ranged, because they are the only terms that remain active at low energies, it is more appropriate to consider the actual Coulomb bare interaction at high energies than to directly start the flow with an effective screened interaction. Instead of relying on some guess about the strength and relevant range of non-local interaction terms near the Fermi level, one can just let the RG flow do the job. Furthermore, the presence of sizable non-local couplings at intermediate scales during the flow may well influence the outcome qualitatively, or at least quantitatively. For some short term technical prospects on our current numerical implementation, see App. D.

Appendices

A. Channel decomposition in real space

The convention for momenta used in the channel decomposition is here recast in real space. Although the derivation is straightforward, it will shed light on our convention for the expanded momentum dependences and truncation procedure. The real space expressions will also be useful for later symmetry considerations.

A general coupling function V in momentum space is related to its real space version via

$$V(\mathbf{k}_1, \mathbf{k}_2, \mathbf{k}_3) = \sum_{\mathbf{R}_1 \ldots \mathbf{R}_4} e^{-i(\mathbf{R}_1\mathbf{k}_1 + \mathbf{R}_2\mathbf{k}_2 - \mathbf{R}_3\mathbf{k}_3 - \mathbf{R}_4\mathbf{k}_4)}\, V(\mathbf{R}_1, \mathbf{R}_2, \mathbf{R}_3, \mathbf{R}_4)$$

where the sums include normalization factors and band indices are ignored. The translation invariance of V in real space is implicitly assumed, and it reduces the R sums and V dependences to three relative differences among position vectors, also resulting in a delta function for momentum conservation. Let us rewrite the expression above in terms of the transfer momenta $\mathbf{l}_P, \mathbf{l}_C, \mathbf{l}_D$ via

$$\begin{aligned}
\mathbf{k}_1 &= \frac{\mathbf{l}_P + \mathbf{l}_C + \mathbf{l}_D}{2}\,, \\
\mathbf{k}_2 &= \frac{\mathbf{l}_P - \mathbf{l}_C - \mathbf{l}_D}{2}\,, \\
\mathbf{k}_3 &= \frac{\mathbf{l}_P + \mathbf{l}_C - \mathbf{l}_D}{2}\,, \\
\mathbf{k}_4 &= \frac{\mathbf{l}_P - \mathbf{l}_C + \mathbf{l}_D}{2}\,,
\end{aligned}$$

to get

$$V(\mathbf{k}_1, \mathbf{k}_2, \mathbf{k}_3) = \sum_{\mathbf{R}_P, \mathbf{R}_C, \mathbf{R}_D} e^{-i(\mathbf{R}_P\mathbf{l}_P + \mathbf{R}_C\mathbf{l}_C + \mathbf{R}_D\mathbf{l}_D)}\, \tilde{V}(\mathbf{R}_P, \mathbf{R}_C, \mathbf{R}_D)\, \delta(\mathbf{k}_1 + \mathbf{k}_2 - \mathbf{k}_3 - \mathbf{k}_4)\,,$$

with

$$\begin{aligned}
\mathbf{R}_P &= \frac{\mathbf{R}_1 + \mathbf{R}_2 - \mathbf{R}_3 - \mathbf{R}_4}{2}\,, \\
\mathbf{R}_C &= \frac{\mathbf{R}_1 - \mathbf{R}_2 - \mathbf{R}_3 + \mathbf{R}_4}{2}\,, \\
\mathbf{R}_D &= \frac{\mathbf{R}_1 - \mathbf{R}_2 + \mathbf{R}_3 - \mathbf{R}_4}{2}\,,
\end{aligned}$$

and where we defined $\tilde{V}$ respect to the original coupling function as

$$\begin{aligned}\tilde{V}(\mathbf{R}_P, \mathbf{R}_C, \mathbf{R}_D) =& V(\mathbf{R}_P + \mathbf{R}_D,\, \mathbf{R}_P - \mathbf{R}_C,\, \mathbf{R}_D - \mathbf{R}_C,\, \mathbf{0}) \\ =& V(\mathbf{R}_1 - \mathbf{R}_4,\, \mathbf{R}_2 - \mathbf{R}_4,\, \mathbf{R}_3 - \mathbf{R}_4,\, \mathbf{0})\,.\end{aligned}$$

Now, rearranging the dependences in transfer momenta into the form of the projected V's and single-channel coupling functions for each channel, namely as

$$\Phi^{\mathrm{P}}_{\mathbf{l}_P, \frac{\mathbf{l}_C + \mathbf{l}_D}{2}, \frac{\mathbf{l}_C - \mathbf{l}_D}{2}} \quad \Big| \quad \Phi^{\mathrm{C}}_{\mathbf{l}_C, \frac{\mathbf{l}_P + \mathbf{l}_D}{2}, \frac{\mathbf{l}_P - \mathbf{l}_D}{2}} \quad \Big| \quad \Phi^{\mathrm{D}}_{\mathbf{l}_D, \frac{\mathbf{l}_P + \mathbf{l}_C}{2}, \frac{\mathbf{l}_P - \mathbf{l}_C}{2}}$$

leads to the following combinations of position variables for the weak dependences in real space

$$\begin{array}{l|l|l} \mathbf{R}_C + \mathbf{R}_D = \mathbf{R}_1 - \mathbf{R}_2 & \mathbf{R}_P + \mathbf{R}_D = \mathbf{R}_1 - \mathbf{R}_4 & \mathbf{R}_P + \mathbf{R}_C = \mathbf{R}_1 - \mathbf{R}_3 \\ \mathbf{R}_C - \mathbf{R}_D = \mathbf{R}_4 - \mathbf{R}_3 & \mathbf{R}_P - \mathbf{R}_D = \mathbf{R}_2 - \mathbf{R}_3 & \mathbf{R}_P - \mathbf{R}_C = \mathbf{R}_2 - \mathbf{R}_4 \end{array}$$

which will always be Bravais lattice vectors. Respectively denoting them as $\mathbf{R}_{\mathbf{k}}$ and $\mathbf{R}_{\mathbf{k}'}$ in each corresponding channel, one has

$$\begin{aligned}\mathbf{R}_P &= \mathbf{R}_1 - \mathbf{R}_3 - \frac{\mathbf{R}_{\mathbf{k}} + \mathbf{R}_{\mathbf{k}'}}{2}\,, \\ \mathbf{R}_C &= \mathbf{R}_1 - \mathbf{R}_3 - \frac{\mathbf{R}_{\mathbf{k}} + \mathbf{R}_{\mathbf{k}'}}{2}\,, \\ \mathbf{R}_D &= \mathbf{R}_1 - \mathbf{R}_2 - \frac{\mathbf{R}_{\mathbf{k}} - \mathbf{R}_{\mathbf{k}'}}{2}\,,\end{aligned}$$

so that whether the real space variable for the strong dependence is a lattice vector or half a lattice vector, ultimately depends on the particular values of the weak dependences.

B. Loop integrals in the Ω-regularization scheme

Here we give the result after Matsubara summation for the form factor projected bubbles of Eqs. (3.16) with an Ω-regulator. The external frequency is set to zero and self-energies are neglected, so that the regulated Green's functions in Eqs. (3.16) are free fermionic propagators. The Matsubara sum can then be performed analytically, and the remaining momentum integral has the form

$$\chi^{\mathrm{pp/ph},\,bb'}_{m,n}(\mathbf{l}) = \int d\mathbf{p}\, \left(\pm I^{bb'}(\mathbf{p})\right) f^*_m(\mathbf{p})\, f_n(\mathbf{p})$$

with a positive and negative sign for particle-particle and particle-hole bubbles, respectively. Defining $\epsilon^b_\pm(\mathbf{p}) = \epsilon^b(\frac{\mathbf{l}}{2} \pm \mathbf{p})$ for the particle-particle case and $\epsilon^b_\pm(\mathbf{p}) = \pm\epsilon^b(\mathbf{p} \pm \frac{\mathbf{l}}{2})$ for the particle-hole case, and after dealing with some removable singularities, the integrand $I^{bb'}(\mathbf{p})$ takes the following form if $\epsilon^b_+(\mathbf{p})\epsilon^{b'}_-(\mathbf{p}) < 0$

$$I^{bb'}(\mathbf{p}) = \frac{3|\epsilon^b_+(\mathbf{p})||\epsilon^{b'}_-(\mathbf{p})| + 2\left(|\epsilon^b_+(\mathbf{p})| + |\epsilon^{b'}_-(\mathbf{p})|\right)\Omega^2 + \Omega^3}{4\left(|\epsilon^b_+(\mathbf{p})| + \Omega\right)^2\left(|\epsilon^{b'}_-(\mathbf{p})| + \Omega\right)^2},$$

and for $\epsilon^b_+(\mathbf{p})\epsilon^{b'}_-(\mathbf{p}) > 0$, if $\epsilon^b_+(\mathbf{p}) = \epsilon^{b'}_-(\mathbf{p})$

$$I^{bb'}(\mathbf{p}) = \frac{2|\epsilon^b_+(\mathbf{p})| + \Omega}{4\left(|\epsilon^b_+(\mathbf{p})| + \Omega\right)^2},$$

and otherwise

$$\begin{aligned} I^{bb'}(\mathbf{p}) = &\frac{4|\epsilon^b_+(\mathbf{p})|^2|\epsilon^{b'}_-(\mathbf{p})|^2 + 5|\epsilon^b_+(\mathbf{p})||\epsilon^{b'}_-(\mathbf{p})|\left(|\epsilon^b_+(\mathbf{p})| + |\epsilon^{b'}_-(\mathbf{p})|\right)\Omega}{4\left(|\epsilon^b_+(\mathbf{p})| + |\epsilon^{b'}_-(\mathbf{p})|\right)\left(|\epsilon^b_+(\mathbf{p})| + \Omega\right)^2\left(|\epsilon^{b'}_-(\mathbf{p})| + \Omega\right)^2} \\ &+ \frac{2\left(|\epsilon^b_+(\mathbf{p})| + |\epsilon^{b'}_-(\mathbf{p})|\right)^2\Omega^2 + \left(|\epsilon^b_+(\mathbf{p})| + |\epsilon^{b'}_-(\mathbf{p})|\right)\Omega^3}{4\left(|\epsilon^b_+(\mathbf{p})| + |\epsilon^{b'}_-(\mathbf{p})|\right)\left(|\epsilon^b_+(\mathbf{p})| + \Omega\right)^2\left(|\epsilon^{b'}_-(\mathbf{p})| + \Omega\right)^2}. \end{aligned}$$

In the peculiar case of a system with a vanishing density of states at the Fermi level, as in the undoped Hubbard model on the honeycomb lattice studied in this work, some bubble components will be suppressed to zero when approaching $\Omega = 0$. This is shown in Fig. B.1 for the particle-hole bubble at zero momentum transfer, which is small at high scales due to the presence of a regulator, and whose inter-band components are also suppressed at lower scales due to the vanishing density of states.

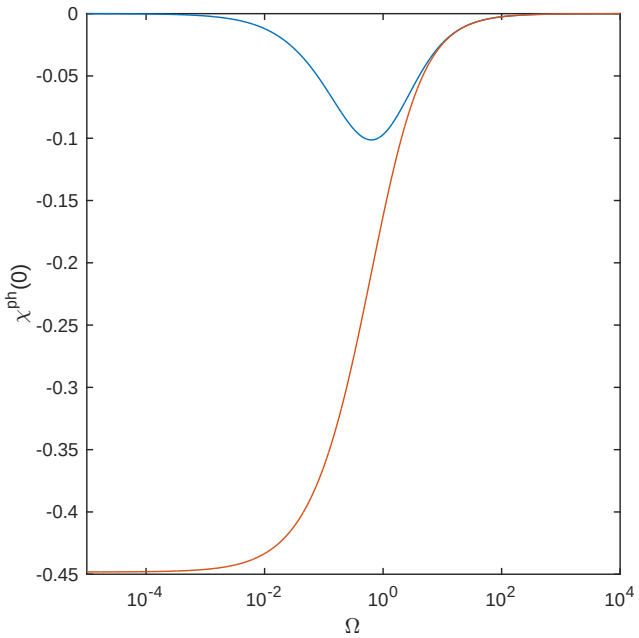

Figure B.1.: Particle-hole bubble at zero momentum transfer vs. Ω, all in units of t, with intra-band (blue) and inter-band (red) components.

C. Form factor basis for irreducible representations of $\mathrm{C_{6v}}$

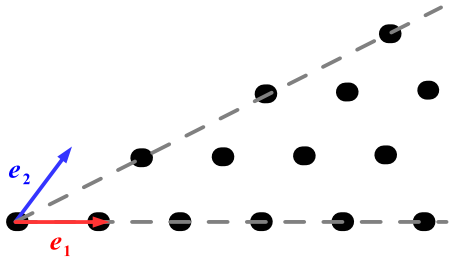

Figure C.1.: Irreducible triangular sector for the hexagonal lattice, from which the rest can be constructed using symmetries. Lattice basis vectors are indicated by $\mathbf{e}_1$ and $\mathbf{e}_2$.

The construction of a form factor basis of lattice harmonics was discussed in Sec. 3.3.1, and some examples for the first form factor shells in the hexagonal lattice were given. The general form of a form factor basis in real space was introduced as a linear combination of delta functions centered at lattice positions $\mathbf{R}_b$

$$f_n(\mathbf{R}) = \sum_b g_{n,b}\, \delta(\mathbf{R} - \mathbf{R}_b)\,,$$

where the coefficients $g_{n,b}$ were only specified for the zeroth and first shell.

Here we present a more thorough prescription to build a basis up to any shell, ensuring that form factors transform according to irreducible representations of C_{6v} and that they all stay orthogonal to each other. For that matter, we will index the different shells by a single bond vector each, since it suffices to consider bond vectors in the irreducible triangular sector shown in Fig. C.1. The rest of the bonds constituting the shell can be obtained via symmetry transformations of the group, and their corresponding coefficients are shown in Fig. C.2. We will denote the representative bond vectors in Fig. C.1 by $\mathbf{R} = a_1\,\mathbf{e}_1 + a_2\,\mathbf{e}_2$, where $\mathbf{e}_1$ and $\mathbf{e}_2$ are the lattice basis vectors, and $a_1, a_2 \in \mathbb{N}$ with $a_1 \geq a_2$. Note that since we set the nearest neighbor distance of the underlying honeycomb lattice to 1, the basis vectors $\mathbf{e}_1$ and $\mathbf{e}_2$ for the hexagonal Bravais lattice have norm $\sqrt{3}$.

The form factor shells may contain up to 12 bond vectors each, and thus up to 12 different form factors, with the exceptions of shells of a representative bond vector $\mathbf{R}$ lying in a symmetry axis, which only contain 6 form factors, and the zeroth form factor shell containing only one. The general case for the coefficients of bond vectors in each representation is illustrated in Fig. C.2. Shells with a bond vector lying in a symmetry axis lack form factors of the representation A_2, and in their two dimensional E_1 and E_2 representations depicted in Fig. C.2, the first combination of bonds shown becomes equivalent to the second one, and the third becomes equivalent to the fourth. Also, if the bond vector lies at the symmetry axis defined by $a_2 = 0$, the form factor shell lacks the B_1 representation, and if it lies at the axis defined by $a_1 = a_2$, it lacks

the B_2 representation. This reduces the number of form factors in either of this cases to only 6.

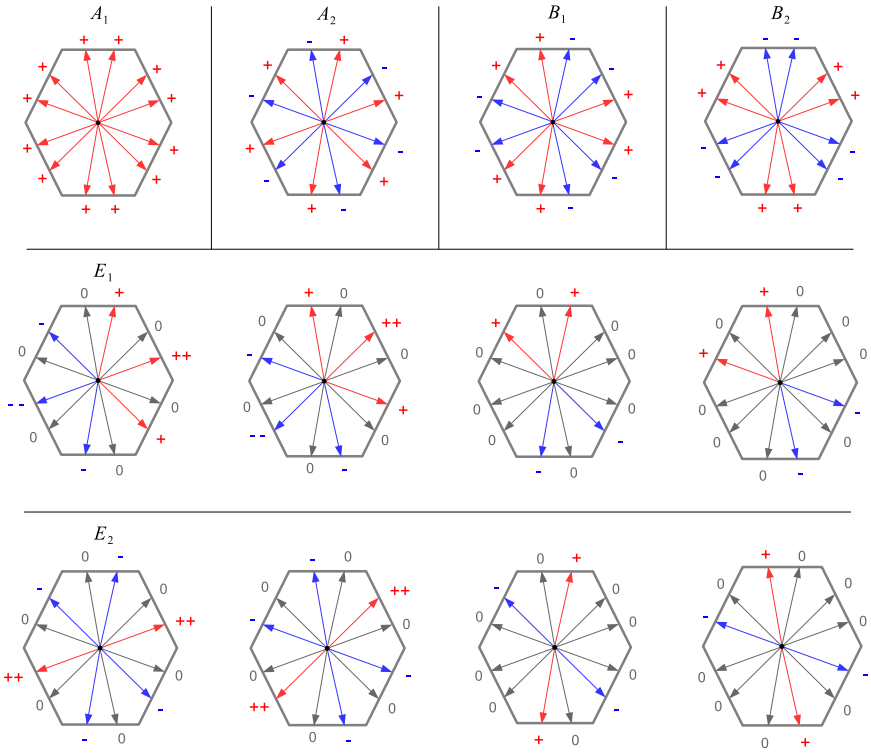

Figure C.2.: Coefficients of bond vectors for real space form factors in the basis of irreducible representations of C_{6v}. Double plus and minus signs indicate a coefficient of ± 2. These coefficients do not contain normalization factors.

In momentum space, the form factors for each representation read

$$
\begin{aligned}
A_1: \; f(\mathbf{k}) = &\cos\left(\sqrt{3}\left(a_1+\frac{a_2}{2}\right)k_x+\frac{3}{2}a_2k_y\right)+\cos\left(\sqrt{3}\left(a_2+\frac{a_1}{2}\right)k_x+\frac{3}{2}a_1k_y\right)\\
&+\cos\left(\frac{\sqrt{3}}{2}(a_1-a_2)k_x+\frac{3}{2}(a_1+a_2)k_y\right)+\cos\left(\frac{\sqrt{3}}{2}(a_2-a_1)k_x+\frac{3}{2}(a_1+a_2)k_y\right)\\
&+\cos\left(\sqrt{3}\left(a_1+\frac{a_2}{2}\right)k_x-\frac{3}{2}a_2k_y\right)+\cos\left(\sqrt{3}\left(a_2+\frac{a_1}{2}\right)k_x-\frac{3}{2}a_1k_y\right)\\
A_2: \; f(\mathbf{k}) = &\cos\left(\sqrt{3}\left(a_1+\frac{a_2}{2}\right)k_x+\frac{3}{2}a_2k_y\right)-\cos\left(\sqrt{3}\left(a_2+\frac{a_1}{2}\right)k_x+\frac{3}{2}a_1k_y\right)\\
&+\cos\left(\frac{\sqrt{3}}{2}(a_1-a_2)k_x+\frac{3}{2}(a_1+a_2)k_y\right)-\cos\left(\frac{\sqrt{3}}{2}(a_2-a_1)k_x+\frac{3}{2}(a_1+a_2)k_y\right)\\
&-\cos\left(\sqrt{3}\left(a_1+\frac{a_2}{2}\right)k_x-\frac{3}{2}a_2k_y\right)+\cos\left(\sqrt{3}\left(a_2+\frac{a_1}{2}\right)k_x-\frac{3}{2}a_1k_y\right)
\end{aligned}
$$

$$
\begin{aligned}
B_1: \; f(\mathbf{k}) = &\sin\left(\sqrt{3}\left(a_1+\frac{a_2}{2}\right)k_x+\frac{3}{2}a_2k_y\right)+\sin\left(\sqrt{3}\left(a_2+\frac{a_1}{2}\right)k_x+\frac{3}{2}a_1k_y\right)\\
&-\sin\left(\frac{\sqrt{3}}{2}(a_1-a_2)k_x+\frac{3}{2}(a_1+a_2)k_y\right)-\sin\left(\frac{\sqrt{3}}{2}(a_2-a_1)k_x+\frac{3}{2}(a_1+a_2)k_y\right)\\
&-\sin\left(\sqrt{3}\left(a_1+\frac{a_2}{2}\right)k_x-\frac{3}{2}a_2k_y\right)-\sin\left(\sqrt{3}\left(a_2+\frac{a_1}{2}\right)k_x-\frac{3}{2}a_1k_y\right)
\end{aligned}
$$

$$
\begin{aligned}
B_2: \; f(\mathbf{k}) = &\sin\left(\sqrt{3}\left(a_1+\frac{a_2}{2}\right)k_x+\frac{3}{2}a_2k_y\right)-\sin\left(\sqrt{3}\left(a_2+\frac{a_1}{2}\right)k_x+\frac{3}{2}a_1k_y\right)\\
&-\sin\left(\frac{\sqrt{3}}{2}(a_1-a_2)k_x+\frac{3}{2}(a_1+a_2)k_y\right)+\sin\left(\frac{\sqrt{3}}{2}(a_2-a_1)k_x+\frac{3}{2}(a_1+a_2)k_y\right)\\
&+\sin\left(\sqrt{3}\left(a_1+\frac{a_2}{2}\right)k_x-\frac{3}{2}a_2k_y\right)-\sin\left(\sqrt{3}\left(a_2+\frac{a_1}{2}\right)k_x-\frac{3}{2}a_1k_y\right)
\end{aligned}
$$

$$
\begin{aligned}
E_1: \; f(\mathbf{k}) = &2\sin\left(\sqrt{3}\left(a_1+\frac{a_2}{2}\right)k_x+\frac{3}{2}a_2k_y\right)+\sin\left(\frac{\sqrt{3}}{2}(a_1-a_2)k_x+\frac{3}{2}(a_1+a_2)k_y\right)\\
&+\sin\left(\sqrt{3}\left(a_2+\frac{a_1}{2}\right)k_x-\frac{3}{2}a_1k_y\right)
\end{aligned}
$$

$$
E_1': \; f(\mathbf{k}) = \sin\left(\frac{\sqrt{3}}{2}(a_1-a_2)k_x+\frac{3}{2}(a_1+a_2)k_y\right)-\sin\left(\sqrt{3}\left(a_2+\frac{a_1}{2}\right)k_x-\frac{3}{2}a_1k_y\right)
$$

$$
\begin{aligned}
E_2: \; f(\mathbf{k}) = &2\cos\left(\sqrt{3}\left(a_1+\frac{a_2}{2}\right)k_x+\frac{3}{2}a_2k_y\right)-\cos\left(\frac{\sqrt{3}}{2}(a_1-a_2)k_x+\frac{3}{2}(a_1+a_2)k_y\right)\\
&-\cos\left(\sqrt{3}\left(a_2+\frac{a_1}{2}\right)k_x-\frac{3}{2}a_1k_y\right)
\end{aligned}
$$

$$
E_2': \; f(\mathbf{k}) = \cos\left(\frac{\sqrt{3}}{2}(a_1-a_2)k_x+\frac{3}{2}(a_1+a_2)k_y\right)-\cos\left(\sqrt{3}\left(a_2+\frac{a_1}{2}\right)k_x-\frac{3}{2}a_1k_y\right)
$$

where in the two-dimensional representations, the expression corresponds to the Fourier transform of the first bond combination shown in Fig. C.2, and we denoted those corresponding to the third combination by a prime, e.g. E_1',E_2'. The second and fourth bond combinations in these representations are respectively obtained from the expressions of the first and third by swapping $a_1 \leftrightarrow a_2$. These form factors in momentum space are not normalized, except for those in E_1' and E_2'. The rest all require a prefactor $\frac{1}{\sqrt{3}}$ to be normalized if their representative bond vector does not lie at a symmetry axis. Otherwise, the surviving one-dimensional representations get a prefactor $\frac{1}{\sqrt{6}}$, since some pairs of sines and cosines above take the same argument when $a_1 = a_2$ or $a_2 = 0$ and add up together. In such cases, the absence of some representations becomes evident as they lead to a $f(\mathbf{k}) = 0$ form factor due to the mutual cancellation of those sine and cosine pairs.

D. Numerical implementation

Here we briefly review some numerical and computational aspects of our current implementation, and comment on possible future improvements. We acknowledge the use of the DCUHRE quadrature routine [8] for the numerical integration of fermionic bubbles, the ODEint library [1] for solving the TUfRG differential equations respect to the scale Ω, and the JUBE workflow environment [89] to manage our computations in the JURECA cluster.

As mentioned in Sec. 4.3 and Sec. 5.3, wavevector dependences of fermionic bubbles, bosonic propagators, and projected Vs are discretized into N_k regions in the Brillouin zone following a static grid. In its current form, one may choose different BZ meshes for particle-particle and particle-hole channels without a need for additional considerations. The channels couple via the inter-channel projections, but since they are computed in real space, the momentum space discretization of each propagator is only involved independently at their respective Fourier transforms to position space. If one were to use a different BZ mesh for the C than for the D channel, as it may be desirable when considering long-ranged Coulomb interactions, some interpolation procedure would be necessary since these two channels couple explicitly in the flow equation for the D propagator. The same is true if meshes for fermionic bubbles were to differ from those used for bosonic propagators and projected Vs, which may also be convenient since in the general case the location of their peaked structures does not necessarily coincide. Actually, the location of the relevant structures in each of these objects does evolve considerably during the flow. We made sure that our static meshes are fine enough to capture all these structures correctly, and since peaks fortunately stay at a relatively fixed position when they are at their sharpest, i.e. when approaching an instability at low energies, they can be reliably described by denser discretizations at fixed regions. However, this often requires doing some preliminary calculations to identify the location of such peaks, to be later checked for convergence with an appropriately refined mesh. Instead, the use of a dynamically adaptive mesh would avoid these issues altogether. Our current meshes are defined using a recursive procedure, starting from the irreducible triangle in the BZ and splitting it into 4 similar triangles, each of which is further split up to a given depth level depending on the region. This sort of structure is ideally suited to be stored as a quaternary tree, together with some rules determining when and where to perform additional splits to the next depth level, or to recollapse children nodes back into the previous depth level. It would not only allow to adapt the meshes dynamically along the flow, but also provide an efficient search structure in order to do interpolation, which would also be required if the grid for each object evolves separately during the flow.

The momentum space grids used for the numeric integration of fermionic bubbles are not static, but follow an adaptive procedure internally defined by DCUHRE. These are determined anew at each scale during the flow, and for each bubble component independently. Runs differing in the interaction parameters but not in the kinetic model parameters result in having to compute the same bubbles again each run. Depending on the size of the computation, and on the structure of the RG scale steps taken along the flow, it would be more convenient to pre-store the integrated fermionic bubbles. In our case, benchmarking runs aside, the dense grids used would

soon turn the problem from compute bound to memory bound, with the drawbacks that it would bring for parallel scalability. Moreover, the step size in Ω at different scales and for runs with different interaction parameters also differ substantially. Some interpolation procedure would then be required to obtain the bubble values at the desired scales. This would bring some additional inaccuracies which we would rather avoid, since the bubbles are the major agents driving the singular structure of the RG flow. Being integrated in a numerically adaptive way, the fermionic bubbles are the only objects for which we have a direct error estimation. A nice alternative to the current implementation, which has already been tested in Ref. [88], is to propagate the local error estimates for the individual bubble components to a global error estimate on the scale derivatives of bosonic propagators, following directly from the TUfRG flow equations. The adaptive integration procedure is then controlled by the global error estimate, which results in approximately ten times fewer integrand evaluations to achieve the same level of confidence as compared to using local errors, since not all bubble components have the same impact on the renormalization of bosonic propagators, and thus not every single one requires to be integrated to the same accuracy. The current implementation of this integration routine, named Parallel Adaptive Integration in two Dimensions (PAID), does not include the contribution from the projected Vs to the global error, since they have no error estimate yet. The use of an adaptive mesh would also provide such estimates.

The last aspect to discuss is the numerical solution to the Ω scale dependence of bosonic propagators, consisting on a set of coupled ordinary differential equations. This is done in a semi-adaptive fashion by means of ODEint, using a so-called explicit stepper within a multistep method. Such explicit steppers require a step size in Ω as input, and return the values for propagators at the new scale without error estimation. ODEint also provides fully adaptive methods which allow to solve Ω dependences efficiently with a minimal number of steps, but they all require the desired final value of Ω to be known a priori, since they use it as target value for error estimation. This is not well suited for approaching divergences taking place at unknown Ω values, as is done in our RG flows. Moreover, there are no adaptive multistep methods available in ODEint yet. The advantage of multistep methods like the Adams-Basforth routine used in this thesis is that they only require one evaluation of the ODE's right hand side per step, while providing a higher than first order solution. ODEint internally stores the values obtained during a number of previous steps in order to apply a Runge-Kutta solution of the desired order. Since the evaluation of the ODE's right hand side is the most time consuming part of our computation, multistep methods are very convenient. The semi-adaptive procedure employed here consists on initially using a fixed step size, usually in a range $d\Omega \sim 0.01 - 0.1\,\Omega$, and dynamically reducing it once approaching a divergence so that the maximal increments of bosonic propagators fall in a range $dB_{\max} \sim 0.1 - 1\,t$. The expected increment is just extrapolated linearly. This semi-adaptive strategy works rather well in the absence of long-ranged interactions, since the absolute values of bosonic propagators do not exceed the bandwidth until signaling an instability via divergences. Otherwise, it is preferable to adopt step sizes based on a relative increment of propagators instead of absolute ones. This can also be applied to the fixed step size used in the initial stages via the modification $d\Omega \to |\log dB_{\max}| d\Omega$ to add some adaptivity, together with some sensible bounds so that the step does not become too big if propagator increments are very small, and ensuring that $dB_{\max} < 0.1 - 1\,t$. Overall, in the current implementation, each run has to be done several times using different size steps to check for convergence.

Ultimately, it would be desirable to achieve an implementation of the TUfRG scheme which only requires to check convergence respect to the number of form-factors considered. The discussion above is meant to motivate attempts in this direction,

hopefully arriving to a procedure unifying the already available error estimates from fermionic bubbles with error estimates for bosonic propagators and projected Vs, in order to have a controlled adaptive mesh and adaptive step size in the RG scale.

On a separate note, there are two other aspects that might need improvement if the implementation is to remain scalable at even bigger problem sizes. On the one hand, the matrix multiplication in the contraction of form-factor and band indices at the ODE's right hand side has so far been straightforwardly implemented. Being done in parallel, it accounts for a small part of the total computation time. However, a possible future bottleneck would require using more elaborate routines from algebraic libraries. On the other hand, ODEint has recently included the possibility of exploiting parallelism in its internal computations, which also remain negligible for the problem sizes analyzed in this work, but could eventually become another bottleneck.

Acknowledgements

I owe my sincere gratitude to the many people who supported me during my doctoral studies, both on a professional and personal level.

First and foremost, I would like to thank Prof. Carsten Honerkamp for supervising me as a graduate student, and for giving me the opportunity to attend many interesting conferences and workshops. This research project was only made possible due to his inspirational advice and dedication. I would also like to express my gratitude and admiration for his understanding and support during times of hardship and struggle, and for his openness to welcome my own ideas.

I sincerely thank Dr. Michael Scherer for our stimulating collaboration and for taking the role of second referee of this dissertation.

I gladly acknowledge all my coworkers during these years, from undergraduates to professors and other university staff, for the great atmosphere and fruitful discussions. Special thanks go to Julian Lichtenstein and Timo Reckling, with whom I shared my office and closely collaborated in research projects. The time spent at the institute would not have been the same without them. I would also like to thank Dr. Stefan Maier for his insight, leading to the development of the TUfRG scheme.

My thanks are also due to Dr. Daniel Rohe and Dr. Edoardo di Napoli for their collaboration and assistance on the computational aspects of this work.

Finally, my friends and family also deserve my gratitude for all their personal support during these years.

The German Research Foundation (DFG) is acknowledged for financial support via FOR 723, FOR 912, SPP 1459, and RTG 1995. The author gratefully acknowledges the computing time granted by the JARA-HPC Vergabegremium on the supercomputer JURECA at Forschungszentrum Jülich.

List of publications

Large parts of this thesis have already been published in the following journal articles

- J. Lichtenstein, D. Sánchez de la Peña, D. Rohe, E. D. Napoli, C. Honerkamp, and S. Maier, "High-performance functional renormalization group calculations for interacting fermions", *Computer Physics Communications*, pp. -, 2016.
- D. Sánchez de la Peña, J. Lichtenstein, and C. Honerkamp, "Competing electronic instabilities of extended Hubbard models on the honeycomb lattice: A functional renormalization group calculation with high-wave-vector resolution", *Phys. Rev. B*, vol. 95, p. 085143, Feb 2017.
- D. Sánchez de la Peña, J. Lichtenstein, C. Honerkamp, and M. M. Scherer, "Antiferromagnetism and competing charge instabilities of electrons in strained graphene from coulomb interactions", *Phys. Rev. B*, vol. 96, p. 205155, Nov 2017.

Further articles which are not explicitly part of this thesis are shown below

- D. Sánchez de la Peña, M. M. Scherer, and C. Honerkamp, "Electronic instabilities of the AA-honeycomb bilayer", *Annalen der Physik*, vol. 526, no. 9-10, pp. 366-371, 2014.
- J. Lichtenstein, J. Winkelmann, D. Sánchez de la Peña, T. Vidović, and E. Di Napoli, "Parallel adaptive integration in high-performance functional renormalization group computations", *High-Performance Scientific Computing*, pp. 170-184, Springer International Publishing, 2017.

References

[1] K. Ahnert and M. Mulansky, "Odeint – solving ordinary differential equations in c++," *AIP Conference Proceedings*, vol. 1389, no. 1, pp. 1586–1589, 2011.

[2] S. Andergassen, V. Meden, H. Schoeller, J. Splettstoesser, and M. R. Wegewijs, "TOPICAL REVIEW: Charge transport through single molecules, quantum dots and quantum wires," *Nanotechnology*, vol. 21, p. 272001, July 2010.

[3] P. W. Anderson, "More is different," *Science*, vol. 177, no. 4047, pp. 393–396, 1972.

[4] P. W. Anderson, "Twenty-five Years of High-Temperature Superconductivity - A Personal Review," *Journal of Physics: Conference Series*, vol. 449, no. 1, p. 012001, 2013.

[5] F. F. Assaad and I. F. Herbut, "Pinning the Order: The Nature of Quantum Criticality in the Hubbard Model on Honeycomb Lattice," *Phys. Rev. X*, vol. 3, p. 031010, Aug 2013.

[6] A. Avella and F. Mancini, *Strongly Correlated Systems: Theoretical Methods*. Springer Series in Solid-State Sciences, Springer Berlin Heidelberg, 2011.

[7] B. A. Bernevig and S.-C. Zhang, "Quantum Spin Hall Effect," *Phys. Rev. Lett.*, vol. 96, p. 106802, Mar 2006.

[8] J. Berntsen, T. O. Espelid, and A. Genz, "Algorithm 698: Dcuhre: An adaptive multidemensional integration routine for a vector of integrals," *ACM Trans. Math. Softw.*, vol. 17, pp. 452–456, Dec. 1991.

[9] A. M. Black-Schaffer and S. Doniach, "Resonating valence bonds and mean-field d-wave superconductivity in graphite," *Phys. Rev. B*, vol. 75, p. 134512, Apr 2007.

[10] L. Boehnke, H. Hafermann, M. Ferrero, F. Lechermann, and O. Parcollet, "Orthogonal polynomial representation of imaginary-time Green's functions," *Phys. Rev. B*, vol. 84, p. 075145, Aug 2011.

[11] I. Bose, "Quantum magnets: a brief overview," *eprint arXiv:cond-mat/0107399*, July 2001.

[12] P. Buividovich, D. Smith, M. Ulybyshev, and L. von Smekal, "Competing order in the fermionic Hubbard model on the hexagonal graphene lattice," *PoS*, vol. LATTICE2016, p. 244, 2016.

[13] R. J. Bursill, C. Castleton, and W. Barford, "Optimal parametrisation of the Pariser-Parr-Pople Model for benzene and biphenyl," *Chemical Physics Letters*, vol. 294, no. 4–5, pp. 305 – 313, 1998.

[14] S. Capponi and A. M. Läuchli, "Phase diagram of interacting spinless fermions on the honeycomb lattice: A comprehensive exact diagonalization study," *Phys. Rev. B*, vol. 92, p. 085146, Aug. 2015.

[15] A. H. Castro Neto, F. Guinea, N. M. R. Peres, K. S. Novoselov, and A. K. Geim, "The electronic properties of graphene," *Reviews of Modern Physics*, vol. 81, pp. 109–162, 2009.

[16] L. Classen, M. M. Scherer, and C. Honerkamp, "Instabilities on graphene's honeycomb lattice with electron-phonon interactions," *Phys. Rev. B*, vol. 90, p. 035122, July 2014.

[17] L. Classen, I. F. Herbut, L. Janssen, and M. M. Scherer, "Mott multicriticality of Dirac electrons in graphene," *Phys. Rev. B*, vol. 92, p. 035429, Jul 2015.

[18] L. Classen, I. F. Herbut, L. Janssen, and M. M. Scherer, "Competition of density waves and quantum multicritical behavior in Dirac materials from functional renormalization," *Phys. Rev. B*, vol. 93, p. 125119, Mar 2016.

[19] C.-K. Chiu, J. C. Y. Teo, A. P. Schnyder, and S. Ryu, "Classification of topological quantum matter with symmetries," *Rev. Mod. Phys.*, vol. 88, p. 035005, Aug 2016.

[20] M. Daghofer and M. Hohenadler, "Phases of correlated spinless fermions on the honeycomb lattice," *Phys. Rev. B*, vol. 89, p. 035103, Jan 2014.

[21] S. Das Sarma, S. Adam, E. H. Hwang, and E. Rossi, "Electronic transport in two-dimensional graphene," *Rev. Mod. Phys.*, vol. 83, pp. 407–470, May 2011.

[22] S. Diehl, S. Floerchinger, H. Gies, J. M. Pawlowkski, and C. Wetterich, "Functional renormalization group approach to the BCS-BEC crossover," *Annalen der Physik*, vol. 522, pp. 615–656, Sept. 2010.

[23] T. DJuric, N. Chancellor, and I. F. Herbut, "Interaction-induced anomalous quantum Hall state on the honeycomb lattice," *Phys. Rev. B*, vol. 89, p. 165123, Apr 2014.

[24] A. Eberlein and W. Metzner, "Parametrization of Nambu Vertex in a Singlet Superconductor," *Progress of Theoretical Physics*, vol. 124, no. 3, pp. 471–491, 2010.

[25] A. Eberlein and W. Metzner, "Effective interactions and fluctuation effects in spin-singlet superfluids," *Phys. Rev. B*, vol. 87, p. 174523, May 2013.

[26] A. Eberlein, "Fermionic two-loop functional renormalization group for correlated fermions: Method and application to the attractive Hubbard model," *Phys. Rev. B*, vol. 90, p. 115125, Sept. 2014.

[27] A. Eberlein and W. Metzner, "Superconductivity in the two-dimensional t-t$'$-Hubbard model," *Phys. Rev. B*, vol. 89, p. 035126, Jan. 2014.

[28] G. Editors, L. H. Greene, J. Thompson, and J. Schmalian, "Strongly correlated electron systems - reports on the progress of the field," *Reports on Progress in Physics*, vol. 80, no. 3, p. 030401, 2017.

[29] D. C. Elias, R. V. Gorbachev, A. S. Mayorov, S. V. Morozov, A. A. Zhukov, P. Blake, L. A. Ponomarenko, I. V. Grigorieva, K. S. Novoselov, F. Guinea, and A. K. Geim, "Dirac cones reshaped by interaction effects in suspended graphene," *Nature Physics*, vol. 7, pp. 701–704, Sept. 2011.

[30] P. Fulde, P. Thalmeier, and G. Zwicknagl, "Strongly correlated electrons," *eprint arXiv:cond-mat/0607165*, July 2006.

[31] O. V. Gamayun, E. V. Gorbar, and V. P. Gusynin, "Supercritical coulomb

center and excitonic instability in graphene," *Phys. Rev. B*, vol. 80, p. 165429, Oct 2009.

[32] O. V. Gamayun, E. V. Gorbar, and V. P. Gusynin, "Gap generation and semimetal-insulator phase transition in graphene," *Phys. Rev. B*, vol. 81, p. 075429, Feb 2010.

[33] N. A. García-Martínez, A. G. Grushin, T. Neupert, B. Valenzuela, and E. V. Castro, "Interaction-driven phases in the half-filled spinless honeycomb lattice from exact diagonalization," *Phys. Rev. B*, vol. 88, p. 245123, Dec 2013.

[34] A. K. Geim and K. S. Novoselov, "The rise of graphene," *Nat. Mater*, vol. 183, Feb. 2007.

[35] R. Gersch, C. Honerkamp, D. Rohe, and W. Metzner, "Fermionic renormalization group flow into phases with broken discrete symmetry: charge-density wave mean-field model," *The European Physical Journal B - Condensed Matter and Complex Systems*, vol. 48, pp. 349–358, Dec 2005.

[36] R. Gersch, C. Honerkamp, and W. Metzner, "Superconductivity in the attractive hubbard model: functional renormalization group analysis," *New Journal of Physics*, vol. 10, no. 4, p. 045003, 2008.

[37] K.-U. Giering and M. Salmhofer, "Self-energy flows in the two-dimensional repulsive Hubbard model," *Phys. Rev. B*, vol. 86, p. 245122, Dec. 2012.

[38] M. Golor, T. Reckling, L. Classen, M. M. Scherer, and S. Wessel, "Ground-state phase diagram of the half-filled bilayer Hubbard model," *Phys. Rev. B*, vol. 90, p. 195131, Nov. 2014.

[39] M. Golor and S. Wessel, "Nonlocal density interactions in auxiliary-field quantum Monte Carlo simulations: Application to the square lattice bilayer and honeycomb lattice," *Phys. Rev. B*, vol. 92, p. 195154, Nov. 2015.

[40] J. González, F. Guinea, and M. Vozmediano, "Non-fermi liquid behavior of electrons in the half-filled honeycomb lattice (a renormalization group approach)," *Nuclear Physics B*, vol. 424, no. 3, pp. 595 – 618, 1994.

[41] J. González, F. Guinea, and M. A. H. Vozmediano, "Unconventional quasiparticle lifetime in graphite," *Phys. Rev. Lett.*, vol. 77, pp. 3589–3592, Oct 1996.

[42] E. V. Gorbar, V. P. Gusynin, V. A. Miransky, and I. A. Shovkovy, "Magnetic field driven metal-insulator phase transition in planar systems," *Phys. Rev. B*, vol. 66, p. 045108, Jul 2002.

[43] A. G. Grushin, E. V. Castro, A. Cortijo, F. de Juan, M. A. H. Vozmediano, and B. Valenzuela, "Charge instabilities and topological phases in the extended Hubbard model on the honeycomb lattice with enlarged unit cell," *Phys. Rev. B*, vol. 87, p. 085136, Feb 2013.

[44] C. Gutierrez, C.-J. Kim, L. Brown, T. Schiros, D. Nordlund, E. B. Lochocki, K. M. Shen, J. Park, and A. N. Pasupathy, "Imaging chiral symmetry breaking from kekulé bond order in graphene," *Nat Phys*, vol. advance online publication, May 2016. Article.

[45] C. J. Halboth and W. Metzner, "d-Wave Superconductivity and Pomeranchuk Instability in the Two-Dimensional Hubbard Model," *Phys. Rev. Lett.*, vol. 85, pp. 5162–5165, Dec 2000.

[46] F. D. M. Haldane, "Model for a Quantum Hall Effect without Landau Lev-

els: Condensed-Matter Realization of the "Parity Anomaly"," *Phys. Rev. Lett.*, vol. 61, pp. 2015–2018, Oct 1988.

[47] P. Hansmann, T. Ayral, L. Vaugier, P. Werner, and S. Biermann, "Long-Range Coulomb Interactions in Surface Systems: A First-Principles Description within Self-Consistently Combined *GW* and Dynamical Mean-Field Theory," *Phys. Rev. Lett.*, vol. 110, p. 166401, Apr 2013.

[48] I. F. Herbut, "Interactions and Phase Transitions on Graphene's Honeycomb Lattice," *Physical Review Letters*, vol. 97, p. 146401, Oct. 2006.

[49] I. F. Herbut, V. Juričić, and O. Vafek, "Relativistic Mott criticality in graphene," *Phys. Rev. B*, vol. 80, p. 075432, Aug 2009.

[50] I. F. Herbut, V. Juričić, and B. Roy, "Theory of interacting electrons on the honeycomb lattice," *Phys. Rev. B*, vol. 79, p. 085116, Feb 2009.

[51] M. Hohenadler, F. Parisen Toldin, I. F. Herbut, and F. F. Assaad, "Phase diagram of the Kane-Mele-Coulomb model," *Phys. Rev. B*, vol. 90, p. 085146, Aug. 2014.

[52] M. Bercx, M. Hohenadler, and F. F. Assaad, "Kane-Mele-Hubbard model on the π-flux honeycomb lattice," *Phys. Rev. B*, vol. 90, p. 075140, Aug 2014.

[53] C. Honerkamp, M. Salmhofer, N. Furukawa, and T. M. Rice, "Breakdown of the Landau-Fermi liquid in two dimensions due to umklapp scattering," *Phys. Rev. B*, vol. 63, p. 035109, Jan 2001.

[54] C. Honerkamp and M. Salmhofer, "Flow of the quasiparticle weight in the n-patch renormalization group scheme," *Phys. Rev. B*, vol. 67, p. 174504, May 2003.

[55] C. Honerkamp, "Density Waves and Cooper Pairing on the Honeycomb Lattice," *Phys. Rev. Lett.*, vol. 100, p. 146404, Apr 2008.

[56] C. Honerkamp, "Iron pncitide superconductors studied by the functional renormalization group," *The European Physical Journal Special Topics*, vol. 188, pp. 33–47, Oct 2010.

[57] C. Honerkamp, "Selfenergy Effect on the Magnetic Ordering Transition in the Mono- and Bilayer Honeycomb Hubbard Model," *Annalen der Physik*, pp. 1700044–n/a, 2017. 1700044.

[58] C. Honerkamp, "Influence of hopping selfenergy and quasiparticle degradation on the antiferromagnetic ordering in the bilayer honeycomb Hubbard model," *ArXiv e-prints*, Oct. 2017.

[59] R. Hott, R. Kleiner, T. Wolf, and G. Zwicknagl, "Review on Superconducting Materials," *ArXiv e-prints*, June 2013.

[60] C.-Y. Hou, C. Chamon, and C. Mudry, "Electron fractionalization in two-dimensional graphenelike structures," *Phys. Rev. Lett.*, vol. 98, p. 186809, May 2007.

[61] C. Husemann and M. Salmhofer, "Efficient parametrization of the vertex function, Ω scheme, and the t, t' Hubbard model at van Hove filling," *Phys. Rev. B*, vol. 79, p. 195125, May 2009.

[62] C. Husemann, K.-U. Giering, and M. Salmhofer, "Frequency-dependent vertex functions of the (t, t') Hubbard model at weak coupling," *Phys. Rev. B*, vol. 85,

p. 075121, Feb 2012.

[63] E. H. Hwang and S. Das Sarma, "Dielectric function, screening, and plasmons in two-dimensional graphene," *Phys. Rev. B*, vol. 75, p. 205418, May 2007.

[64] S. G. Jakobs, V. Meden, and H. Schoeller, "Nonequilibrium Functional Renormalization Group for Interacting Quantum Systems," *Physical Review Letters*, vol. 99, p. 150603, Oct. 2007.

[65] Y. Jia, H. Guo, Z. Chen, S.-Q. Shen, and S. Feng, "Effect of interactions on two-dimensional Dirac fermions," *Phys. Rev. B*, vol. 88, p. 075101, Aug. 2013.

[66] J. Jung and A. H. MacDonald, "Enhancement of nonlocal exchange near isolated band crossings in graphene," *Phys. Rev. B*, vol. 84, p. 085446, Aug 2011.

[67] L. P. Kadanoff, "Scaling laws for Ising models near T(c)," *Physics*, vol. 2, pp. 263–272, 1966.

[68] J. Kanamori, "Electron correlation and ferromagnetism of transition metals," *Progress of Theoretical Physics*, vol. 30, no. 3, pp. 275–289, 1963.

[69] C. L. Kane and E. J. Mele, "Quantum Spin Hall Effect in Graphene," *Phys. Rev. Lett.*, vol. 95, p. 226801, Nov 2005.

[70] C. Karrasch, R. Hedden, R. Peters, T. Pruschke, K. Schönhammer, and V. Meden, "A finite-frequency functional renormalization group approach to the single impurity Anderson model," *Journal of Physics: Condensed Matter*, vol. 20, no. 34, p. 345205, 2008.

[71] A. P. Kampf and A. A. Katanin, "Competing phases in the extended $U-V-J$ Hubbard model near the Van Hove fillings," *Phys. Rev. B*, vol. 67, p. 125104, Mar 2003.

[72] A. A. Katanin, "Fulfillment of Ward identities in the functional renormalization group approach," *Phys. Rev. B*, vol. 70, p. 115109, Sept. 2004.

[73] A. A. Katanin and A. P. Kampf, "Quasiparticle anisotropy and pseudogap formation from the weak-coupling renormalization group point of view," *Phys. Rev. Lett.*, vol. 93, p. 106406, Sep 2004.

[74] A. A. Katanin, "Two-loop functional renormalization group approach to the one- and two-dimensional hubbard model," *Phys. Rev. B*, vol. 79, p. 235119, Jun 2009.

[75] M. I. Katsnelson, K. S. Novoselov, and A. K. Geim, "Chiral tunnelling and the Klein paradox in graphene," *Nature Physics*, vol. 2, pp. 620–625, Sept. 2006.

[76] M. Kharitonov, "Phase diagram for the $\nu = 0$ quantum Hall state in monolayer graphene," *Phys. Rev. B*, vol. 85, p. 155439, Apr 2012.

[77] D. V. Khveshchenko, "Ghost excitonic insulator transition in layered graphite," *Phys. Rev. Lett.*, vol. 87, p. 246802, Nov 2001.

[78] M. L. Kiesel, C. Platt, W. Hanke, D. A. Abanin, and R. Thomale, "Competing many-body instabilities and unconventional superconductivity in graphene," *Phys. Rev. B*, vol. 86, p. 020507, Jul 2012.

[79] M. L. Kiesel, C. Platt, and R. Thomale, "Unconventional Fermi Surface Instabilities in the Kagome Hubbard Model," *Physical Review Letters*, vol. 110, p. 126405, Mar. 2013.

[80] P. Kopietz, L. Bartosch, and F. Schütz, *Introduction to the Functional Renormalization Group*. Lecture Notes in Physics, Springer Berlin Heidelberg, 2010.

[81] V. N. Kotov, B. Uchoa, V. M. Pereira, F. Guinea, and A. H. Castro Neto, "Electron-electron interactions in graphene: Current status and perspectives," *Rev. Mod. Phys.*, vol. 84, pp. 1067–1125, Jul 2012.

[82] F. B. Kugler and J. von Delft, "Multiloop functional renormalization group for general models," *ArXiv e-prints*, July 2017.

[83] C. P. Landee and M. M. Turnbull, "Review: A gentle introduction to magnetism: units, fields, theory, and experiment," *Journal of Coordination Chemistry*, vol. 67, no. 3, pp. 375–439, 2014.

[84] T. C. Lang, Z. Y. Meng, M. M. Scherer, S. Uebelacker, F. F. Assaad, A. Muramatsu, C. Honerkamp, and S. Wessel, "Antiferromagnetism in the Hubbard Model on the Bernal-Stacked Honeycomb Bilayer," *Physical Review Letters*, vol. 109, p. 126402, Sept. 2012.

[85] Z.-X. Li, Y.-F. Jiang, S.-K. Jian, and H. Yao, "Fermion-induced quantum critical points: type-II Landau-forbidden transitions," *arXiv:1512.07908*, Dec. 2015.

[86] J. Lichtenstein, S. A. Maier, C. Honerkamp, C. Platt, R. Thomale, O. K. Andersen, and L. Boeri, "Functional renormalization group study of an eight-band model for the iron arsenides," *Phys. Rev. B*, vol. 89, p. 214514, Jun 2014.

[87] J. Lichtenstein, D. S. de la Peña, D. Rohe, E. D. Napoli, C. Honerkamp, and S. Maier, "High-performance functional renormalization group calculations for interacting fermions," *Computer Physics Communications*, pp. –, 2016.

[88] J. Lichtenstein, J. Winkelmann, D. Sánchez de la Peña, T. Vidović, and E. Di Napoli, "Parallel adaptive integration in high-performance functional renormalization group computations," in *High-Performance Scientific Computing* (E. Di Napoli, M.-A. Hermanns, H. Iliev, A. Lintermann, and A. Peyser, eds.), (Cham), pp. 170–184, Springer International Publishing, 2017.

[89] S. Luehrs, D. Rohe, A. Schnurpfeil, K. Thust, and W. Frings, "Flexible and generic workflow management," *Advances in Parallel Computing*, vol. 27, no. Parallel Computing: On the Road to Exascale, p. 431–438, 2016.

[90] S. A. Maier, C. Honerkamp, and Q.-H. Wang, "Interplay between Point-Group Symmetries and the Choice of the Bloch Basis in Multiband Models," *Symmetry*, vol. 4, p. 313, Oct. 2013.

[91] S. A. Maier, A. Eberlein, and C. Honerkamp, "Functional renormalization group for commensurate antiferromagnets: Beyond the mean-field picture," *Phys. Rev. B*, vol. 90, p. 035140, July 2014.

[92] N. Majlis, *Low Dimensional Magnetism*, pp. 443–451. Berlin, Heidelberg: Springer Berlin Heidelberg, 1991.

[93] A. S. Mayorov, D. C. Elias, I. S. Mukhin, S. V. Morozov, L. A. Ponomarenko, K. S. Novoselov, A. K. Geim, and R. V. Gorbachev, "How Close Can One Approach the Dirac Point in Graphene Experimentally?," *Nano Letters*, vol. 12, pp. 4629–4634, Sept. 2012.

[94] V. Meden, S. Andergassen, T. Enss, H. Schoeller, and K. Schönhammer, "Fermionic renormalization group methods for transport through inhomogeneous Luttinger liquids," *New Journal of Physics*, vol. 10, no. 4, p. 045012,

2008.

[95] Z. Y. Meng, T. C. Lang, S. Wessel, F. F. Assaad, and A. Muramatsu, "Quantum spin liquid emerging in two-dimensional correlated Dirac fermions," *Nature*, vol. 464, pp. 847–851, Apr. 2010.

[96] W. Metzner and D. Vollhardt, "Correlated lattice fermions in $d = \infty$ dimensions," *Phys. Rev. Lett.*, vol. 62, pp. 324–327, Jan 1989.

[97] W. Metzner, M. Salmhofer, C. Honerkamp, V. Meden, and K. Schönhammer, "Functional renormalization group approach to correlated fermion systems," *Rev. Mod. Phys.*, vol. 84, pp. 299–352, Mar 2012.

[98] T. R. Morris, "Derivative expansion of the exact renormalization group," *Physics Letters B*, vol. 329, pp. 241–248, June 1994.

[99] J. Motruk, A. G. Grushin, F. de Juan, and F. Pollmann, "Interaction-driven phases in the half-filled honeycomb lattice: An infinite density matrix renormalization group study," *Phys. Rev. B*, vol. 92, p. 085147, Aug. 2015.

[100] M. Neek-Amal, L. Covaci, K. Shakouri, and F. M. Peeters, "Electronic structure of a hexagonal graphene flake subjected to triaxial stress," *Phys. Rev. B*, vol. 88, p. 115428, Sep 2013.

[101] J. Negele and H. Orland, *Quantum many-particle systems*. Frontiers in physics, Addison-Wesley Pub. Co., 1988.

[102] K. Nomura, S. Ryu, and D.-H. Lee, "Field-induced kosterlitz-thouless transition in the $n = 0$ landau level of graphene," *Phys. Rev. Lett.*, vol. 103, p. 216801, Nov 2009.

[103] K. S. Novoselov, A. K. Geim, S. V. Morozov, D. Jiang, M. I. Katsnelson, I. V. Grigorieva, S. V. Dubonos, and A. A. Firsov, "Two-dimensional gas of massless Dirac fermions in graphene," *Nature*, vol. 438, pp. 197–200, Nov 2005.

[104] K. Ohno, "Some remarks on the Pariser-Parr-Pople method," *Theoretica chimica acta*, vol. 2, no. 3, pp. 219–227, 1964.

[105] Y. Otsuka, S. Yunoki, and S. Sorella, "Universal Quantum Criticality in the Metal-Insulator Transition of Two-Dimensional Interacting Dirac Electrons," *Phys. Rev. X*, vol. 6, p. 011029, Mar 2016.

[106] V. M. Pereira, A. H. Castro Neto, and N. M. R. Peres, "Tight-binding approach to uniaxial strain in graphene," *Phys. Rev. B*, vol. 80, p. 045401, Jul 2009.

[107] C. Platt, R. Thomale, C. Honerkamp, S.-C. Zhang, and W. Hanke, "Mechanism for a pairing state with time-reversal symmetry breaking in iron-based superconductors," *Phys. Rev. B*, vol. 85, p. 180502, May 2012.

[108] C. Platt, W. Hanke, and R. Thomale, "Functional renormalization group for multi-orbital Fermi surface instabilities," *Advances in Physics*, vol. 62, pp. 453–562, Nov. 2013.

[109] J. Polchinski, "Renormalization and Effective Lagrangians," *Nucl. Phys.*, vol. B231, pp. 269–295, 1984.

[110] S. Pujari, T. C. Lang, G. Murthy, and R. K. Kaul, "Interaction-Induced Dirac Fermions from Quadratic Band Touching in Bilayer Graphene," *Physical Review Letters*, vol. 117, p. 086404, Aug. 2016.

[111] X.-L. Qi and S.-C. Zhang, "Topological insulators and superconductors," *Rev.*

Mod. Phys., vol. 83, pp. 1057–1110, Oct 2011.

[112] S. Raghu, X.-L. Qi, C. Honerkamp, and S.-C. Zhang, "Topological Mott Insulators," *Phys. Rev. Lett.*, vol. 100, p. 156401, Apr 2008.

[113] S. Reich, J. Maultzsch, C. Thomsen, and P. Ordejón, "Tight-binding description of graphene," *Phys. Rev. B*, vol. 66, p. 035412, Jul 2002.

[114] J. Reiss, D. Rohe, and W. Metzner, "Renormalized mean-field analysis of antiferromagnetism and d-wave superconductivity in the two-dimensional Hubbard model," *Phys. Rev. B*, vol. 75, p. 075110, Feb 2007.

[115] J. Reuther and P. Wölfle, "J_1-J_2," *Phys. Rev. B*, vol. 81, p. 144410, Apr 2010.

[116] J. Reuther and R. Thomale, "Functional renormalization group for the anisotropic triangular antiferromagnet," *Phys. Rev. B*, vol. 83, p. 024402, Jan 2011.

[117] D. Rohe and W. Metzner, "Pseudogap at hot spots in the two-dimensional hubbard model at weak coupling," *Phys. Rev. B*, vol. 71, p. 115116, Mar 2005.

[118] B. Roy and I. F. Herbut, "Unconventional superconductivity on honeycomb lattice: Theory of kekule order parameter," *Phys. Rev. B*, vol. 82, p. 035429, Jul 2010.

[119] B. Roy, V. Juričić, and I. F. Herbut, "Quantum superconducting criticality in graphene and topological insulators," *Phys. Rev. B*, vol. 87, p. 041401, Jan 2013.

[120] S. Ryu, C. Mudry, C.-Y. Hou, and C. Chamon, "Masses in graphenelike two-dimensional electronic systems: Topological defects in order parameters and their fractional exchange statistics," *Phys. Rev. B*, vol. 80, p. 205319, Nov 2009.

[121] M. Salmhofer and C. Honerkamp, "Fermionic Renormalization Group Flows: Technique and Theory," *Progress of Theoretical Physics*, vol. 105, no. 1, pp. 1–35, 2001.

[122] D. Sánchez de la Peña, M. M. Scherer, and C. Honerkamp, "Electronic instabilities of the AA-honeycomb bilayer," *Annalen der Physik*, vol. 526, no. 9-10, pp. 366–371, 2014.

[123] D. S. de la Peña, J. Lichtenstein, and C. Honerkamp, "Competing electronic instabilities of extended Hubbard models on the honeycomb lattice: A functional renormalization group calculation with high-wave-vector resolution," *Phys. Rev. B*, vol. 95, p. 085143, Feb 2017.

[124] D. S. de la Peña, J. Lichtenstein, C. Honerkamp, and M. M. Scherer, "Antiferromagnetism and competing charge instabilities of electrons in strained graphene from coulomb interactions," *Phys. Rev. B*, vol. 96, p. 205155, Nov 2017.

[125] T. Sato, M. Hohenadler, and F. F. Assaad, "Dirac Fermions with Competing Orders: Non-Landau Transition with Emergent Symmetry," *Phys. Rev. Lett.*, vol. 119, p. 197203, Nov 2017.

[126] M. M. Scherer, S. Uebelacker, and C. Honerkamp, "Instabilities of interacting electrons on the honeycomb bilayer," *Phys. Rev. B*, vol. 85, p. 235408, Jun 2012.

[127] M. M. Scherer, S. Uebelacker, D. D. Scherer, and C. Honerkamp, "Interacting electrons on trilayer honeycomb lattices," *Phys. Rev. B*, vol. 86, p. 155415, Oct 2012.

[128] D. D. Scherer, M. M. Scherer, G. Khaliullin, C. Honerkamp, and B. Rosenow,

"Unconventional pairing and electronic dimerization instabilities in the doped Kitaev-Heisenberg model," *Phys. Rev. B*, vol. 90, p. 045135, July 2014.

[129] D. D. Scherer, M. M. Scherer, and C. Honerkamp, "Correlated spinless fermions on the honeycomb lattice revisited," *Phys. Rev. B*, vol. 92, p. 155137, Oct. 2015.

[130] M. M. Scherer and I. F. Herbut, "Gauge-field-assisted Kekulé quantum criticality," *Phys. Rev. B*, vol. 94, p. 205136, Nov 2016.

[131] G. Â. A. Â. H. Schober, K.-U. Giering, M. Â. M. Scherer, C. Honerkamp, and M. Salmhofer, "Functional renormalization and mean-field approach to multiband systems with spin-orbit coupling: Application to the Rashba model with attractive interaction," *Phys. Rev. B*, vol. 93, p. 115111, Mar. 2016.

[132] G. A. H. Schober, J. Ehrlich, T. Reckling, and C. Honerkamp, "Truncated unity functional renormalization group for multiband systems with spin-orbit coupling," *ArXiv e-prints*, Oct. 2017.

[133] M. Schüler, M. Rösner, T. O. Wehling, A. I. Lichtenstein, and M. I. Katsnelson, "Optimal Hubbard Models for Materials with Nonlocal Coulomb Interactions: Graphene, Silicene, and Benzene," *Phys. Rev. Lett.*, vol. 111, p. 036601, Jul 2013.

[134] D. Smith and L. von Smekal, "Monte Carlo simulation of the tight-binding model of graphene with partially screened Coulomb interactions," *Phys. Rev. B*, vol. 89, p. 195429, May 2014.

[135] S. Sorella and E. Tosatti, "Semi-metal-insulator transition of the Hubbard model in the honeycomb lattice," *EPL (Europhysics Letters)*, vol. 19, p. 699, Aug. 1992.

[136] S. Sorella, Y. Otsuka, and S. Yunoki, "Absence of a Spin Liquid Phase in the Hubbard Model on the Honeycomb Lattice," *Scientific Reports*, vol. 2, p. 992, Dec. 2012.

[137] P. Strack, R. Gersch, and W. Metzner, "Renormalization group flow for fermionic superfluids at zero temperature," *Phys. Rev. B*, vol. 78, p. 014522, Jul 2008.

[138] H.-K. Tang, E. Laksono, J. N. B. Rodrigues, P. Sengupta, F. F. Assaad, and S. Adam, "Interaction-Driven Metal-Insulator Transition in Strained Graphene," *Physical Review Letters*, vol. 115, p. 186602, Oct. 2015.

[139] R. Thomale, C. Platt, J. Hu, C. Honerkamp, and B. A. Bernevig, "Functional renormalization-group study of the doping dependence of pairing symmetry in the iron pnictide superconductors," *Phys. Rev. B*, vol. 80, p. 180505, Nov 2009.

[140] B. Uchoa and A. H. Castro Neto, "Superconducting States of Pure and Doped Graphene," *Physical Review Letters*, vol. 98, p. 146801, Apr. 2007.

[141] S. Uebelacker and C. Honerkamp, "Instabilities of quadratic band crossing points," *Phys Rev B*, vol. 84, p. 205122, Nov. 2011.

[142] S. Uebelacker and C. Honerkamp, "Multiband effects on superconducting instabilities driven by electron-electron interactions," *Phys Rev B*, vol. 85, p. 155122, Apr. 2012.

[143] S. Uebelacker and C. Honerkamp, "Self-energy feedback and frequency-dependent interactions in the functional renormalization group flow for the two-dimensional Hubbard model," *Phys. Rev. B*, vol. 86, p. 235140, Dec. 2012.

[144] M. V. Ulybyshev, P. V. Buividovich, M. I. Katsnelson, and M. I. Polikarpov, "Monte Carlo Study of the Semimetal-Insulator Phase Transition in Monolayer Graphene with a Realistic Interelectron Interaction Potential," *Physical Review Letters*, vol. 111, p. 056801, Aug. 2013.

[145] O. Vafek, "Anomalous Thermodynamics of Coulomb-Interacting Massless Dirac Fermions in Two Spatial Dimensions," *Phys. Rev. Lett.*, vol. 98, p. 216401, May 2007.

[146] J. A. Vergés, E. SanFabián, G. Chiappe, and E. Louis, "Fit of Pariser-Parr-Pople and Hubbard model Hamiltonians to charge and spin states of polycyclic aromatic hydrocarbons," *Phys. Rev. B*, vol. 81, p. 085120, Feb 2010.

[147] D. Vilardi, C. Taranto, and W. Metzner, "Non-separable frequency dependence of two-particle vertex in interacting fermion systems," *ArXiv e-prints*, Aug. 2017.

[148] D. Vollhardt, K. Byczuk, and M. Kollar, *Dynamical Mean-Field Theory*, pp. 203–236. Berlin, Heidelberg: Springer Berlin Heidelberg, 2012.

[149] Y. Volpez, D. D. Scherer, and M. M. Scherer, "Electronic instabilities of the extended Hubbard model on the honeycomb lattice from functional renormalization," *Phys. Rev. B*, vol. 94, p. 165107, Oct 2016.

[150] F. Wang, H. Zhai, and D.-H. Lee, "Nodes in the gap function of LaFePO, the gap function of the Fe(Se,Te) systems, and the STM signature of the $s_{\pm}$ pairing," *Phys. Rev. B*, vol. 81, p. 184512, May 2010.

[151] W.-S. Wang, Y.-Y. Xiang, Q.-H. Wang, F. Wang, F. Yang, and D.-H. Lee, "Functional renormalization group and variational Monte Carlo studies of the electronic instabilities in graphene near $\frac{1}{4}$ doping," *Phys. Rev. B*, vol. 85, p. 035414, Jan 2012.

[152] W.-S. Wang, Z.-Z. Li, Y.-Y. Xiang, and Q.-H. Wang, "Competing electronic orders on kagome lattices at van Hove filling," *Phys. Rev. B*, vol. 87, p. 115135, Mar. 2013.

[153] Q. H. Wang, C. Platt, Y. Yang, C. Honerkamp, F. C. Zhang, W. Hanke, T. M. Rice, and R. Thomale, "Theory of superconductivity in a three-orbital model of Sr 2 RuO 4," *EPL (Europhysics Letters)*, vol. 104, no. 1, p. 17013, 2013.

[154] C. Weeks and M. Franz, "Interaction-driven instabilities of a dirac semimetal," *Phys. Rev. B*, vol. 81, p. 085105, Feb 2010.

[155] F. J. Wegner and A. Houghton, "Renormalization Group Equation for Critical Phenomena," *Phys. Rev. A*, vol. 8, pp. 401–412, Jul 1973.

[156] T. O. Wehling, E. Şaşıoğlu, C. Friedrich, A. I. Lichtenstein, M. I. Katsnelson, and S. Blügel, "Strength of Effective Coulomb Interactions in Graphene and Graphite," *Phys. Rev. Lett.*, vol. 106, p. 236805, Jun 2011.

[157] T. Wehling, A. Black-Schaffer, and A. Balatsky, "Dirac materials," *Advances in Physics*, vol. 63, no. 1, pp. 1–76, 2014.

[158] C. Wetterich, "Exact evolution equation for the effective potential," *Phys. Lett.*, vol. B301, pp. 90–94, 1993.

[159] K. G. Wilson, "Renormalization Group and Critical Phenomena. I. Renormalization Group and the Kadanoff Scaling Picture," *Phys. Rev. B*, vol. 4, pp. 3174–3183, Nov 1971.

[160] K. G. Wilson, "Renormalization Group and Critical Phenomena. II. Phase-Space Cell Analysis of Critical Behavior," *Phys. Rev. B*, vol. 4, pp. 3184–3205, Nov 1971.

[161] Y.-Y. Xiang, Y. Yang, W.-S. Wang, Z.-Z. Li, and Q.-H. Wang, "Functional renormalization group study of pairing symmetry and pairing mechanism in iron-selenide superconductors," *Phys. Rev. B*, vol. 88, p. 104516, Sep 2013.

[162] D. Zanchi and H. J. Schulz, "Weakly correlated electrons on a square lattice: A renormalization group theory," *EPL (Europhysics Letters)*, vol. 44, no. 2, p. 235, 1998.

[163] Y. Zhang, Y.-W. Tan, H. L. Stormer, and P. Kim, "Experimental observation of the quantum Hall effect and Berry's phase in graphene," *Nature*, vol. 438, pp. 201–204, Nov. 2005.